DEVELOPING A VISCOELASTIC MODEL AND CONTROLLER FOR THE MRE ISOLATOR OVER A WIDE FREQUENCY RANGE

Thesis

Submitted in partial fulfilment of the requirements for the degree of

DOCTOR OF PHILOSOPHY
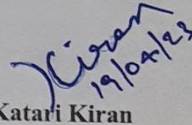
by

KATARI KIRAN

Reg.No. 165077 ME16F07

DEPARTMENT OF MECHANICAL ENGINEERING
NATIONAL INSTITUTE OF TECHNOLOGY KARNATAKA (NITK)
SURATHKAL, MANGALORE - 575 025
April 20, 2023

DECLARATION

By the Ph.D. Research Scholar

I hereby *declare* that the Research Thesis entitled **"Developing a viscoelastic model and controller for the MRE isolator over a wide frequency range"**, which is being submitted to the ***National Institute of Technology Karnataka, Surathkal*** in partial fulfilment of the requirements for the award of the Degree of ***Doctor of Philosophy*** in ***Mechanical Engineering*** is a *bonafide report of the research work carried out by me.* The material contained in this thesis has not been submitted to any University or Institution for the award of any degree.

Katari Kiran
Register No.: 165077 ME16F07
Mechanical Engineering
National Institute of Technology Karnataka,
Surathkal

Place: NITK, Surathkal

Date: April 20, 2023

DECLARATION

By the Ph.D. Research Scholar

I hereby *declare* that the Research Thesis entitled **"Developing a viscoelastic model and controller for the MRE isolator over a wide frequency range"**, which is being submitted to the ***National Institute of Technology Karnataka, Surathkal*** in partial fulfilment of the requirements for the award of the Degree of ***Doctor of Philosophy*** in ***Mechanical Engineering*** is a *bonafide report of the research work carried out by me*. The material contained in this thesis has not been submitted to any University or Institution for the award of any degree.

Katari Kiran
Register No.: 165077 ME16F07
Mechanical Engineering
National Institute of Technology Karnataka,
Surathkal

Place: NITK, Surathkal

Date: April 20, 2023

CERTIFICATE

This is to *certify* that the Research Thesis entitled **"Developing a viscoelastic model and controller for the MRE isolator over a wide frequency range"**, submitted by **Katari Kiran** (Register Number: 165077 ME16F07) as the record of the research work carried out by him, is *accepted* as the *Research Thesis submission* in partial fulfillment of the requirements for the award of degree of ***Doctor of Philosophy***.

Dr K V Gangadharan
Research Guide
Professor
Department of Mechanical Engineering
NITK Surathkal - 575025

Chairperson - DRPC
(Signature with Date and Seal)

CERTIFICATE

This is to *certify* that the Research Thesis entitled **"Developing a viscoelastic model and controller for the MRE isolator over a wide frequency range"**, submitted by **Katari Kiran** (Register Number: 165077 ME16F07) as the record of the research work carried out by him, is *accepted* as the *Research Thesis submission* in partial fulfillment of the requirements for the award of degree of ***Doctor of Philosophy***.

Dr K V Gangadharan
Research Guide
Professor
Department of Mechanical Engineering
NITK Surathkal - 575025

Chairperson - DRPC
(Signature with Date and Seal)

Statements of Contribution

This thesis is based on the following published articles.

- Kiran, K., Poojary, U. R., and Gangadharan, K. V. (2022). "Developing the viscoelastic model and model-based fuzzy controller for the MRE isolator for the wide frequency range vibration isolation." *J. Brazilian Soc. Mech. Sci. Eng* ., 44(7).

- Kiran, K., Poojary, U. R., and Gangadharan, K. V. (2022). "Fractional-order viscoelastic modeling of the magnetic field dependent transmissibility response of MRE isolator." *J. Intell. Mater. Syst. Struct.*

  https://doi.org/10.1177/1045389X221087172, 1045389X2210871.

ABSTRACT

Passive rubber isolators are designed to isolate vibrations for a fixed set of operating frequencies. To design an isolator over broadband frequency, it must change its property to adapt depending upon the frequency of excitation. The semi-active isolator has the desired qualities to achieve the required vibration isolation over broadband frequency. Among the available semi-active isolators, MRE (Magnetorheological Elastomer) isolator is one such isolator where the dynamic properties of the active element are varied by applying magnetic field. The active element MRE consists of ferromagnetic filler particles dispersed in an elastomer matrix. Other than magnetic influence, the MRE dynamic properties are influenced by amplitude of excitation and frequency under passive and magnetized conditions, due to its physical structure being particulate composite. This complex behaviour of MRE makes it challenging to develop a mathematical model for an MRE isolator considering all the operating parameters. Furthermore, because the mathematical model for the isolator is unknown, developing control for such conditions becomes more difficult.

Present work focused on the design of MRE isolator to regulate micron-level vibrations in electronic circuit boards application. The initial methodology involved designing the MRE isolator to operate in shear mode. The performance of the isolator was then evaluated through a displacement transmissibility test over a frequency range of 15 Hz to 80 Hz. The test involved varying the input current to the isolator from 0 A to 3 A, as well as the excitation amplitudes from 1.25 mm to 2.25 mm. Performance results show that MRE isolator changes its stiffness under magnetic field, and increases the overall natural frequency of the system. On the other hand, under passive and active conditions, the change in stiffness decreases with the amplitude of excitation. This is due to Payne effect which exists in the particle filled elastomer. Overall, the shift in the natural frequency and relative increase in stiffness decreased from 21.07 Hz to 16.09 Hz and 190.09% to 154.78%, with increasing the amplitude of excitation from 1.25 mm to 2.25 mm. The damping ratio of the MRE isolator increases with increasing current input but decreases with increasing excitation amplitude. This behaviour was observed in the passive and active states of the MRE isolator. The decrease or increase in damping is primarily caused by the decrease or increase in friction between the particle and the matrix. According to the results of the performance tests, the designed isolator provides

maximum vibration isolation of approximately 74.12% at 2.25 mm excitation amplitude and minimum vibration isolation of approximately 39.04% at 1.25 mm excitation amplitude under 3 A current input.

The conventional methods of developing the viscoelastic model involves the estimation of the parameters for the steady-state response of the isolator for a single frequency of excitation. To develop a complete mathematical model using this method involves a larger number of experiments as well as time. To overcome this problem, a state-space approach was introduced, which involves the estimation of model parameters for steady-state response of MRE isolator under multiple sweep frequency of excitation. In this approach, initially, a viscoelastic model consisting of Zener and Bouc-Wen elements arranged parallelly was considered. Here, the Zener element in the model was used to predict the viscoelastic properties of the MRE isolator, and the Bouc-Wen element, on the other hand, was used to predict the hysteresis behaviour of the MRE isolator. Once the mathematical model was defined, in the second stage, a linear second-order state-space equation was extracted from experimental data using the MATLAB system identification toolkit. Once the linear state space was determined, the unknown parameter values of the viscoelastic model were estimated by minimising the mean square error between the linear state space and the model response using MATLAB optimization toolkit. Using the known model parameters with respect to current input, a polynomial equation was used to establish a relationship between the viscoelastic model parameter and the current input to the isolator. This state-space approach modelling reduces the number of experiments required to develop the mathematical model for the MRE isolator over a wide frequency range. The model parameters for the different excitation amplitudes were estimated based on the Controller Stopping frequency (CS frequency). This reduces the further amount of experimentation, and the polynomial equation was used to establish the relationship between the current input to the isolator and the amplitude of excitation. This relationship equation was used to calculate the viscoelastic model parameter values with respect to excitation amplitude. Hence, the complete mathematical model which consists of all the influencing operating parameter is ready for use in the control development.

For effective use of the MRE isolator, a superior control strategy was implemented, and the superior controller chosen based on the following characteristics:

- The designed controller should be robust and adaptive to ensure the stability of the system.

- Should consider uncertainty in the model parameters.

- Should consider the uncertainty in the external environment changes.

The previously developed fuzzy controller has the problem of producing control output even when it is isolated. To overcome this problem, a control condition was developed based on the model to control the output of the Fuzzy controller. Another controller, a model-based sliding mode controller (MBSM controller), was also developed in addition to the fuzzy controller to produce the desired response at the receiver end. In the simulation, the performance of both model-based controllers was tested using random excitation signals. The test results confirm that the MBSM controller works more efficiently than the fuzzy controller to control the amplitudes of the vibrations.

Another model-free controller, the radial basis function neural network sliding mode controller (RBSM controller), was also developed. The unknown model was estimated by a radial basis neural network in this controller, and the sliding mode controller was the primary controller that produced the control input to the isolator. Ten neurons were considered for ten conditions, and the desired output was generated using the radial basis function neural network sliding mode controller (RBSM controller). The simulation results show that the RBSM controller works properly in all ten conditions. An additional set of conditions were also considered when testing the effectiveness of the controller; the results confirm that the RBSM delivers the desired output as expected.

Acknowledgements

their ongoing support and love. In addition, I'd like to express my heartfelt gratitude to everyone who helped or motivated me to reach this milestone, whether directly or indirectly.

Dedicated

to

my inspiring professor

and

My dear friend

Contents

List of Figures

List of Tables

Nomenclature

List of Symbols

m	Mass
k	Stiffness
c	Damping Coefficient
ζ	Damping ratio
ω	Angular frequency
f	Frequency of excitation
η	Loss factor
I	Current input to Isolator
A	Amplitude of excitation
$x(t)$, $\dot{x}$, and $\ddot{x}$	Displacement, velocity and acceleration of the receiver
$w(t)$	Excitation amplitude
Z	Bouc-Wen Force
C_1 and η_1	Sliding mode controller gains
W	Weights of the neural network
b	Bias of the neural network
$h(x)$	Gaussian function
$s(x)$	Sliding surface

$e(x)$ and $\dot{e}(x)$ Error and Error rate

$F(t)$ Control Force

$f(t)$ Property Function

List of Abbreviation

MRE   Magneto-rheological Elastomer

MBF Controller   Model Based Fuzzy controller

MBSM Controller   Model Based sliding-mode controller

RBSM Controller   Radial Basis function Neural Network Sliding mode controller

SDOF   Single Degree of Freedom

NPSS   Non-parametric State Space

ZPSS   Zener parametric State Space

LSS   Linear State Space

CIP   Carbon iron Powder

NR   Natural Rubber

RTV   Room Temperature Vulcanised

HTV   Higher Temperature Vulcanised

CS frequency   Controller stopping frequency

Chapter 1

INTRODUCTION

Summary

In this chapter, the importance of vibration isolation and the effect of the system parameters on the isolation of vibration are discussed. With the understanding of previous sections, practical methods to the common passive techniques used for vibration isolation are discussed. After that, the active and semi-active isolator technology is introduced to address the issues of a passive isolator. The following section includes details on a brief overview of semi-active MRE isolators, the working of MRE isolators, and the importance of implementation of isolator in electronic circuit boards are discussed. At the end of the chapter, the outline of the thesis is discussed.

A typical industrial or commercial workplace contains a plethora of devices and machinery that could result in unwanted vibrations. Fans, motors, and other machinery that produce abnormally high levels of vibrations during normal operation are common examples. Uncontrolled vibration levels can be dangerous and inconvenient. If an abnormal vibrations of a machine or piece of equipment occurs during normal operation, it can cause bolts and screws to loosen over time, disruption of smaller and more sensitive mechanical components, and eventually damage the machine or piece of equipment (Collacott 1977). The cumulative effect causes the machine or equipment to operate inefficiently, causing output delays.
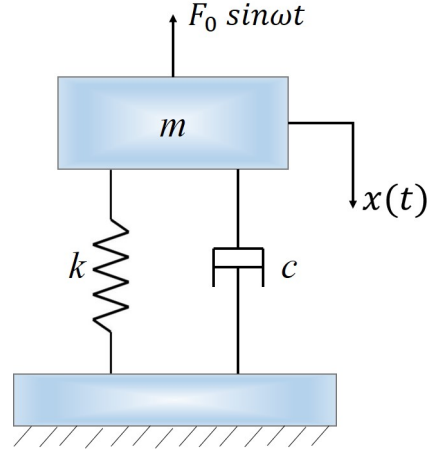
Figure 1.1: SDOF model of vibrating system

1.1 Effect of system parameter on the vibration response

Vibrations management is critical for structural and machine components that are continuously subjected to dynamic loading. In general, there are various methods to control vibrations (Costain and Robichaud 2004). Consider the lumped mass model of an SDOF (Figure 1.1) system consisting of mass m stiffness k and damping coefficient c.

The equation of motion for the SDOF system is

$$m\ddot{x} + kx + c\dot{x} = F_0 \, sin\omega \, t \qquad (1.1)$$

where, F_0 is input force. ω frequency of excitation and x is the displacement

The response $x(t)$ will be composed of a homogeneous solution (the transient response) and a particular solution (the steady state response) as

$$x(t) = e^{-\zeta\omega t}[A\sin(\sqrt{1-\zeta^2}\omega t) + B\cos(\sqrt{1-\zeta^2}\omega t)] \qquad (1.2)$$

where, A and B are arbitrary constants. To find the particular solution to equation, assume that the solution will be in the following form

$$x(t) = X\sin(\omega t - \varphi) \qquad (1.3)$$

where, X is the response amplitude and φ phase between input of excitation and response Substituting equation 1.3 in equation 1.1 and finding the components of forces

2

acting on a SDOF system, are the stiffness force, damping force and inertial force. The mathematical expression representing those forces are

$$kx = kX\sin(\omega t - \varphi) \tag{1.4}$$

$$c\dot{x} = c\,X\omega\cos\left(\omega t - \varphi\right) = c\,X\omega\sin\left(\omega t - \varphi + \frac{\pi}{2}\right) \tag{1.5}$$

$$m\ddot{x} = -mX\omega^2\sin(\omega t - \varphi) = -mX\omega^2\sin(\omega t - \varphi + \pi) \tag{1.6}$$
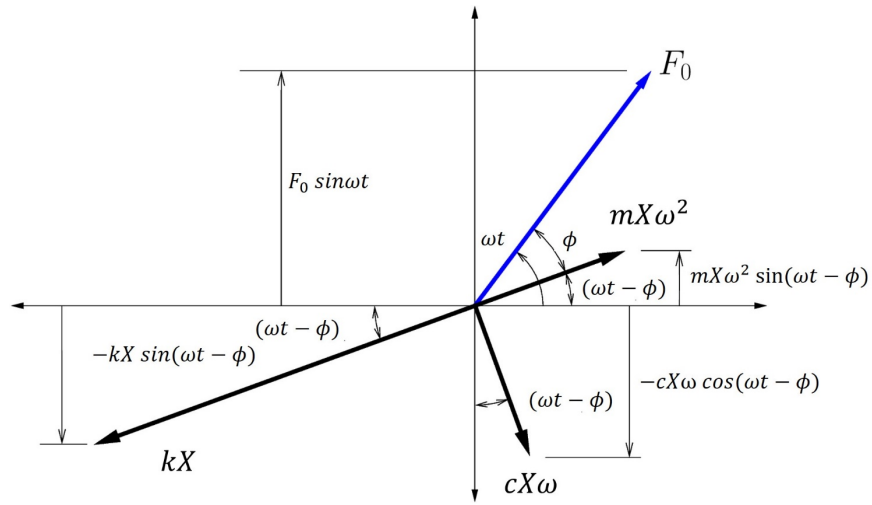
Figure 1.2: The phasor representation of forces

The phasor representation of the above forces is shown in Figure 1.2. The excitation force leads the response of the system by an angle φ and the damping force acts at an angle $90°$ to the stiffness force, and the inertial force acts is out of the phase with stiffness force. Substituting the equation 1.4,1.5 and 1.6 in equation 1.1, then

$$k\,X\sin\left(\omega t - \varphi\right) + c\,X\omega\cos\left(\omega t - \varphi\right) - mX\omega^2\sin\left(\omega t - \varphi\right) = F_0\,\sin\omega t \tag{1.7}$$

The goal of any design engineer is to minimize the transmitted force F_T. The ratio of the transmitted force and the input force represents the amount of vibrations transmitted, which is expressed as the transmissibility ratio. The transmissibility is estimated using with following equation

$$Tr = \frac{F_T}{F_0} = \sqrt{\frac{k^2 + (c\omega)^2}{(k - m\omega^2)^2 + (c\omega)^2}} = \sqrt{\frac{1 + \left(2\frac{\omega}{\omega_n}\xi\right)^2}{\left(1 - \frac{\omega}{\omega_n}\right)^2 + \left(2\frac{\omega}{\omega_n}\xi\right)^2}} \tag{1.8}$$

3
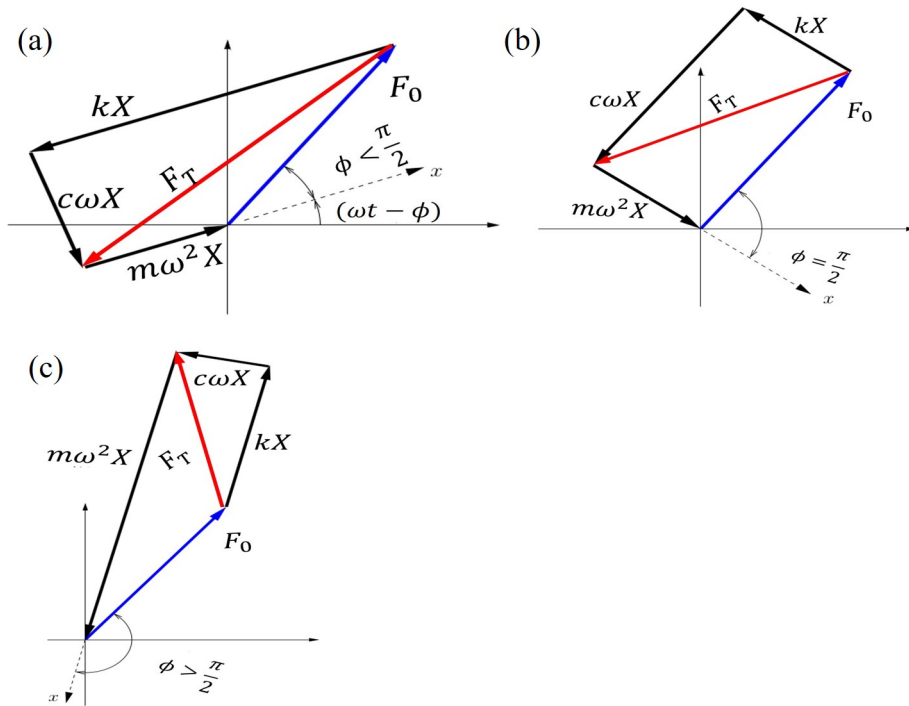
Figure 1.3: Graphical representation of force vectors as a function of operating frequency (a) $\omega < \omega_n$, (b) $\omega = \omega_n$ and (c) $\omega > \omega_n$,

There are various approaches developed to mitigate vibrations. These methods vary with region of interest corresponding to the force transmissibility response. For a system operating below the natural frequency of the system, the input force leads the response by an angle of less than $\frac{\pi}{2}$. The graphical representation of the forces corresponding to this state is presented Figure 1.3(a). The spring force dominates the over the inertial force. Consequently, to reduce the vibration in the system, either the stiffness of the system must be increased, or the mass of the system must me decreased. At resonance, the input force leads the response by $90°$. The vector representation corresponding to this state is shown Figure 1.3(b). The effect of stiffness force and inertial force are null because their magnitudes are the same and but with a phase difference of $180°$ phase. At this state, the vibration of the system can be controlled by increasing the damping force. The vector representation of the forces when the system is operating above the natural frequency is shown in Figure 1.3(c). In this case, the response is $180°$ out of phase with the input force and the inertial force dominates over the spring force. At this condition the vibration of the system can be controlled either by increasing mass or decreasing stiffness of the system.

4

1.2 Vibration control techniques

Protection from damaging vibrations is critical for the integrity of a structure subjected to dynamic loading. Often the stiffness or the mass is varied to maintain the vibration levels within the safe limit. Based on the energy requirement and the medium that decouples the structure from the source of disturbance, vibration control techniques are classified as passive, active and semi-active.

1.2.1 Passive vibration control techniques

The Passive vibration control technique is often used when the operating frequency of the system is constant. This approach is realized either by modifying the mass, stiffness or the damping to control vibration. The following section discusses the different practical scenarios where this method is employed.

i. Vibration control using mass

Mass addition is the simple approach often considered to reduce the vibration whenever the stiffness of the system is high. According to this approach, an additional mass is attached to mitigate the vibrations in a system undergoing translation or rotation. The mass unbalance and the foundation isolation using inertial mass are the commonly used mass addition techniques.
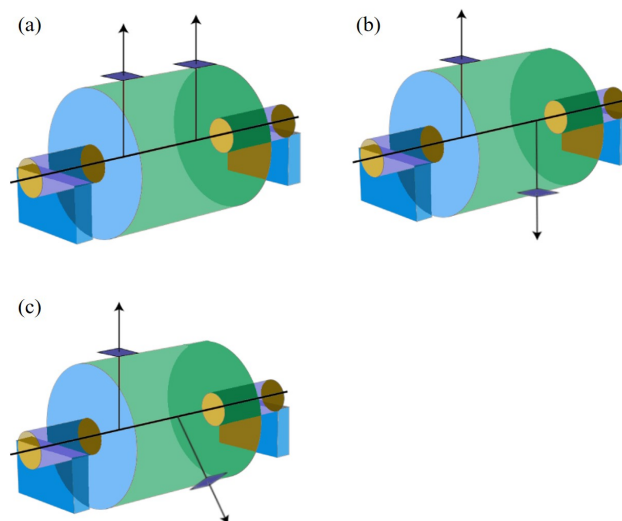
Figure 1.4: (a) static (b) and (c) dynamic unbalance of rotating bodies

5

a. Unbalanced Mass

Mass unbalance is the major reason for the vibrations in rotating machinery. The rotating unbalance is categorized as static, and dynamic (Figure 1.4). In static case, the mass axis is displaced parallel to the axis of rotation and the centrifugal force (F) responsible for the torsional vibration is given by,

$$F = mr\omega^2 \tag{1.9}$$

where, m static mass, r is the distance between the center of gravity (COG) and the center of rotation and ω is the angular velocity of the rotor. The static unbalance is achieved by adding an equivalent mass m opposite to location of the unbalanced mass at a distance r. The dynamic unbalance is also referred to as the couple unbalance. In this case the unbalance results from the couple developed due to the unbalance mass present at different planes of rotation. To dynamically balance the system, weights are added at two planes, which develops a reactive couple to compensate the effect of unbalance.
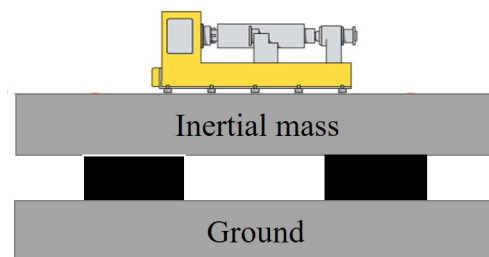
Figure 1.5: Foundation isolation through the addition of inertial mass

b. Foundation isolation through mass addition

This method is particularly useful for the equipment that experiences high levels of vibration or transient (impacting) forces, such as hammer mills, diesel engines, positive displacement pumps, etc. This method works on the principle that, under constant input force, if the mass of a system is increased, the acceleration (vibration response) of the system will decrease. As discussed in Section 1.1, for a system operating at a frequency greater than its natural frequency, the mass of the system must be increased to a certain level to control vibrations. This method works efficiently when the stiffness supported by mass is exceptionally high to support mass. This scheme is realized by mounting

the vibrating machine on a massive concrete block and isolating the block from the foundation with rubber isolators (Figure 1.5). For the success of vibration isolation in case of mass addition, the frequency ratio of the isolator f/f_n must be greater than, $\sqrt{2}$. Accordingly, for a known machinery mass, stiffness and damping coefficient, the desired inertial mass (for undamped case) for achieving required isolation is given by following equation

$$m = \frac{k(T-1)}{T\omega^2} \qquad (1.10)$$

where, T is desired transmissibility

ii. Vibration control using stiffness

The natural frequency of a dynamic system depends on the inertial mass and the stiffness. The stiffness of the system is modified in order to avoid the resonance during normal operating conditions. The amount of modification depends on the inertial mass of the system. If decreasing stiffness does not influence structural failure, then isolators are chosen for vibration control. On the contrary, system stiffness is increased to a certain level to change the natural frequency of the system where the mass of the system is very high. System detuning, vibration isolation and vibration absorption are the common approaches used to modify the vibration response of the system by the stiffness addition.

Tuning is a technique for reducing amplification due to resonance by adjusting the natural frequency of a system or component so that it no longer coincides with the frequency of a specific force input. For an undamped or lightly damped system, the vibration response of industrial equipment will be amplified at the resonance frequency. However, for a damped system, the peak amplitude of response at the resonance is significantly reduced. On the contrary, the half power points are wider for a damped system when compared to the low damped system. Under this state, natural frequency tuning is the viable option.

Generally, it is the range of resonance that governs how much tuning (change in the natural frequency of the system) will be required to completely eliminate resonance. For a given system, to estimate the resonant frequency, forced response (bump) test should be used to determine the natural frequency (and damping characteristics) before attempting to detune it. After evaluating the resonant frequency, a decision on whether to raise or lower the natural frequency must be made. The natural frequency is propor-

tional to the square root of stiffness to mass ratio in a simple (SDOF) vibrating system. Increasing stiffness raises the natural frequency and it is most commonly used because increasing mass and/or decreasing stiffness (in order to lower the natural frequency) may compromise the strength of a machine or the structure that supports the machine.
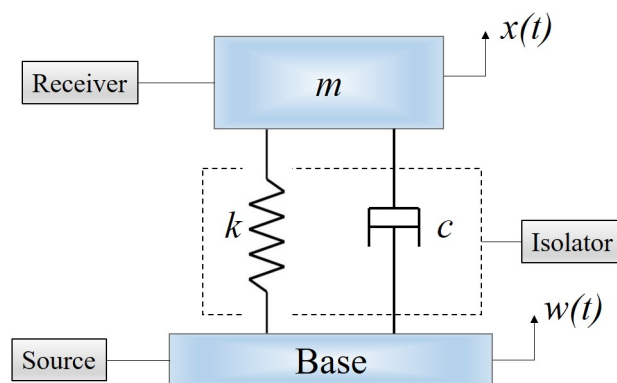
Figure 1.6: Vibration isolator

The vibration isolation using the isolator is an alternative approach to mitigate the transmitted vibration or noise due to the machinery mounted on floors or walls. Ideally, the optimal location for a vibrating machine is on the ground floor. Unfortunately, this condition cannot always be achieved. A common occurrence is a rotating machine (such as a pump, air conditioner compressor, blower, or engine) positioned on a roof or above the ground floor. Typically, the condition is most noticeable in the immediate proximity of the vibration source. Mechanical vibrations, on the other hand, can travel great distances and take extremely tortuous pathways through the structure of a building, occasionally resurfacing hundreds of feet from the source. It is important that vibration from the source must be isolated to the receiver end of the equipment or machine. This is usually done using isolators that are installed between the source to receiver end, which is shown in Figure 1.6.

The stiffness of the isolator is selected based on the amount of isolation required at the receiver end. The required stiffness (consider the damping is zero) of the isolator to reduce the vibration in the receiver end is given by the following equation

$$k = \frac{T\omega^2}{m(T-1)} \tag{1.11}$$

8

It is very important that the support structure and equipment must be properly secured to the isolator because any deflection of the support structure could diminish the performance of the isolator.
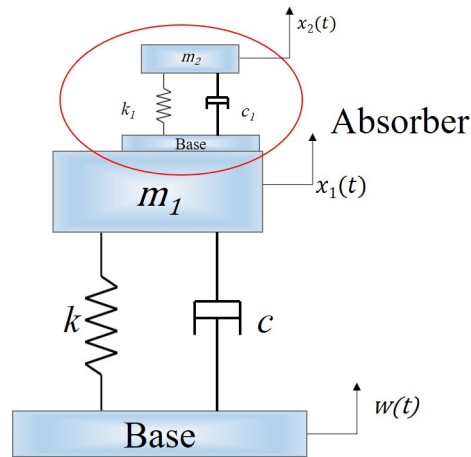
Figure 1.7: vibration absorber

The vibration absorption is a viable option when vibration is not supposed to reach to reach receiving member. The device is often termed a dynamic vibration absorber (Figure 1.7). It is as secondary system that has mass and stiffness attached to the primary system mass that has to be protected from unwanted vibration. Thus, the basic system mass and the associated absorber mass creates a two-degree-of-freedom system, hence the vibration absorber will have two natural frequencies. The vibration absorber is typically employed in machinery that operates at a constant speed because the vibration absorber is set to one particular frequency and is effective only within a restricted spectrum of frequencies. Common applications of the vibration absorber include reciprocating equipment, such as sanders, saws, and compactors, and big reciprocating internal combustion engines which run at constant speed (for minimum fuel usage).

iii. Vibration control using Damping

Despite the fact that the terms "vibration damping" and "vibration isolation" are frequently used interchangeably, they refer to two distinct types of vibration mitigation methods. Vibration damping is the process of absorbing or changing vibration energy in order to reduce the amount of energy transmitted from equipment or machinery to the structure, whereas vibration isolation is the process of preventing energy from entering equipment or machinery. In the context of damping, energy is dissipated by the release of low-grade heat, which is typical of this process. Section 1.1 discussed how increasing

the damping can help to reduce the transmissibility amplitude at natural frequency and conditions where the ratio of the excitation frequency to the natural frequency is less than a factor of two. But increasing damping in the isolation region (where $\frac{\omega}{\omega_n} > \sqrt{2}$) increases the response amplitude.

One of the most common damping mechanisms is dry friction, which causes an object sliding on a surface to slow down and eventually come to a stop. Some mechanical devices dissipate energy through the use of viscous damping. The energy loss in these systems is provided by a liquid being forced through a small opening. Viscous dampers are commonly found in the shock absorbers of automobiles. There is a long history of mathematical models for viscous damping that can be used for analysis. The damping ratio, $\frac{c}{c_c}$ or ζ, characterises viscous damping capability.

The majority of elastomeric engineering materials used for vibration isolation employ a mechanism known as hysteretic damping to dissipate the energy generated by the vibration. As a result of the deformation of these materials, internal friction causes significant energy losses to occur. The loss factor used for determining the amount of energy dissipation through hysteretic damping in a material. The ratio of the energy dissipated from the system to the energy stored in the system for each oscillation of the system gives the loss factor (η). It is frequently necessary to relate the loss factor to the damping ratio in order to be able to use viscous damping models for analysis. It is possible to approximate the damping ratio from the loss factor using the following formula.

$$\eta = 2\frac{c}{c_c} = 2\zeta \tag{1.12}$$
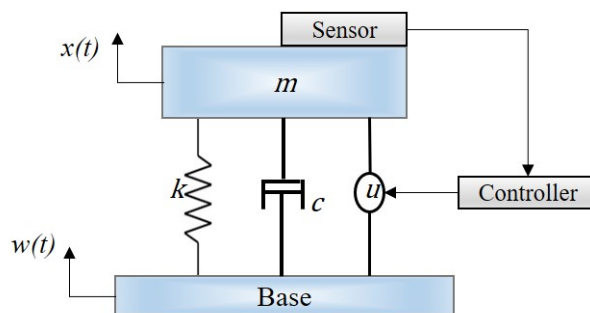
Figure 1.8: Active vibration isolator

1.2.2 Active vibration control technique

Passive isolators described in previous sections are intended to isolate excitation frequencies with a narrow bandwidth. To attain the vibration mitigation over a wide range of excitation frequencies, the active and semi-active vibration control methods are more effective (Karnopp 1995). An active vibration control method requires an external power source known as an actuator (for example, a hydraulic piston, a piezoelectric device, or an electric motor). The actuator will provide a force or displacement to the system based on response of the system as measured by the feedback control system. As depicted in Figure 1.8, the working principle of an active vibration control system begins with measuring response of the system using appropriate sensors. The electronic circuit then reads the sensor output, converts it appropriately, and sends it to the control unit. The calculated force signal is sent to the actuator and the controlled force is applied to the system based on the control law used. The actuator force will actually compensate for vibration force of the system. Active vibration control is entirely reliant on external source to power the actuators and deliver the necessary control forces to the system. The main drawbacks of the active vibration isolator are the cost and energy consumption are significantly higher.
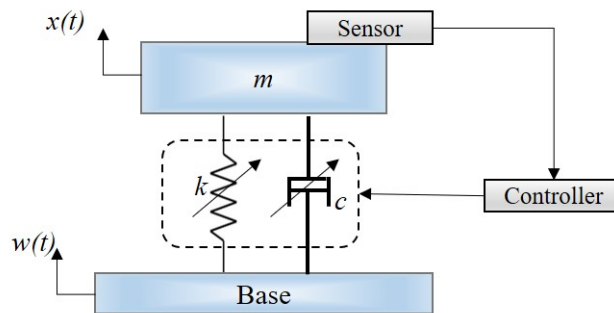
Figure 1.9: Semi-Active isolator

1.2.3 Semi-Active vibration control technique

A schematic representation of a semi-active vibration isolation system is shown in Figure 1.9. The semi active isolator possesses the attributes similar to passive isolator, but it differs with the ability of resilient element to modify the properties in response to the external stimuli. In a typical semi active vibration isolator, the vibration of the base and mass is monitored and transmitted into a controller, which adjusts the stiffness

and damping coefficient such that the stiffness and damping force increase or decrease based on the displacement and velocity of the relative position difference of mass and base. Semi-active isolators consume far less energy than active devices, and this energy is frequently stored locally, in the form of a battery, making the semi-active isolator independent of any external power supply.

Resilient elements in semi-active vibration-control unit are typically comprised of variable rate damper and stiffness. Significant efforts have been devoted to the development and implementation of such devices for a variety of applications. Examples include electro-rheological, magneto-rheological (MR) fluid dampers, variable orifice dampers, controllable friction braces, controllable friction isolators, and variable stiffness devices including pneumatic isolators. Winthrop et al. (Winthrop et al. 2005) listed numerous smart materials-based variable stiffness and damping-based devices and discovered that Magnetorheological elastomer (MRE) had the greatest stiffness variation when compared to other smart material-based devices. Compared to variable damping devices, variable stiffness-based devices perform better in low frequency than in high frequency. The reason for this is that the controlling force is the product of stiffness and displacement, and in the case of variable damping devices, it is the product of damping coefficient and velocity (Xu et al. 2016).
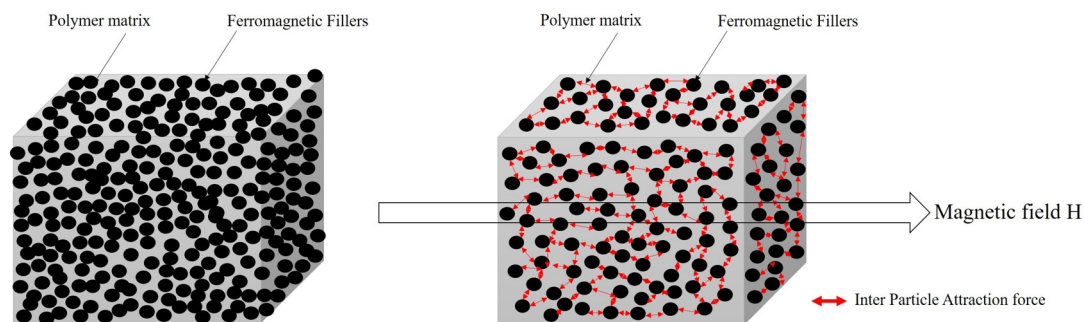
Figure 1.10: Structure of MRE (a) Before (b) After application of magnetic Field

1.3 MRE: An Overview

Magnetorheological elastomers (MREs) are smart materials comprised of Polymer matrix and micrometer-sized ferromagnetic filler particles (Figure 1.10). Under the influence of external magnetic field, the stiffness of the MRE increases due to interaction between the fillers (Jolly et al. 1996) (Figure 1.10). MRE can generally be distinguished

based on how the filler particles are distributed within the matrix. The isotropic structure of MRE in attained when the filler particles are randomly dispersed in a polymer, and anisotropic structure comprises of an orderly arrangement of the fillers. MRE has gained an increased interest due to fast response, reversibility, ease of storage and the no sedimentation related issues. These unique attributes have opened up an immense potential in the engineering fields of civil structures (Li and Li 2015), precision fabrication (Dai et al. 2018), and vehicle suspensions (Hoang et al. 2011). Furthermore, MREs have a stronger magnetorheological effect at small strain amplitudes, making them more suitable for micro vibration control applications.
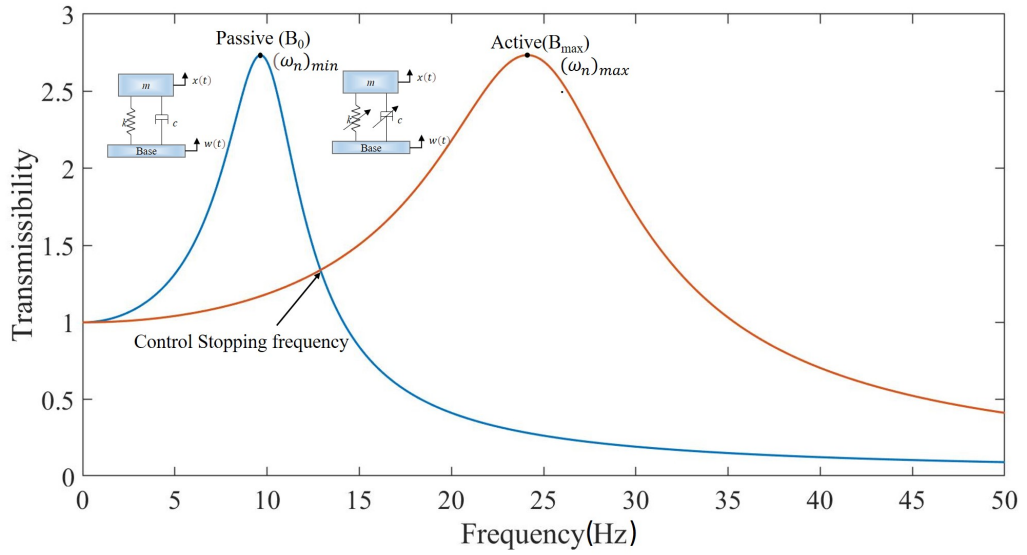
Figure 1.11: The change of natural frequency of the MRE

1.4 Concept of Semi active MRE isolator

Compared to the passive isolators, the MRE can mitigate vibrations over wider frequency range. Figure 1.11 depicts the typical performance of the MRE semi-active isolator. Under non magnetized state also referred as the passive state, the stiffness of the MRE is minimal and the natural frequency of the system is $\omega_{n_{min}}$. The stiffness of MRE in increased under the influence of magnetic field which in turn increases the natural frequency of the system to $\omega_{n_{max}}$. By employing an efficient control strategy, this unique attributes of MRE are used to attain the vibration isolation of a dynamic system over a broader frequency range. During operation, the controller should give an input

13

signal to MRE isolator so that the stiffness of the isolator is maximum whenever the excitation frequency is between 0 Hz and the CS frequency (Indicated in the Figure 1.11). For frequencies higher than the CS frequency, the controller should be turned off, and the stiffness of the MRE is kept to a minimum value.
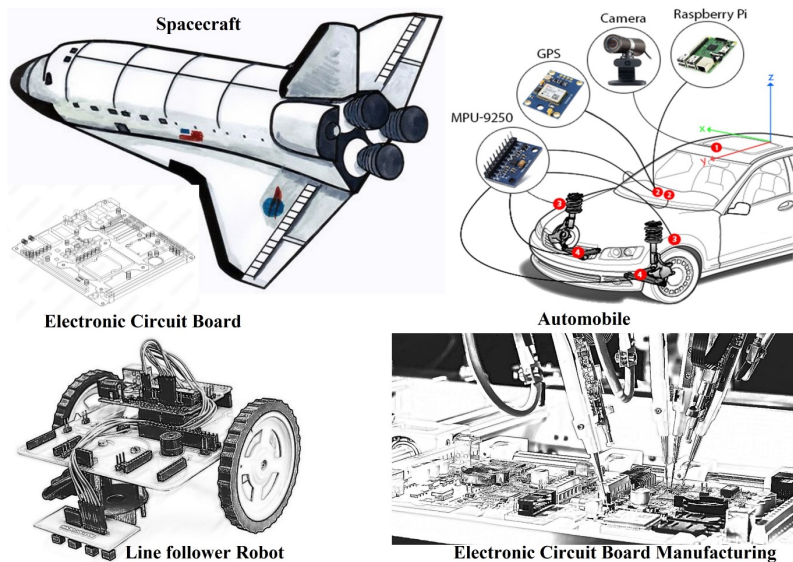
Figure 1.12: Vibration generation in electronic circuit board in various application (Menegazzo and Wangenheim (2021)

Semi active MRE isolators have a huge potential in controlling the vibrations in electronic circuit boards used in automobile, circuit board manufacturing, space crafts and robots. For example, during launch, a spacecraft is subjected to a various load, including vibration, acoustic, and shock loads (Figure 1.12). The electronic packages are built to endure the launch vibrations. To provide enough margins, electronic packages are subjected to vibration testing. Vibration loads have already caused package component breakdowns. The following conditions result in the four main failure scenarios of components installed on PCB due to random vibration environment: high acceleration levels, high stress levels, huge displacement amplitudes, and electrical signals out of tolerance.

Keeping in mind the need to regulate vibration in electronic circuit boards for application, The current effort aims to design an MRE isolator for micron-level vibration control. The present study addresses the significant hurdle faced in developing the mathematical model for MRE isolator and control development in order to deploy an MRE isolator in a real-world context. The methodology for developing an MRE isolator: first, design an MRE isolator and investigate its performance in a series of dis-

placement transmissibility tests with varying excitation and magnetic field amplitudes. The behaviour of the MRE isolator was mathematically modelled with a viscoelastic model. The model parameters values under the magnetic field and excitation amplitude were identified based state space approach and control stopping criteria. A model-based controller, such as a fuzzy controller or a sliding mode controller, was developed and used to provide control input to the isolator in order to isolate vibration in the receiver. The performance of the controller was evaluated in simulation under random excitation conditions. Following the development of the model-based controller, another type of controller, a model-free radial basis neural network sliding mode controller, was developed for the MRE isolator, and its performance was simulated using different excitation frequency and amplitude.

1.5   Outline of the thesis

There are seven chapters in this thesis.

- In Chapter 1, the importance of vibration isolation and the effect of the system parameters on the isolation of vibration are discussed. With the understanding of previous sections, practical methods to the common passive techniques used for vibration isolation are discussed. After that, the active and semi-active isolator technology is introduced to address the issue that are present in the passive isolator. The following section includes details on a brief overview of semi-active MRE isolators, the working of MRE isolators, and the importance of MRE isolator implementation in electronic circuit boards are discussed. At the end of the chapter, the outline of the thesis is discussed.

- In chapter 2, a comprehensive literature review is carried out, the primary focus of which is placed on the many different MRE isolator designs found in the previous research. In addition, the active element of the MRE isolator constitutes details, the available methodologies in testing the MRE isolators, the development of a mathematical model, and the existing control techniques implemented in the MRE isolator are detailly explained in this chapter. The literature review identifies the research gap and outlines a path forward for additional investigation. The questions that are left unanswered after the literature review are used to

for the formulation of the scope of the work, which is then presented at the end of the chapter.

- In chapter 3, the design methodology of the MRE isolator, as well as the construction details of the MRE isolator and the manufacturing of MRE, are discussed in detail.

- In chapter 4, the performance of the designed MRE isolator is evaluated using a series of displacement transmissibility tests with varying current input and excitation amplitude. These tests are performed in order to determine how well the isolator worked. The MRE isolator unique performance measuring parameters, such as stiffness, damping, the MR effect, and frequency shift parameters, are calculated with regard to the amount of current input and the amplitude of the excitation, and the results are presented in the form of a table.

- In chapter 5, the development of a viscoelastic model for MRE is discussed, and a mathematical relationship between the viscoelastic constituents and the current input was formulated. Based on the CS frequency, the amplitude-dependent viscoelastic modelling parameters of the MRE isolator was formulated in relationship with the current input to the isolator.

- In chapter 6, Model based controller and the model free controller development for MRE isolator is discussed in detail. In simulation, the model-based controller such as the model-based fuzzy controller, and the model-based sliding model mode controller are implemented on the MRE isolator and compared their performance under random excitation. Similarly, a model-free radial basis function neural network sliding mode controller for the MRE isolator is developed and tested in simulation for various excitation frequencies and amplitudes. Finally, the performance of the model-based fuzzy controller is estimated in real time on the MRE isolator.

- In chapter 7, a summary of the work done so far and the primary conclusions that can be drawn from it are presented. After that, major contribution from the current work and future work is discussed.

Chapter 2

LITERATURE SURVEY

2.1 Introduction

The necessity for low frequency range of vibration mitigation necessitates the development of a new class of semi-active isolator. MRE isolator is one such semi-active isolator having the ability to attain the ultimate goal. The design and development of an MRE-based isolator is a difficult task because its isolation capabilities are sensitive to changes in dynamic loading conditions. Consequently, the design of a MRE isolator necessitates a thorough understanding of isolation characteristics and its mathematical representation in order to execute the control mechanisms. In recent years, research on the development of MRE and its devices has continued to strive for improved qualities to enhance the operating range and effectiveness of a device.

As discussed in Chapter 1, design of an isolator necessitates a thorough understanding of existing research on various isolator designs, isolation capabilities of the developed isolator, and mathematical model development, and existing control strategies. This chapter contains a thorough and critical overview of the available literature on the MRE. The literature review improves understanding of the design, characterization, mathematical model, and control development of the MRE isolator. Furthermore, the literature review findings provide a proper guidance and a structured road map for the planned investigation. The literature review is organized into the following general sections.

1. Material overview of MRE

2. Synthesis of MRE Element

3. MRE isolator designs

4. Designing parameters of a MRE isolator

5. Performance assessment of the MRE isolator

6. Factors contributing to the performance of MRE isolator

7. Viscoelastic modelling of the MRE isolator

8. Semi active control strategies for MRE isolator

2.2   Material overview of the MRE

MRE consists of ferromagnetic fillers and nonmagnetic matrix. To improve the performance of the MRE additive are added. Additives are in powder form or liquid form, which either occupies in between the filler and matrix or improve the interface. The present section gives a brief inside into the MRE as a structural point of view.

2.2.1   Matrix materials

The matrix material is the medium that holds the particles in the absence of a magnetic field; however, under magnetic field, the particles try to align along the direction of magnetic field to form a chain like structure inside the matrix which modifies the properties of MRE. The mobility of a particle under the magnetic field depends on the properties of matrix. Matrix materials for MRE are chosen based on the various properties like hardness, porosity, initial modulus, magnetic field dependent modulus, and MR effect. List of matrix material are silicone rubber (Li et al. 2010), polyurethane (PU) (Chokkalingam et al. 2011), thermoset/thermoplastic elastomers (Lee et al. 2019c), an interpenetrating polymer network (IPN) (Yu et al. 2015a), and natural/synthetic rubber (Yunus et al. 2016).

Matrix materials used to make MRE fall into two categories: high temperature vulcanised (HTV) rubber and room temperature vulcanised (RTV) rubber. The temperature at which the crosslinking process is conducted distinguishes the HTV matrix of MRE (Chen et al., 2007b). The RTV elastomer matrix-based MRE is produced by combining polymer melt with ferromagnetic particles and curing at room temperature with a curing

agent (Perales-Martnez et al. 2017). The matrix and filler mixing process traps air bubbles in the mixture, which could result in a flawed MRE sample. Prior to initiating the curing process, air is extracted from the matrix by a vacuum degassing procedure (Li et al., 2010b). HTV MRE is synthesised by masticating matrix and fillers in a double-roll mill or using a conventional mixing process (Chen et al., 2007b; Zhang et al., 2010). The HTV MRE curing process is carried out at a higher temperature than the ambient temperature. The curing temperature varies depending on the matrix type, which in turn affects the viscoelastic properties of MRE (Chen et al., 2007b).

Silicone rubber is most offen used matrix material for synthesis of MRE. The primary reason is due to viscosity of uncured matrix and longer working. Additionally, these silicone-based matrices cure rapidly at elevated temperatures as well as at room temperature and are non-toxic and non-flammable. Silicone-based rubber have some drawbacks. One of the most significant disadvantages of silicone-based rubber is its poor mechanical performance, which manifests itself in low strength and short fatigue life (Abdul Aziz et al. 2017).

To improve the synthesis process additives like silicone oil are added to increase the fluidity and plasticity (Bica et al. 2012; Gong et al. 2005b; Khairi et al. 2019a). Additionally, other additives such as methyl tri-methoxysilane (Kashima et al. 2012), dimethyl silicone (Wu et al. 2020), silane clear (Ubaidillah et al. 2015), tert-buthyl perbenzoat (Ubaidillah et al. 2015), toluene-benzoil peroxide (Bastola et al. 2020), catalyst 60R/rhone-poulenc-stearic acid (Bunoiu and Bica 2016), and acetic initiator (Ubaidillah et al. 2015) have been considered to enhance the zero-field properties and MR effect of MREs.

Thermosets and thermoplastics have also attracted a great deal of interest for use as MRE matrix (Bica et al. 2019; Chen et al. 2020; Qi et al. 2015) due to the ease with which the types and concentrations of fundamental constituents can be changed. Use of thermoplastic elastomers over thermoset elastomers has several advantages, including the ease and speed with which they can be manufactured, their low energy consumption, and the possibility of reusing waste. The strength of thermoset elastomers is achieved through an irreversible crosslinking process that occurs when heat and pressure are applied, whereas thermoplastics can be melted by reheating. When compared to other types of elastomers, polyurethane (PU) is the most widely used thermoplastic-based

elastomer due to its excellent mechanical stability. The natural or synthetic rubbers (Alias et al. 2018a; Choi et al. 2007; Jung et al. 2016; Lee et al. 2012; Wahab et al. 2016) are another type of matrix material used in MREs.

Synthesis process of natural rubber and syntetic rubber are complex as compared to RTV rubber as it requires additional equipment and raw materials. Natural rubber (NR) and synthetic rubber (SR) are the least commonly used matrix materials for the fabrication of MREs due to their complexity in manufacturing (requiring more equipment), raw materials (solid phase), and resistance to thermal degradation. However, when compared to other matrices, the use of natural or synthetic rubbers has superior mechanical properties, such as higher tensile and rupture strength, as well as higher heat resistance (Hu et al. 2005), and as a result, the consideration of these matrices is continuously increasing. Other supplements/additives, such as plasticizers and crosslinking/vulcanizing agents (such as zinc oxide, stearic acid, sulfonamide, sulphur) (Cao et al. 2020; Ismail and Kamaruddin 2017; Raa Khimi and Lai 2018; Song et al. 2019), should be used to assist in the crosslinking of NR. Ethylene-propylene rubber (Qi et al. 2018), acrylonitrile rubber (Masłowski and Zaborski 2012), cis-polyisoprene/polyisoprene (Hafeez et al. 2020), styrene-butadiene rubber, and chloroprene rubber (Choi and Chung 2014) are examples of synthetic rubbers that have been used in the development of MREs. As part of the crosslinking process, these synthetic rubbers also require additives such as NRs.

2.2.2 Filler Particles

Magnetic particles are accountable for magnetic field-dependent MRE properties. Magnetic particles are the magneto-active component of MREs and are accountable for their magnetic field-dependent properties (i.e., MR effect). The most used magnetizable particles are carbonyl iron powders (CIPs). Due to their high magnetic saturation, low magnetic residual, softness, and high magnetic permeability, CIPs are regarded as the optimal material for manufacturing MREs (Khairi et al. 2018; Lokander 2002; Ubaidillah et al. 2015). Other magnetic particles used as filler include cobalt, nickel, and Nd–Fe–B. However, due to their lower magnetic residual value than CIP, these particles are less effective than CIP. Most often used CIP particles for the synthesis of MRE are spherical and have an average size of less than 10 μm. (Hafeez et al. 2020). The un-

derlying rationale for the use of smaller particles is that the smaller particle size provides a larger effective area for interfacial friction between magnetic particles and matrix materials, and may also produce an increase in the storage and loss moduli. Also reported are particles with a size range of 10–100 µm or even higher, up to 200 µm. This particle has an irregular form and has a substantial impact on the magnetic and nonmagnetic characteristics of MRE. The effect of magnetic particle size on MRE parameters such as modulus and loss factor is important. In the absence of a magnetic field, the MRE modulus decreases with increasing particle size. In the presence of a magnetic field, smaller particles exhibit a substantially greater rise in modulus (Ubaidillah et al. 2015).

In general, the MR effect is seen to increase as the magnetic particle concentration is higher. Increased particle concentration reduces the quantity of matrix material, hence decreasing the matrix rubber's tensile strength. The zero field modulus rises as the CIP concentration increases. According to L C Davis (Davis 1999b), the optimal volume fraction of Fe particles in the MRE should be 27 percent. Lokander invented the phrase "critical particle volume fraction (CPVC)" (Lokander 2002). This determines the maximum volume of filler particles that a matrix material may tolerate. This is often assessed by the material's apparent density. When the apparent density of ASC300 is 2.88 g/cm^2, MR rubber's CPVC content was 36.5%. Li and Zhang (Li and Zhang, 2010) employed two kinds of iron products with particle sizes of 50 and 5 µm to make a set of bimodal MRE samples. The MR elastomer with the ideal volume proportion of tiny particles in the bimodal particle combination (23.3 wt %) will have the greatest MR impact.

In addition to CIPs, other particles, such as hard NdFeB particles, have been utilised as magnetic fillers in MREs. NdFeB particles have an irregular form and vary in size from 1 to 100 µm. (Borin et al. 2019; Kramarenko et al. 2015; Stepanov et al. 2020; Xie et al. 2020; Yu and Ju 2011). According to Yu et al., the introduction of such a hard-magnetic filler led to substantial damping and bidirectional modulus changes in MREs. (Yu et al. 2015b). Several research have also suggested the usage of iron sand (Kurniawan et al. 2017; Raa Khimi and Pickering 2016). These iron sand particles vary in size between 45 and 56 µm. According to morphological studies, the use of iron sand did not impede the construction of the magnetic chain during the crosslinking process.

Modifications of CIPs have gained an increased interest for researchers in recent years. A surface coating, nano-flakes, and flower-like CIPs are among the modifica-

tions(Jolly et al. 1996a; Li et al. 2021a; Yu et al. 2015c). Such modifications are usually made to improve the interaction between the particles and the matrix material in order to achieve an effective damping property. Furthermore, such modifications improve particle dispersion and wettability between particles and matrix materials during processing. Coated magnetic particles include poly (tetrafluoropropyl methacrylate), (3-aminopropyl) triethoxy silane (APTES), silica-coated, polyaniline-modified, and siloxane-modified particles (An et al. 2017; Chen et al. 2016; Cvek et al. 2017; Kwon et al. 2019; Sedlacik et al. 2016; Yu et al. 2017).

2.2.3 Additives

The main role of additives in MREs is to enhance the field dependent properties, fundamentally known as MR effect as well as to provide sensing capabilities such as resistance and capacitance. Additives can be categorized as non-magnetic and magnetic additives: plasticizer and carbon-based materials are popular non-magnetic additives while chromium-based particles and other MNPs fall under the category of magnetic additives.

Plasticizers are the most typical additions for matrix materials. Silicone oil, mineral oil, phthalate easters, and silicone/natural-based esters are all common plasticizers found in MREs. Plasticizers are added to matrix materials to improve their flowability, flexibility, and workability, which helps the MRE process the materials. By mechanical mixing or vulcanization, a plasticizer can be dissolved in matrix material. Plasticizers and additives make it easier for rubber molecular chains to glide by serving as lubricants, lowering adhesiveness of the rubber matrix. As a result, when rubber is stretched and released, its molecular chains may readily slide back and forth. Similarly, plasticizers soften matrix materials, making it easier to align magnetic particles along the direction of a magnetic field for anisotropic MRE synthesis. Silicone oil is the most prevalent plasticizer in MREs. According to the findings of Khairi et al(Khairi et al. 2019b), adding roughly 15% wt silicon oil to silicone based MREs increases MR effects by 343 % (0.3 MPa) for isotropic MREs and 646% (0.8 MPa) for anisotropic MREs when compared to samples without silicone oil. Ahmad Khairi et al (Ahmad Khairi et al. 2017) Prepared a sample with composition of 60 wt% of CIPs, 32.5 wt% of ENR-50, and 7.5 wt% of SAIB ester. Results show that with addition of SAIB ester MR effect was

increased by 23% compared to the non- additive samples.

Other type of additive commonly found in MREs is carbon-based materials. Addition of these additives has the potential to improve the mechanical properties of matrix materials during processing, provide better mechanical properties after curing, improve the MR effect, and provide sensing capabilities. Nayak et al. (Nayak et al. 2015) produce an RTV silicone base MRE that contains 7% vol carbon blacks, 40% vol CI powders, and 53% vol RTV silicone. Mechanical parameters such as modulus have increased from 1.124 MPa to 1.763 MPa with the introduction of carbon black, and shear storage modulus has increased from 0.37 MPa to 0.45 MPa. Chen et al (Chen et al. 2008) developed a natural rubber-based MRE with varying amounts of carbon black (4 % Vol and 7 % Vol). The MR effect climbs to 104%, and the damping ratio approaches 0.25, according to the findings. The tensile strength of the sample rises from 2.37 MPa to 3.52 MPa, a 48.5% increase in relative strength. Carbon nanotubes (CNTs) are used as additive because of their advantages such as high aspect ratio, high surface to mass ratio, and lightweight. Li and Sun (Li and Sun 2011) investigated dynamic mechanical response of MR nanocomposites using 1 and 3.5 wt% of MWCNT in RTV silicone rubber in MRE. At all dynamic compression and shear tests, MR nanocomposite shows higher zero-field stiffness and damping along with greater magnetic field– induced increasing dynamic mechanical properties. Aziz et al. (Aziz et al. 2017) investigated the viscoelastic properties of several functionalized groups of MWCNTs reinforced with MREs. It was discovered that MREs with functionalized MWCNT have a better MR effect than MREs with pure MWCNT.

In addition, graphite microparticles and graphene nanoparticles have been explored for use in studying the sensing behaviour of MREs. The primary function of graphene particles in MREs is to give electroconductive properties. The electrical resistance of graphene-loaded MRE was observed to decrease as the magnetic field strength and compression force increased (Bica 2009). Although graphite can reduce the electric resistance of MREs, Tian et al. found that an excess of graphite powder reduces the MR effect (Tian et al. 2011).

Another type of additives known as magnetic or magneto-active additives include nano-sized iron oxides and nickel or cobalt-based nanowires. Song et al. (Song et al. 2009) created nanowire-based MRE composites with two different compositions, Fe and

Co, and three different particle weight fractions (i.e., 10, 30, and 50 wt%). According to the findings, nanowire based MREs have a greater specific modulus than MREs with spherical particles. CIP@FeNi particles are incorporated into MRE samples by Li et al (Li et al. 2021b) in order to improve transient magnetorheological response. The results show that adding 4% CIP@FeNi to MRE improves the magnetorheological property and the transient magnetorheological response property significantly. Yu et al. (Yu et al. 2015d) create Fe nano-flakes coated spherical carbonyl iron particles (CIP-Nano-Fe) to improve the MR effect of polyurethane-based MREs. The results show that when 6% wt CIP-Nano-Fe was added to the MRE, the MR effect was boosted and the damping property was significantly improved when compared to non-doped MREs. Lee et al (Lee et al. 2018) used rod-shaped hard magnetic $\gamma - Fe_2O_3$ particles as an addition in a CI particle-based natural rubber (NR) composite MR elastomer to improve the MR efficiency of CI-based MR elastomers. Under various magnetic field strengths, the MR characteristics of MR elastomers based on pure CI and CI@$\gamma - Fe_2O_3$ were examined using a rotational rheometer. According to the findings, the introduction of $\gamma - Fe_2O_3$ increased MR efficiency by 25%.

2.3   Synthesis of MRE Element

MREs are synthesised similarly to conventional polymer-based products. Due to the fact that silicone rubber, the most often used matrix material, is a liquid, MREs may be easily produced by combining silicone rubber with magnetic particles and other components. The mixture is typically prepared at room temperature and then let to cure in a mould. At high temperatures ($> T_m$), thermoset/thermoplastic polymers, such as silicone rubber, may readily interact with magnetic particles. In contrast, MREs have been made by utilizing NR, which is accessible as a solid phase or in immiscible polymer blends. Before mixing, such solid raw materials must often be transformed into a liquid or plastic condition. In this instance, a double roll mill and an extruder were employed to increase the dispersion of magnetic particles and matrix material. In a mould, the mixture is allowed to crosslink, cure, or vulcanize after correct mixing. After the mixture has completely dried, magnetic particles get entrapped inside the polymer network. The mould specifies the thickness and breadth of the MRE to be manufactured. Typically, mixing is performed at ambient temperature, while curing is performed at a

higher temperature to accelerate the crosslinking process. If the matrix material vulcanizes at normal temperature, curing may occur at room temperature; otherwise, curing will occur at greater temperatures. During the crosslinking procedure, magnetic particles are aligned in a certain direction using a magnetic field. Anisotropic MREs include magnetic particles that are oriented in a certain direction. During the crosslinking procedure, isotropic MREs are generated without the need of a magnetic field. In the case of isotropy, magnetic particles should be uniformly spread.

In an anisotropic MRE, the chains of magnetic particles, also known as pre-structuring or the formation of columnar structures, are revealed to be influenced by a number of parameters, including the magnetic field intensity, exposure duration, and temperature. Li et al. explored in detail the impact of varying these factors on the generation of anisotropic MREs (Li et al. 2008). If a greater magnetic field was applied, the samples would have a higher initial modulus. An increase in pre-structuring time would assist in the restraint of rubber and columnar structures. The moment at which the microstructure of rubber and magnetic particles ceases to move is the definition of saturation time. As the temperature increases, the viscosity of matrix materials reduces, making it simpler for magnetic particles to form columnar formations. By reducing the viscosity of matrix materials, additives such as plasticizers may also facilitate the creation of columnar structures. Lee et al. (Lee et al. 2019a) studied the influence of magnetic field strength during the production of anisotropic MRE and found that the MR effect is considerably greater for anisotropic MRE created with a magnetic field more than 1500 mT. Similar studies, such as those by Zhong et al (Zhong et al. 2019) and Samal et al (Samal et al. 2019), have been conducted to investigate the influence of the magnetic field on magnetic particle dispersion, but the optimal magnetic field strength has yet to be determined.

Magnetic force aligns magnetic particle chains parallel to the direction of the applied magnetic field, producing anisotropic MREs. By applying external energy derived from the magnetic force, magnetic particles seek to attain the minimal energy state (Kaleta et al. 2011). In contrast to isotropic MREs, in which particles are scattered evenly in space, anisotropic MREs need greater effort to deform along the direction of particle chains because the magnetic contact force between particles is stronger. Similarly, when the magnetic field is perpendicular to the chains of anisotropic MREs, the magnetic

interaction is enhanced, resulting in a higher relative MR effect (Li and Sun 2013). As a magnetic field is needed during the cross-linking process to make anisotropic MREs, a substantially greater amount of electricity is required to generate a greater magnetic flux. Similarly, it is difficult to manage the arrangement of magnetic particles inside the matrix material because magnetic particles can only be arranged in the direction of magnetic flux lines. As a consequence, it is difficult to produce a unique configuration, and none has been documented to yet. Isotropic MREs offer many benefits over their counterparts, including the absence of pre-structuring, the absence of a magnetic field during the crosslinking process, and uniform absorption qualities in a different direction. In contrast to anisotropic MREs, however, the MR impact is diminished.

Boczkowska et al. (Boczkowska and Awietjan, 2012) evaluated the impact of aligning particles in various directions and found that the samples with the greatest MR effect were aligned at an angle of 60 degrees. Similarly, Tian et al. (Tian and Nakano 2018) and Yao et al. (Yao et al. 2019) shown that altering the starting inclination angle for magnetic particle chains may influence the modulus and MR effect of MREs.

On the other hand, the literature has a number of attempts to create patterned MREs without employing a magnetic field. In 2008, Zhang et al. (Zhang et al. 2008b) manufactured the first patterned MREs. In their study, a lattice and a BCC structure were created as novel MREs. The findings were obtained by using particles with an average diameter of 400 μm. Similarly, another study (Forster et al., 2013) shown that MREs may be patterned without the need of a magnetic field. Utilizing a low-cost wax-cast moulding technique, an agglutinative MRE was constructed with an ultra-soft matrix. Zhang et al. (Zhang et al., 2008b) used patterned moulds to generate a range of patterned samples. This method is essentially comparable. The description of MRE structures ranging in size from a few millimetres to a few micrometres, accompanied by highly repeatable results, suggests that such patterned MREs may be used in biomedical engineering and microfluidic applications. Frequently, when creating patterned MREs without employing a magnetic field, a pre-defined mould is required. Even if such processes do not entail the utilisation of a magnetic field, extra stages and procedures are still required.
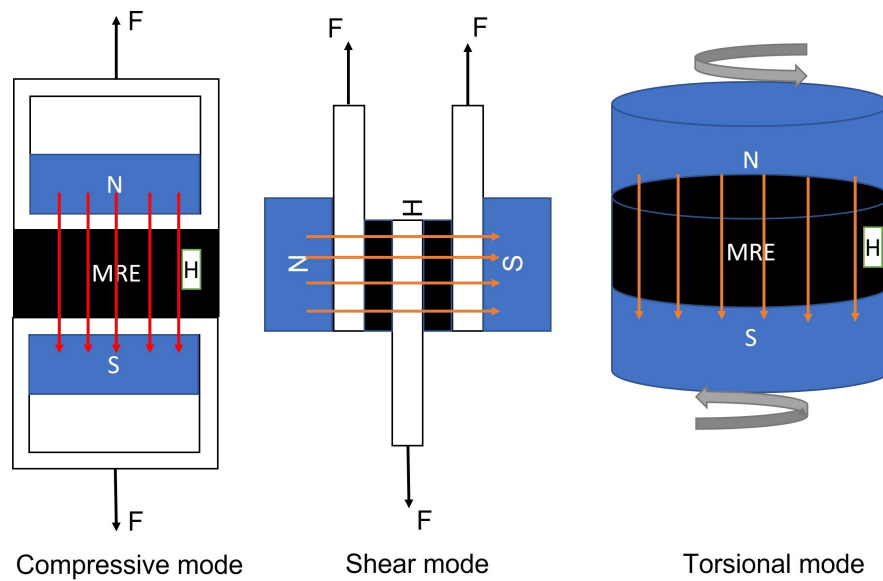
Figure 2.1: Basic working mode of the MRE isolator

2.4 MRE Isolator designs

Vibration isolation is an effective way to decouple the system from the source of vibration. It is achieved by inserting a resilient element referred as the vibration isolator between the vibration path. Based on the orientation of the resilient element and the direction of loading, the modes of operation of isolators are categorized as shear mode, squeeze mode and the mixed mode (Figure 2.1). The application of these isolators differs based on the system being isolated, and the frequency range of the source of disturbance. The shear mode offers a lower natural frequency and for the same cross section, the natural frequency of squeeze mode is higher. On the contrary, the mixed mode attains the attributes of both squeeze and the shear mode isolators.

MRE isolator is a type of passive isolator with a distinct resilient element that has the ability to vary the dynamic stiffness in response to the applied magnetic field. Like passive isolators, MRE isolator is also operates in shear, squeeze and mixed mode. However, these models are distinguished with respect to the direction of the applied load and the direction of the magnetic field. The compression or tensile mode constitute the squeeze mode and the shear mode of operation is either in translatory or oscillatory shear.

Tensile-compressive operation provides the most compact design in many axial loading applications, such as rotor systems, MRE bearing isolators in bridges, car suspension

systems, building isolators, and vertical vibration settings that cannot be controlled with MRE in shear mode due to its low stiffness capacity (Norouzi et al. 2017). The MRE isolator with mixed (The combination of compression and shear mode) operating mode MREs is more optimal than that of single mode, and performance of vibration isolation is improved in a large frequency range with applied current (Fu et al. 2013b). Li et al. (Li and Li 2013) created a laminated MRE isolator in shear mode, and testing revealed highly adjustable stiffness and damping capabilities. Yang et al. (Yang et al. 2015a) provided a theoretical model to analyze MRE isolators in shear–squeeze mixed mode, which demonstrated that the variable range for stiffness and damping of an MRE-based device in mixed mode was bigger than that of a single mode. The field-dependent features of shear working mode were noteworthy, and the regulating range was clear in a defined frequency range (Sun et al. 2015a) ; however, the phenomena of pre-strain existed due to gravity, and so the relevant engineering application was limited (Yang et al. 2015a). Large loading capacity may be produced for squeeze working mode; however, the regulating ranges of field dependent characteristics and frequency-shift range were significantly smaller than that of shear mode, limiting the working performance (Liao et al. 2013; Sun et al. 2015a). A few authors have reported on the torsional mode of MRE in various applications such as MRE absorber and isolator. However, the amount of shift achieved in torsion mode is much less than in other modes (Hoang et al. 2011, 2013; Lee et al. 2019b; Praveen et al. 2020).
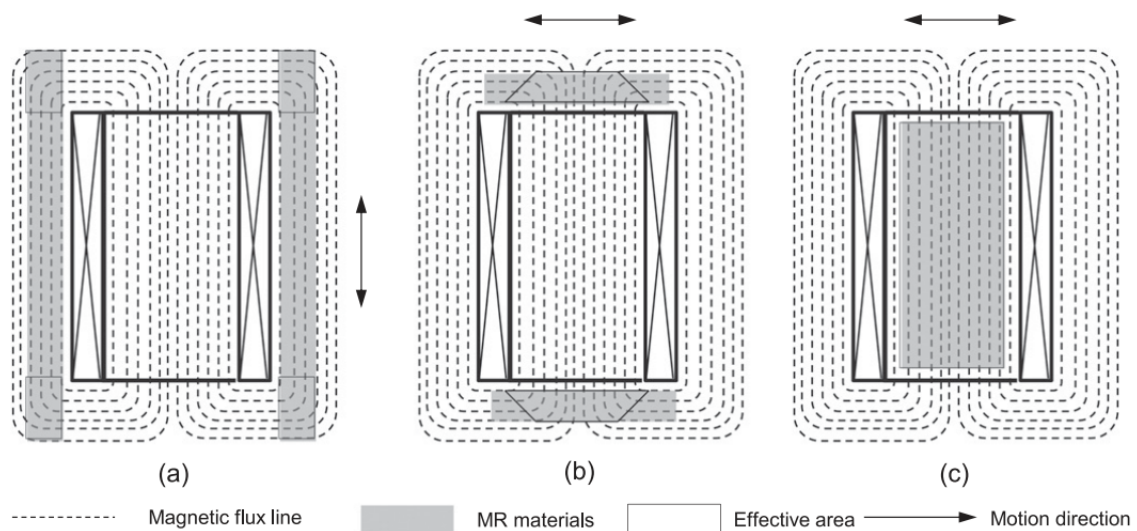
Figure 2.2: Configurations for magnetic circuit design(Li et al. 2014)

2.4.1 Magnetic circuit design of the MRE isolator

The performance of MRE isolator depends on the resilient element and its sensitivity to the applied magnetic field, which intern depends on the design of the magnetic circuit. Also, it is very important that the isolator should be adoptable to disturbances of wider frequency range. In practice there are three possible configurations for a magnetic circuit design in a MRE device (Figure 2.2a)). In the first arrangement, the field-sensitive material is placed outside of the magnetic coil. In this configuration the magnetic field strength exposed to the materials is less. Hence, extra magnetic coils are provided to enhance the magnetic field strength (Liu et al. 2021). The MR materials are closely placed on the top and/or bottom of the magnetic coil in the second type of magnetic circuit arrangement, depicted in Figure 2.2(b). This type configuration yields better magnetic field strength in the expose material compared to first configuration. Further, enhancing the field strength extra magnetic coil added at top or bottom of the magnetic coil(Behrooz et al. 2012).
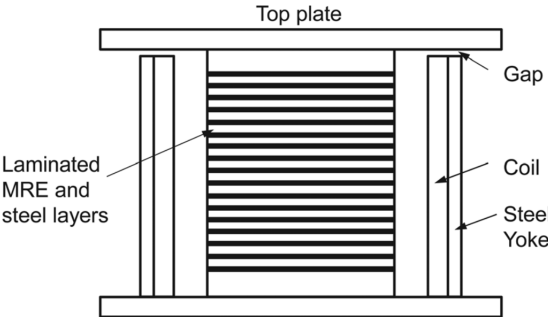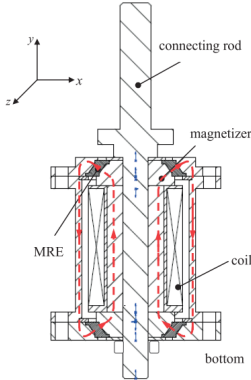
The MR materials can be inserted inside the magnetic coil in the third type of arrangement (depicted in Figure 2.2(c)), acting as the magnetic core of the magnetic circuit. The magnetic field inside the solenoid is strong and homogeneous, in contrast to the weak and divergent magnetic field outside the coil (Li et al. 2020; Li and Li 2015a; Sun et al. 2015b; Wahab et al. 2015; Xing et al. 2015; Zhao et al. 2017a). The most significant advantage of this design is that it has a huge active surface and a high magnetic field. A homogeneous magnetic field can fully energize the MR materials inside the solenoid. However, due to the poor permeability of the MR elastomer material, extra precautions should be taken to increase the permeability of the magnetic core, which contains the MR materials.

Other than above three configurations, a hybrid design contains permanent magnets in the existing configurations in which magnetic field can be boosted or diminished toward the existing magnetic field generated by permanent magnetics by adding a positive and negative current. This results, the MR device possess changing the stiffness into negative and positive, which gives the advantage of wide range of natural frequency shift (Liu et al. 2020; Yang et al. 2014). Such a design is especially useful when a specific stiffness is necessary for the device to retain serviceability and structural stability.

2.4.2 Existing MRE isolator Designs
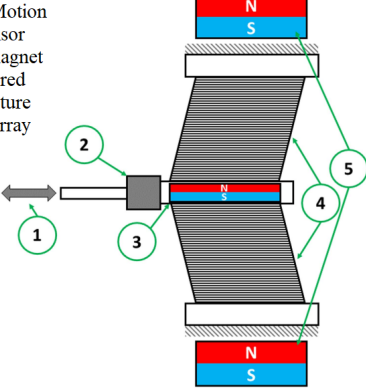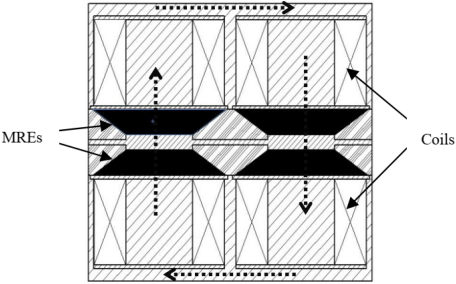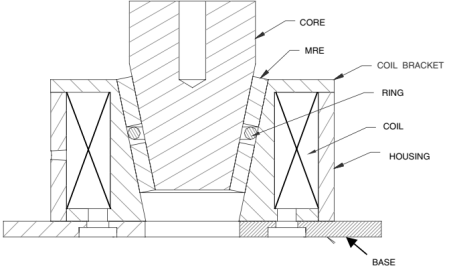
There are various MRE isolator designs provided by researchers which are intended to reduce the force or displacement vibration in the receiver. These isolator's efficiencies mainly depend on working mode of the MRE, payload of the receiver, the amount of stiffness increase in the MRE (MR effect) isolator, the magnetic field generation in the material, and the amplitude of excitation. So, the literature work focuses on various designs of the MRE isolator and its capabilities represented in a Table 2.1.

Table 2.1: Various isolator devices designed in the literature

Device	Specification
	Device: MRE seat isolator **Author:** (Li et al. 2012) **Input amplitude excitation:** 10 mm **Inertia mass:** 86 kg **Max change of stiffness:** 300% **Current input:** 0 A to 3 A **Working mode:** Both shear and squeeze mode
	Author: (Tao et al. 2018a) **Input amplitude excitation:** 1g and 2g **Inertia mass:** 2.1 kg **Max change of stiffness:** 66.57% **Max change of Damping:** 45.55% **Current input:** 0 A to 2.5 A **Working mode:** squeeze/elongation–shear mode
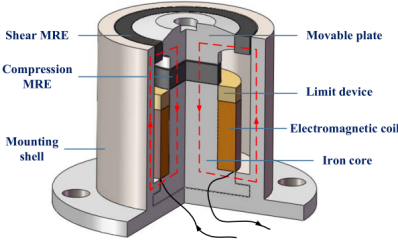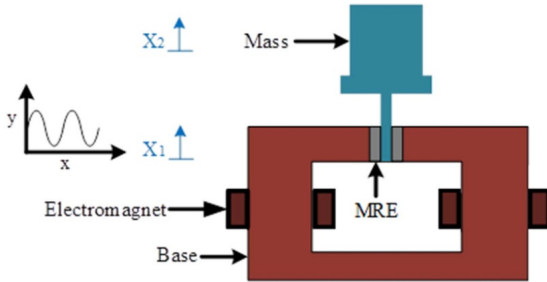
Table 2.1 – continued from previous page

Device	Specification
1. Relative Motion 2. Force Sensor 3. Internal magnet 4. MRE layered isolator structure 5. Halbach array	**Author:** (Przybylski et al. 2016) **Input amplitude excitation:** : 1 mm and 4 mm **Inertia mass:** 2.1 kg **Max change of stiffness:** 81.13% **Max change of Damping:** 148.12% **Magnetic magnetic:** -49.86 mT to 162.01 mT **Working mode:** Shear mode
MREs / Coils	**Author:** (Behrooz et al. 2012) **Input amplitude excitation:** : 0.1 g **Inertia mass:** 68 kg **The natural frequency change**: 43 Hz to 51 Hz **Current input**: 0 A to 3 A **Working mode**: Shear mode
CORE / MRE / COIL BRACKET / RING / COIL / HOUSING / BASE	**Author**: (Li et al. 2012) **Input amplitude excitation**: 10 mm **Inertia mass**: 86 kg **Max change of stiffness**: 300% **Current input**: 0 A to 3 A **Working mode**: Both shear and squeeze mode
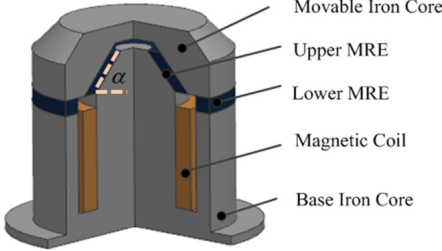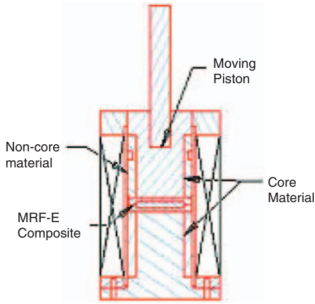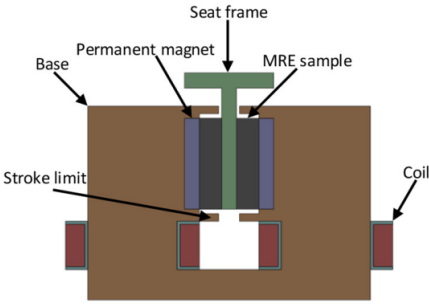
Table 2.1 – continued from previous page

Device	Specification
	Author: (Fu et al. 2013b) **Input amplitude excitation**: 0.045mm, 0.09mm and 0.135 mm **Inertia mass**: 1.2 kg **Max change of stiffness**: 175% **Max change of Damping**: 216% **The shift of natural frequency**: 45.82 Hz to 82.55 Hz **Current input**: 0 A to 1.5 A **Working mode**: Both shear and squeeze modes
	Author: (Liu et al. 2021) **Input amplitude excitation**: 2 mm **Inertia mass**: 30 kg **Max change of storage modulus**: 47.79 kPa to 200.02 kPa **Max change of loss modulus**: 10.10 kPa to 60.66 kPa **Magnetic field**: 0 T to 0.8 T **Working mode**: Shear mode
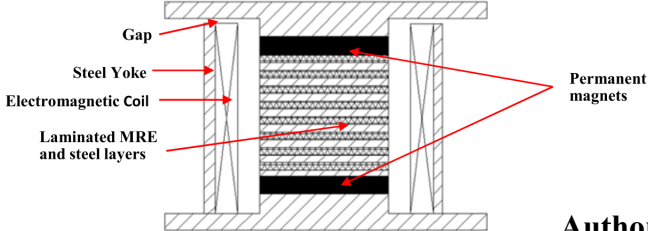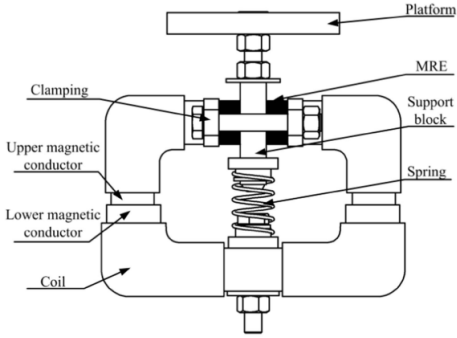
Table 2.1 – continued from previous page

Device	Specification
	Author: (Leng et al. 2018a) **Input amplitude excitation**: 2 mm **Compression modulus and shear modulus change**: 25% and 20% **Current input**: 0 A to 2 A **Max isolation of vibration**: 39% **Working mode:** in shear and compression mode
	Author: (Liu et al. 2021) **Input amplitude excitation**: 0.1 mm and 0.6 mm **Max change of damping coefficient ceq** : 10.10 kPa to 60.66 kPa **Current input**: 0 A to 3 A **Working mode**: Shear mode
	Author: (Liu et al. 2020) **Input amplitude excitation**: 8.7 mm **Max change of storage modulus**: 75 kPa to 225 kPa **Max change of loss modulus**: 15 kPa to 65 kPa **Magnetic field**: 0 T to 0.6 T **Working mode**: Shear mode
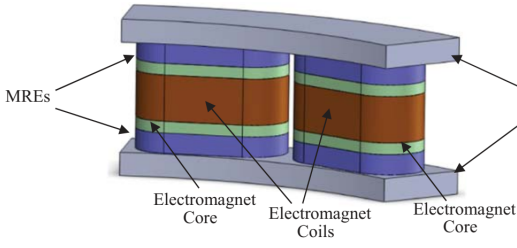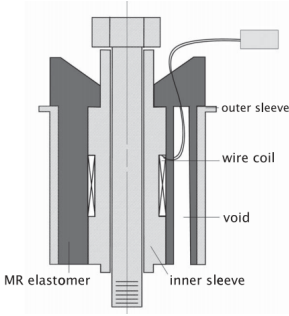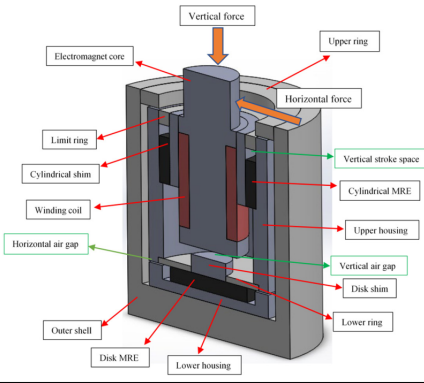
Table 2.1 – continued from previous page

Device	Specification
	Author: (Yang et al. 2014) **Input amplitude excitation**: 8 mm **Max change of stiffness**: 5.31 KNm-1 to 1.88 KNm-1 **Max change of damping**: 0.21 to 0.08 **The natural frequency change**: 9.85 Hz to 4.20 Hz **Current input**: -4 A to 4 A **Working mode**: Shear mode
	Author: (Du et al. 2017) **Input amplitude excitation**: 2 mm **Inertia mass**: 0.7 kg **Max change of stiffness**: 55.11 Nmm-1 **Max change of damping coefficient**: 84.5 N.sm-1 **Current input**: 0 A to 2 A **Working mode**: Shear mode
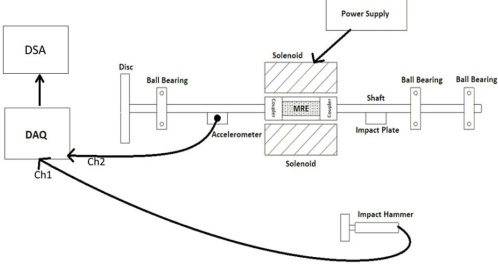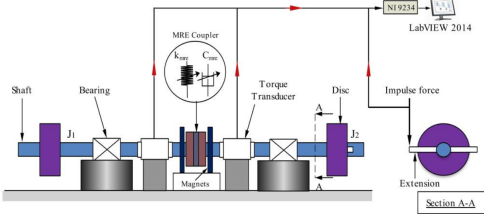
34

Table 2.1 – continued from previous page

Device	Specification
	Author: (Kavlicoglu et al. 2011) **Input amplitude excitation**: 5 g **Max change of stiffness**: 27% **Input current**: 0 A to 5 A **Max isolation of vibration**: 32% **Working mode**: compression
	Author: (Ginder et al. 2000) **Input amplitude excitation**: 1 mm **Max change of stiffness**: 25% **Input current**: 0 A to 5 A **Working mode**: Torsional
	Author: (Jalali et al. 2020) **Input amplitude excitation**: 0.24, 0.48, 0.96, 1.5 and 1.92 mm **MR effect**: 35% and 27% in the vertical and horizontal **Magnetic field**: 0 to 0.22 T **Working mode**: Shear mode

35

Table 2.1 – continued from previous page

Device	Specification
	Author: (Syam et al. 2021) **Max change of stiffness**: 164.7% **The shift of natural frequency**: 26 Hz to 28 Hz **Magnetic field**: 0 to 0.0122 T **Working mode**: Torsional mode
	Author: (Praveen et al. 2020) **Input amplitude excitation**: 0.002 to 0.016 rad **Max change of stiffness**: 9.96% **The shift in the torsional natural frequency**: 1 Hz (12 Hz to 13 Hz) **Input current**: 0 A to 5 A **Working mode**: Torsional mode

2.5   Designing parameters of an MRE isolator

The parameters that are critical for the design of MRE isolator are modulus of MRE, permeability of MRE and its response time. The ability of MRE isolator to withstand the applied load is governed by the modulus. Any enhancements in modulus under the applied field are with respect to modulus of MRE under the passive state. The modulus of MRE is a complex quantity as it inherits properties from its viscoelastic matrix. The complex modulus defines the ability of MRE to store and dissipate the energy. The distinctive feature of MRE is its ability to enhance the modulus in response to the magnetic

field. The amount of shift in the modulus depends on the sensitivity of the MRE, which in turn depends on its permeability. The permeability also aids in analyzing the magnetic circuit of an MRE device. The response time of MRE is defined as sum of the time taken by the electromagnetic coil to generate magnetic-field and time required to induce the changes in the properties of MRE. Response time is a critical parameter that need to be addressed while implementing the real time control strategies of MRE isolator. The following section briefly explains the parameters that need to be considered while designing the MRE isolator.

2.5.1 Modulus enhancement of MRE isolator in response to the magnetic field.

The ability of MRE isolator to adopt a wide range of frequencies of disturbance depends on the amount of modulus change in response to the external magnetic field. A larger variation in modulus results in a greater shift in natural frequency. On the contrary, the MRE isolator which could offer lesser variations in the modulus are not ideal to achieve wide frequency range of isolation. Therefore, it is very important that the device should yield larger variations in the filed induced modulus. This property depends on the initial modulus of the unfilled matrix, the properties of fillers and the effects induced under the filled state of the elastomer. However, these aspects are related to microscopic details, and will be addressed separately. This section deals with the analysis of magneto induced modulus of MRE and the different approaches employed to model this attribute.

The magneto induced modulus of MRE is determined by the initial modulus at zero magnetic field and the enhancement in the modulus under the influence of magnetic field. The magneto-induced modulus is an index that can be used to determine the range of stiffness change. To create high-performance MREs, it is critical to investigate how different material properties affect the magneto-induced modulus theoretically. The estimation of modulus is usually done through the dipole model. Dipole models for MR material are based on the magnetic dipole theories and the overall effect is the inter particle dipole interactions averaged over entire sample. Jolly et al(Jolly et al. 1996a) proposed a one-dimensional quasistatic model in which the particles are assumed to be uniform, homogeneous spheres with identical induced dipole moments. The theoretical model assumes that particles are aligned in perfect chains and that quasi-static shear

strains and associated stresses are distributed uniformly along each particle length of the chain. Maximum field-induced stress increases quadratically with particle saturation magnetization J_p, which is expressed as,

$$G = \frac{\varphi J_P^2}{2\mu_0\mu_1 h^3} \qquad (2.1)$$

where, the permeability of the elastomer is μ_1, the permeability of the vacuum is μ_0, φ is the volume fraction of magnetic particles and $h = \frac{r_0}{d}$, the distance between the particle is r_0 and the diameter of the particle is d.

Shen et al. (Shen et al. 2004) developed a model which is different from Jolly et al. (1999) model. The author considers all the magnetic dipole interactions of particles in the single chain, unlike the interaction between the adjacent particle and the assumptions considered is as same as that of Jolly et al. (Jolly et al. 1996a). The resultant equation shows that the shear modulus change is quadratically proportional to the value of dipole moment.

$$\delta G = \frac{9}{8}\frac{\varphi C m^2 (4 - \gamma^2)}{r_0{}^3 \pi^2 a^2 \mu_0 \mu_1 (1 + \gamma^2)^{7/2}} \qquad (2.2)$$

where, a is the particle radius, m is the dipole moment and the shear strain is γ. Davis (Davis 1999a) proves, using the dipole model theory and the finite element method, that an optimal volume fraction of a filler material is around 27% and that the change in modulus at saturation level is equal to 50% of the initial modulus. From the simple dipole model (regard the aggregation as a dipole), the increase in the shear modulus δG can be expressed as

$$\delta G = 4.808 \varphi \mu_0 \left(\frac{R}{d}\right)^3 M_s{}^2 \qquad (2.3)$$

where, R is the radius of the particle, d is the distance between the particles and M_s is the saturation magnetization.

Zhang et al (Zhang et al. 2008a) proposed a new effective permeability model that takes particle saturation into account to explain the field-induced modulus of MREs with complex structure and components.

$$\delta G = \frac{3}{2}\varphi \mu_m \mu_0 H_0{}^2 \left(\frac{2 + \varphi_n}{1 - \varphi_n}\right) \qquad (2.4)$$

where, H_0 is external magnetic field and φ_n is the volume fraction of nanoparticles in

soft shell.

Gong et al (Gong et al. 2005a) suggested a basic self-assembled microstructure model. This type of microstructure is made up of additive and scattered particles in the matrix. When this type of MRE is exposed to a magnetic field, the particles in the microstructure become magnetised and move somewhat due to the additive's lubrication to form a regular structure, resulting in a strong MR effect. According to the theory, modulus changes.

$$\delta G = \frac{36\sqrt{2}\varphi\mu_1\mu_0\beta^2 H_0{}^2 \left(\frac{R}{d}\right)^3 \zeta}{2 - \beta} \qquad (2.5)$$

where, $\beta = \frac{(\mu_p - \mu_m)}{\mu_p} + 2\mu_m$, ζ is the constant.

Yao et al. (Yao et al. 2019) developed a hypothesis of magnetic dipoles and magnetic field coupling between particles aligned in chains to explain the micromechanical interaction between particles in magneto-rheological elastomers. The model results demonstrate that the magneto-induced shear storage modulus of MREs is strongly dependent on the internal particle chain's initial inclination angles. The change in the modulus according to the theory

$$\delta G = \frac{2\varphi A \mu_0 \mu_1 \left(\frac{a}{r_0}\right)^3 K}{Y} \left[\frac{\chi H_0}{1 - 2C\chi \left(\frac{a}{r_0}\right)^3 cos^5\theta + \frac{2}{3}C\chi \left(\frac{a}{r_0}\right)^3 cos^3\theta} \right]^2 \qquad (2.6)$$

where, χ is the susceptibility of the iron particles, the angle between the particle chain and the applied magnetic field is θ, K and A are constants.

2.5.2 Magnetic permeability of the MRE

To design a magnetic circuit for MRE isolator, it is important to know the relative permeability of the MRE. The relative permeability value of MRE mainly depends on the particle volume fraction. Increasing the particle volume fraction increases the permeability of the MRE. The filler particle orientation within the matrix has a direct impact on its permeability (Ivaneyko et al. 2014b; Kärkkäinen 2000; Varga et al. 2006). Numerous efforts have been made to accurately predict the macroscopic behaviours of MREs by observing particle distributions in MREs (Biller et al. 2014; Danas et al. 2012; Jolly et al. 1996b; c; Zhang et al. 2010; Zhou et al. 2015; Zhu et al. 2006) Various methods

are applied to calculate and measure the permeability of materials (Biller et al. 2014; Danas et al. 2012; Ivaneyko et al. 2014a; Jolly et al. 1996b; c; Zhang et al. 2010; Zhu et al. 2006). Maxwell-Garnet equation is usually used to evaluate the permeability of composites with simple internal structures. In addition, it assumes that the magnetization of particles is linear, and the interaction of particles is neglected. However, the magnetization of ferromagnetic particles is non-uniform in the magnetic field (Jolly et al. 1996b). Maxwell Garnet mixing rule, the relative permeability of MRE can be obtained

$$\mu_{eff} = \mu_m + 2\varphi\mu_m \frac{\mu_p - \mu_m}{\mu_p + \mu_m - \varphi(\mu_p - \mu_m)} \tag{2.7}$$

where, μ_m and μ_p are permeability of the matrix and particle and φ is the volume fraction of the particle.

Tao et al (Tao et al. 2019) provided a theoretical and experimental technique to measure the permeability of the MRE.

2.5.3 Response time of the MRE isolator

MRE response is adaptive, allowing it to alter the stiffness and damping of a vibratory system, preventing or attenuating resonant vibrations. MREs have a very quick response time, which is defined as the time it takes for an MRE to respond to a magnetic field given to it. Zhou and Jiang (Zhou and Jiang 2004) discovered that the response time of MRE is substantially smaller than a few tens of milliseconds (ms). According to Fu et al (Fu et al. 2013a), the response time of an MRE buffer under impact loading is 7 ms. Nguyen and Ramanujan (Nguyen and Ramanujan 2010) discovered that for big displacement, the response time of an MRE is 60 ms. As a result, adjustable mechanical properties of the MRE, along with their fast temporal response, make them appropriate for a wide range of engineering applications, including adaptive tuned vibration absorbers (ATVAs), isolators, sandwich beams, and actuators.

The key to unlocking unique properties of the MRE materials, such as instantly adjustable shear modulus in both directions is required for real-time control of the MRE isolators. When employing a smart device based on MRE, the response time of the magnetorheological elastomer (MRE) material is the most important factor that influences control performance of the vibration system. As the current increased, the response time

decreased and increased in a trend in the rise and fall edge (Zhu et al. 2018). The response time for compression mode MRE increases as the compression strain for the rise and fall edge increases (Zhu et al. 2018). The initial and transient change in normal force to a higher strain was also higher. When comparing the response time of anisotropic MRE to that of isotropic MRE, anisotropic MRE outperforms isotropic MRE (Zhu et al. 2018). Gu et al. (Gu et al. 2016) offered two methods for lowering reaction time of the MRE isolator. The first method is to stack the huge coil with multiple identical coils, and the second method is to use field quenching to remove the leftover magnetic field. The updated design was discovered to minimize the reaction force time from 421 ms to 52 ms in the rising and from 402 ms to 48 ms in the dropping. With increasing content of CIP@FeNi, the characteristic response time on the rise edge shows a clear decrease trend (Li et al. 2021a). By considering the response property of MRE material, Zhu et al (Zhu et al. 2019) investigated the response time of a shear mode MRE isolator to step excitations. The experimental results showed that the larger step-up current has a faster response time at the rise edge, while the smaller step-down current has a better response time at the fall edge. Furthermore, the amplitude of shear strain has a smaller impact on response time of the MRE. Chen et al. (Chen et al. 2020) showed that adding conductive multi-wall carbon nanotubes (MWCNTs) particles increases conductivity and decreases response time.

2.6   Performance assessment of the MRE isolator

Vibration isolators are used to reduce the transfer of vibrational energy between the structural systems. For effective use of MRE isolator in a specific vibration isolation application, its stiffness and damping properties has to be experimentally characterized as a function of magnetic field, amplitude of excitation and frequency. For that, an experimental setup is required to characterize MRE. According to ISO 10846-1, there are three methods such as Direct Method (Poojary et al. 2016), the Driving Point Method (Ooi and Ripin 2014) (Esmaeeli et al. 2019; Zainudin et al. 2020), and the Indirect Method(Richards and Singh 2001) (Boote et al. 2014) (Phu and Choi 2015) can be used to design any experimental setup(Iso 2009). Among these three methods, the Direct Method has the widest effective frequency range (Poojary et al. 2016). There are alternative methods such as impact hammer (Lin et al. 2005; Ooi and Ripin 2011),

force/displacement transmissibility (Hegde et al. 2015) and free vibration test available (Levent et al. 2003; Ramanauskas et al. 2010) to estimate dynamic properties of isolator, which is going to discussion in detail in the following paragraphs.
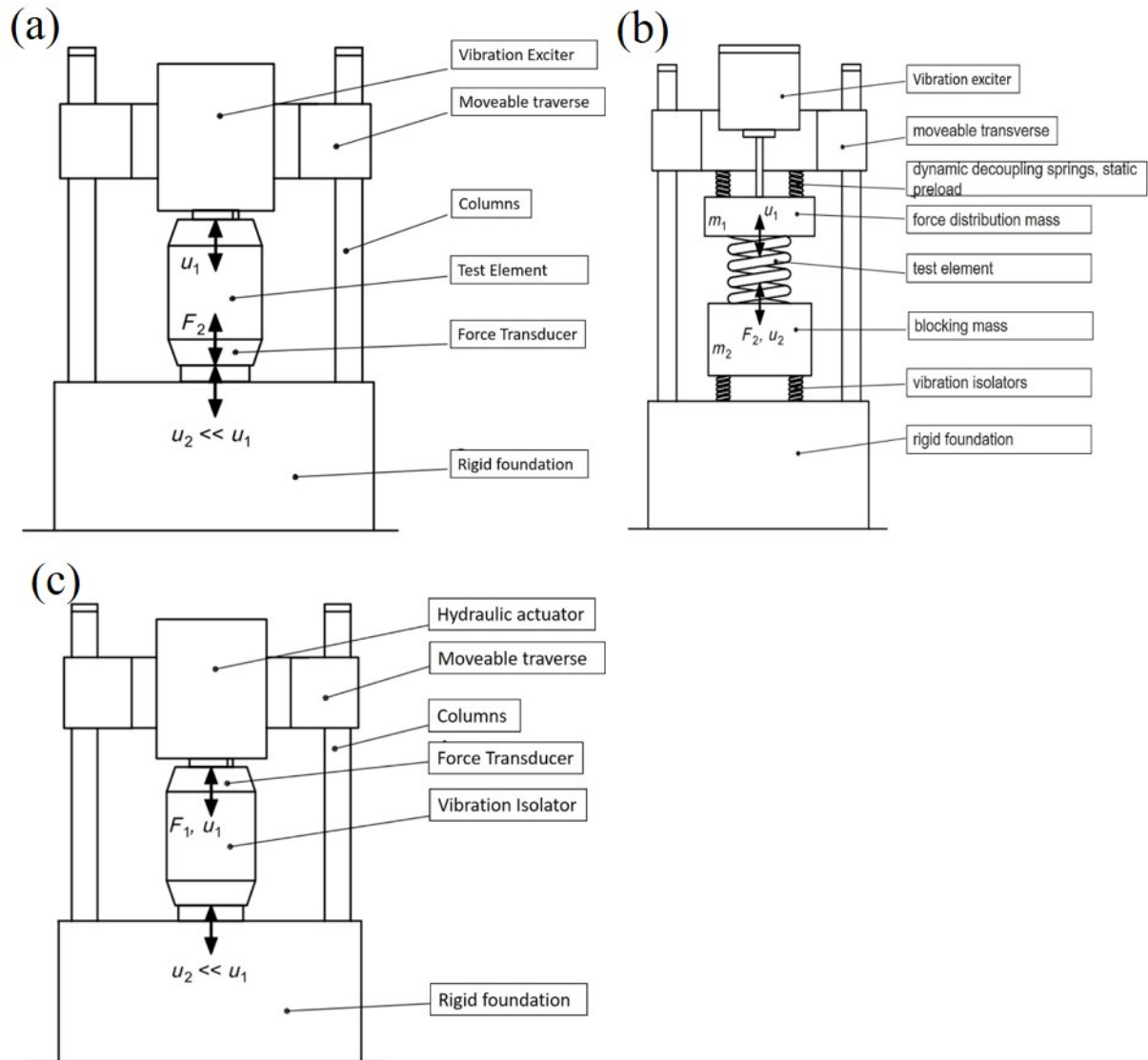
Figure 2.3: ISO 10846-1 method of testing the isolator element (a) Direct Method (b) indirect method (c) driving point method (Iso 2009)

2.6.1 ISO standards for testing the isolator

Direct Method:

Figures 2.3(a) show a schematic representation of the isolator property measurement approach using the direct stiffness method. To position the vibration exciter vertically

for different levels, it is connected to a moveable traverse. The vibration exciter and foundation are separated by the isolator test element. Displacement and Force sensors are installed in the test setup to measure excitation displacement and force transfer to the foundation in order to determine isolator properties. After collecting the measurement data, dynamic stiffness is calculated using the following expression (Poojary et al. 2016).

$$K^* = (K' + iK'') = \frac{F_2}{u_1} \tag{2.8}$$

where, K^* represents the dynamic stiffness. The real and imaginary part of dynamic stiffness is calculated as

$$K' = \frac{F_2}{X_0} \cos\delta \text{ and } K'' = \frac{F_2}{X_0} \sin\delta \tag{2.9}$$

The loss factor of a resilient element can be estimated according to

$$\eta = \tan(\delta) \tag{2.10}$$

The frequency range of validity of the direct method is mainly determined by the test rig properties. The upper frequency limit of the Direct Method can be as high as 500 Hz while for lower frequency limit is around 1 Hz (Iso 2009).

Indirect Method:

In the indirect method, the blocking force is not directly measured. Instead, it is figured out by measuring the acceleration of the blocking mass, which is separated from the test rig chassis in a way that is shown in Figure 2.3(b). A small mass, called m_1 "excitation mass" stands between the sample being tested and the source of vibration. The function of the excitation mass is to provide the contact point at the input side of the sample being tested. As the blocking mass, it is dynamically decoupled from the structure of the test rig by using auxiliary isolators. The so-called blocking mass is put under the test sample. It gives the output side of the isolator a high-stiffness contact point, so that the forces between the output side of the isolator and the receiving mass are about the same as the blocking forces. The blocking mass must have a high rotational and translational inertia, and its decoupling isolators should have a low enough stiffness to keep the mass's six

43

rigid motions from resonating at high frequencies(Richards and Singh 2001)(Boote et al. 2014)(Phu and Choi 2015).

$$K^* = (K' + iK'') = \frac{F_2}{u_1} = -(2\pi f)^2 m_2 \frac{u_2}{u_1} \qquad (2.11)$$

where, f is the frequency of the mass/spring system formed by m_2 and the test element.

Typical frequency range in the indirect method of designing the experimental setup is between 20 Hz to 50 Hz for stiffer mounts and it is 2 kHz to 5 kHz which depends on the test rig(Iso 2009).

Driving point method:

The driving point method employs the same test setup as the direct method. However, the force on the input side is measured rather than the force on the output side (Figure 2.3(c)). As a result, the dynamic transfer stiffness is determined using the driving point method by assuming that, at low frequencies, it is nearly equal to the driving point dynamic stiffness because inertial forces are negligible in comparison to elastic forces, that is (Iso 2009),

$$K^*_{direct} \approx K^*_{driving} = (K' + iK'') = \frac{F_1}{u_1} \qquad (2.12)$$

The Equation is only valid at low frequencies (typically $f < 200$ Hz), when the inertial forces are small compared to the stiffness and damping forces. The dynamic mechanical analyser (DMA) and rheometer test setup for MRE isolator works on this method to estimate the dynamic properties (Esmaeeli et al. 2019; Rahman et al. 2018). Other Methods of testing the isolator
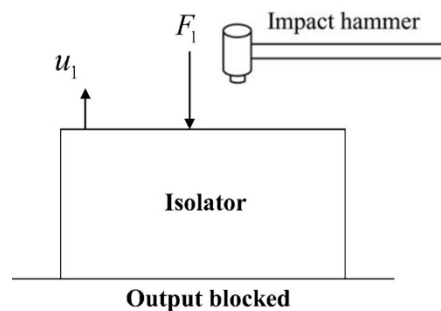
Figure 2.4: Impact Hammer test

44

2.6.2 Impact Hammer

This test-setup for finding dynamic properties is much simpler in construction comparative other methods (Figure 2.4). In this test setup, isolator is fixed to the base in the one end and the other end open for providing the impact excitation. The dynamic properties of the rubber block are determined directly by fast Fourier transform (FFT) of the measured impact force and displacement at the free end of the setup (Lin et al. 2005; Ooi and Ripin 2011) The complex receptance function of the SDOF system can be written as (Lin et al. 2005; Ooi and Ripin 2011)

$$\bar{R} = \frac{\widetilde{x}}{\widetilde{F}} = \frac{1}{k[1 - r^2 + j\eta]} \tag{2.13}$$

where, the variable $r = \frac{\omega}{\omega_n}$ is the frequency ratio and $\omega_n = \sqrt{\frac{k}{m}}$ is the natural frequency of the SDOF system, which is determined from the measured frequency response function. The real and imaginary parts of the complex receptance are readily available from and are given by (Lin et al. 2005; Ooi and Ripin 2011)

$$Re\,(\bar{R}) = \frac{1 - r^2}{k[1 - r^2 + \eta^2]} \tag{2.14}$$

and

$$Im\,(\bar{R}) = -\frac{\eta}{k[1 - r^2 + \eta^2]} \tag{2.15}$$

The following relations for the rubber mount stiffness and damping as functions of frequency can be obtained from Eqs.

$$\eta = -\frac{Im\,(\bar{R})}{Re\,(\bar{R})}\left(1 - r^2\right) \tag{2.16}$$

and

$$k = \frac{Re\,(\bar{R})}{|\bar{R}|^2\left(1 - r^2\right)} \tag{2.17}$$

where, $|\bar{R}|$ is the absolute value of the complex receptance. One advantage of the proposed method is that the rubber mount stiffness and damping can be determined without knowing the exact mass of the system, which is often difficult to quantify in such measurements since the rubber element has distributed mass and stiffness (Lin et al. 2005; Ooi and Ripin 2011).
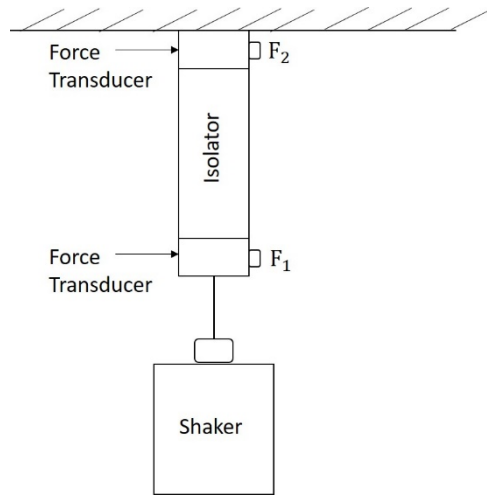
Figure 2.5: Transmissibility Test

2.6.3 Force or displacement Transmissibility

As seen in Figure 2.5, the isolator is positioned between the fixed end and the shaker. Two force transducers are used to evaluate the input excitation force and the amount of force transferred to the structure. The ratio between the output force and the input force to an isolator called the transmissibility. The isolator's transmissibility might be force or displacement. When the device must be shielded from vibrations originating at the site of connection, displacement transmissibility is chosen. The force transmissibility (FT) is the ratio of force at the output side to force at the input side (Hegde et al., 2015), and it is taken into account while isolating the source of vibration from the system of interest. Both techniques have the same response function, but their systems of reference are distinct (Rao 2011). After calculating the transmissibility, the frequency with the highest transmissibility value was established. This frequency corresponds to the SDOF natural frequency of the system, where the phase delay between the base and mass reaches 90° degrees. Consequently, the stiffness of the system can be determined using the equation, whereas the damping ratio may be determined as follows:

$$\xi = \frac{\Delta\omega}{2\omega_n} \tag{2.18}$$

where, $\Delta\omega$ is the frequency difference when the response amplitude is equal to $\frac{T_{max}}{\sqrt{2}}$ of the peak response amplitude

46

2.6.4 Free vibration test method:

In this method, the isolator is fixed to the base and the free end of the isolator is excited with external source for limited time. The movement of isolator body for the given excitation is measured using accelerometer. For the measured signal, the FFT of the measured signal is analysed. Frequency transfer function used to determine the damping ratio. The Q-factor, which measures the sharpness of resonant peak, is defined by(Levent et al. 2003)(Ramanauskas et al. 2010)

$$Q = \frac{\omega_r}{\Delta\omega} = \frac{1}{2\zeta} \tag{2.19}$$

where, ω_r damped natural frequency of the system, ζ damping ratio and, $\Delta\omega$ is the frequency difference when the response amplitude is equal to $\frac{T_{max}}{\sqrt{2}}$ of the peak response amplitude The natural frequency of the isolator is given by

$$\omega_n = \frac{\sqrt{1 - 2\zeta^2}}{\omega_r} \tag{2.20}$$

2.7 Factors contributing to the performance of MRE isolator

The performance of an MRE isolator is determined by magnetic field, temperature, pre-compression, excitation amplitude, and frequency. To develop a mathematical model and control implementation for an MRE isolator, its performance under these factors must be comprehended. This section describes how operational variables impact the performance of an MRE isolator.

As discussed earlier, the MRE isolator stiffness is control by magnetic field. The applied magnetic field can be homogeneous and non-homogeneous with intensity of-magnetic fields between 0 T and 1 T. (Fan et al. 2011; Jolly et al. 1996). The non-homogeneous magnetic field magnetises just a section of the MRE, while the homogeneous magnetic field magnetises the full geometry of the MRE (Hu et al., 2011). (Stepanov et al. 2009). Utilizing the unique field-induced characteristics effectively is facilitated by the uniform magnetic field.

The storage modulus of MRE increases proportionally with the magnetic field strength. At a magnetic field strength of less than 0.1 T, the property improvements are insignificant (Hu et al., 2011), but these modifications become more evident as the magnetic

field intensity rises (Lokander and Stenberg 2003) However, these properties improvements come at the price of a loss in linear features (Stepanov et al. 2007). In the absence of a magnetic field, the stress-strain relationships are rather linear, but as the magnetic field strength rises, the linear range of MRE diminishes. Furthermore, the field-induced increases are minimal at higher magnetic fields because MRE is magnetically saturated. In addition, the increase in magnetic field strength has no impact on particle attraction after particle saturation (Lokander and Stenberg 2003). According to prior studies, the range of 0.3 T to 0.8 T is seen for saturation magnetization depending on the matrix type (Chen and Gong 2008; Chen et al. 2007).

Like storage modulus, the damping characteristics of the MRE are also sensitive to the magnetic field. But, variations in field-dependent damping documented in prior literatures are conflicting. Few investigations have indicated that when the magnetic field rises, the damping properties of MRE improve. Several investigations have also shown that strengthening the magnetic field decreases the loss factor (Gong et al. 2012a). Lokander and Stenberg (2003a) report that the field-induced change in MRE damping characteristics is insignificant (Lokander and Stenberg 2003). Few investigations have shown that the loss factor peaks between 0.25 T and 0.4 T magnetic fields (Abdul Aziz et al. 2017). The literature reported that contributions of interface damping and magneto-mechanical damping affect the fluctuations in field-induced damping characteristics, however the impact of magneto-mechanical damping is insignificant compared to that of interface damping (Chen et al. 2016, 2008a). As the magnetic field strength on MRE increases, the particle-matrix interface pressure rises, resulting in a decrease in damping for magnetic fields between 0.3 T and 0.4 T (Rabindranath and Bose, 2013).

Pre-compression has a substantial effect on the magnetic and nonmagnetic characteristics of MRE (Lejon and Kari 2009; Zhu et al. 2012). The magnetic poles are positioned above and below the MRE sample to activate it in compression and tension modes. The initial modulus of MRE in its pre-compression or pre-tension condition has a greater value than its non-compression initial modulus. Upon application of a magnetic field, the stiffness of both forms of MRE will increase since there is less space between the particles in their pre-compressive condition (Psarra et al. 2019; Wang et al. 2011). However, the overall MR effect of MRE will be diminished in the pre-loading condition owing to the bigger zero field modulus in the compression state and the lesser

magnetic field strength between the magnetic poles in the tensile state (Psarra et al. 2019; Wang et al. 2011).

Temperature is one of the most crucial influences on the performance of polymer materials. MR elastomer-based devices usually function across a broad temperature range. Consequently, it is essential to examine the influence of temperature on the mechanical characteristics of MR elastomers. So far, little study has been conducted on the temperature-dependent performance of MR elastomers. Zhang et al. (2011) examined the mechanical characteristics of MR elastomers with a mixed rubber matrix (cis-polybutadiene rubber and natural rubber). The results demonstrated that the temperature-dependent moduli of MR elastomers with various rubber matrices have distinct features. Lejon et al. (Lejon and Kari, 2013) determined the relationship between the dynamic shear modulus of magneto-sensitive (MS) elastomers and temperature, dynamic strain amplitude, magnetic field strength, and frequency. The measurements revealed that temperature had a greatest influence on the parameters, particularly when the temperature reached transition phase of the material. Wan et al. (Wan et al., 2018) observed that the transition temperature of MR elastomers was around 50°C and that the storage modulus first declined with rising temperature, reaching its lowest value at 50°C before continuing to rise with increasing temperature.

MRE has rate-dependent properties inherited from its relaxation qualities. Typically, the frequency dependent features of MRE are characterised between 1 Hz and 100 Hz (Tian et al. 2011; Yunus et al. 2016). For any structural vibration control application, the viscoelastic response up to 80 Hz is necessary (ISO 10846). Previous study has shown that the storage modulus of MRE increases with frequency (Chen and Jerrams 2011; Gong et al. 2012a). Consequently, a higher loading frequency leads to a greater storage modulus. The difference is attributed to mismatch in velocity between the slower movement of polymer chains and the stimulation frequency (Chen et al. 2008b). In MRE, frequency dependence may be represented by the strain rate effect. At lower frequencies, the strain rate impact is exponentially magnified, but not so much at higher frequencies (Koo et al. 2009). This suggests that the influence of frequency is considerable at low frequencies (less than 5 Hz) but lessens progressively as frequency increases (Li et al. 2010). In addition, the field-induced improvements indicated by the absolute MR effect are independent of frequency (Chen et al. 2007; Damiani and Sun

2017; Lokander and Stenberg 2003). In contrast, the relative MR impact is frequency dependant.

The damping characteristic of MRE is frequency dependent. As frequency increases, the loss modulus of MRE demonstrates an upward trend (Tian et al. 2011). However, the loss factor reduces when the storage and loss modulus rise in tandem with an increase in frequency. Compared to an unfilled rubber, the impact of frequency on fluctuations in MRE loss factor is minor due to the fact that embedded fillers impede the rubber molecules during cyclic loading (Li and Gong 2008). At higher frequencies, the loss factor of MRE is minimal, suggesting that the sliding of molecular chains in the rubber matrix dissipates less energy (Yunus et al. 2016). In addition, Chen et al. observed that as frequency increased, the effect of magnetic field on the damping properties of MRE reduced. This occurrence was ascribed to a shortage of time to show the field-induced impact when the driving frequency was increased to greater levels (Chen and Gong 2008).

Similar to ordinary filled elastomers, MRE exhibits displacement-sensitive characteristics (Gong et al. 2005; Li and Sun 2011). There are two sorts of interactions in a filled elastomer: particle-matrix and particle-particle (Yu et al. 2017). The storage and loss modulus of MRE are significantly affected by these interactions. The applied strain alters the processes behind these interactions, which changes the storage and loss moduli. As applied strain increases, the storage modulus of MRE decreases (Agirre-Olabide et al. 2015; Gong et al. 2012a; Koo et al. 2009). Strain-induced differences in MRE characteristics are typically differentiated relative to the critical strain (Agirre-Olabide et al. 2015). Within the critical strain, the relationship between the storage modulus and strain is almost linear. The storage modulus is dramatically lowered beyond the critical strain (Yu et al. 2017). This phenomenon is linked to the degradation of the matrix-filler structure due to external stress. At smaller strain amplitudes, the matrix-filler structure is marginally harmed. But the MRE still maintains its linearity, the storage modulus is significantly diminished (Gong et al. 2012a). Consequently, the linear viscoelastic area of MRE is typically understood as the strain corresponding to a 10% divergence from the strain-independent storage modulus determined by the SAOS test (Agirre-Olabide et al. 2015). At higher strain amplitudes, however, the interface is destroyed, resulting in a greater decrease in storage modulus (Sorokin et al. 2014).

Comparable to a filled elastomer, the damping properties of the MRE are more sensitive to the dynamic strain amplitude (Fan et al. 2011; Sun et al. 2008). In response to differences in strain amplitude, filled elastomer displays an initial rising and falling trend (Poojary et al. 2017). MRE is dampened by the discontinuous phase formed by fillers inserted in an elastomer matrix (Chen and Gong 2008; Fan et al. 2011; Li and Gong 2008). Because the microstructure of MRE is not disrupted at lower strains, damping is reduced. Nevertheless, when the strain grows, the relative motion between the particles intensifies, resulting in an increase in damping (Sorokin et al. 2014). As strain rises, the microstructure of MRE is entirely destroyed. Consequently, the contribution from contact friction is decreased, considerably reducing the loss modulus (Yu et al. 2017). Further, because the loss factor is reliant on the storage modulus and the loss modulus, thus it is also influenced. The loss factor stabilises at greater strain levels after reaching its maximum with rising strain (intermediate strain levels).

The strain has a substantial effect on the magnetic characteristics of MRE because the fillers are moved from their original location (Chen et al. 2007; Zhu et al. 2013). Very few investigations have shown strain-dependent magnetic field characteristics. Nonetheless, these investigations are unclear due to inconsistent findings. Sorokin et al. (Sorokin et al., 2014) revealed that the strain amplitude damaged the magnetic field-formed internal filler structure. This impact is less in the non-magnetized condition due to the absence of the filler structure. However, in the presence of a magnetic field, the disruption of magnetic coupling generated by the input strain displaces particles from their starting locations by breaking through the energy barrier and reshaping them. Chen et al. (Chen et al., 2007) discovered that when the distance between the fillers was lowered, the magneto-induced modulus dropped, resulting in a reduction in the interaction energy between the fillers. Lokandar et al. (Lokander and Stenberg, 2003) observed that, within the studied strain range, the MR effect declined fast with increasing strain. Yu et al. (Yu et al., 2017) determined that the amplitude-dependent behaviour of MRE was comparable to the Payne effect, which is widely seen in filled rubbers. The Payne effect is defined as the difference between the modulus found at lower strain and maximum strain (Yu et al. 2017). In the magnetised condition, the Payne effect is more evident because the modulus corresponding to increased strain is less susceptible to fluctuations in the magnetic field. However, the effects of magnetic field on MRE re-

51

sponse at moderate strain levels (the crucial strain zone) are mostly neglected in the prior research. In the critical strain zone, field-induced interactions between the fillers are crucial because the magnetic force drives iron particles to shift from their starting positions (Gong et al. 2012b). This process may have a substantial effect on strain-dependent MRE responsiveness.

2.8 Viscoelastic modeling of MRE isolator

The ability of a MRE-based device to adjust its properties in response to control signals is critical for its success. This necessitates a mathematical description that represents the field-induced properties of MRE. The properties of MRE are viscoelastic in nature and it cannot be represented mathematically using fluid or solid laws alone. Furthermore, these properties vary with magnetic field, preload, strain amplitude, and excitation frequency which impart hysteresis behaviour of MRE. As a result, it takes a significant amount of effort to represent this behaviour in the form of a mathematical relationship.

Material modelling methodologies for MRE are either parametric or nonparametric in general. A nonparametric technique is used to build models with a high number of parameters. The parameters of the nonparametric model have no clear meaning, but they are highly correlated with the experimental data. Non-parametric modelling (the second branch of macro-modeling) can establish corresponding mapping relationships between inputs (excitation amplitude, frequency of excitation, and input current) and outputs (force response or displacement response) without requiring a complex parameter identification process, and it is robust and applicable to capture nonlinear and hysteresis performances (Fu et al. 2016) (Wang and Liao 2011). The neural network (NN) is a powerful non-parametric method for developing approximate nonlinear mapping relationships that is highly practical due to its high accuracy, low complexity, and ease of identification (Fu et al. 2016). However few studies have reported this approach. Koo (Koo et al. 2010) used a NN to to determine the nonlinear relationship between stress and magnetic flux density, displacement, velocity, and compression force of the MRE element to simulate the stress under cyclic strain. Yu et al (Yu et al. 2015a) used ANN for forecasting the hysteretic responses of MRE base isolator under various loading conditions (displacement, velocity and current). Fu et al (Fu et al. 2016) used NARX neural network with three-layer structure to approximate the functional relationship between

inputs (displacement, velocity and current) and output (force) of magnetorheological elastomer isolator. Leng et al. (Leng et al. 2018) proposed an artificial neutral network approach optimised by fuzzy algorithm (ANNOFA) system that is simpler, faster to convergence, and has reasonable accuracy for capturing the nonlinear functional relationship between MRE isolator inputs (displacement, frequency, and current) and output (force). These models are capable of predicting the MRE behaviour under steady-state force vs displacement responses at different excitation and current amplitudes (Fu et al. 2016; Leng et al. 2018; Yu et al. 2015a). However, these models are not effective in predicting the dynamic response of the MRE isolator over a wide frequency range.

In contrast to nonparametric modelling, parametric modelling is a reliable way of characterising material behaviour as a collection of physical elements such as springs and dampers. The parametric modelling approach uses an integral models or internal variables models to depict viscoelastic behaviour. Integral models are based on the assumption that the stress is an explicit function of strain history. This approach generalizes the Boltzmann principle. Internal variables models assume that stress is affected by state variables, including internal ones. These internal variables are influenced by strain history via evolution laws. This method includes rheological models. The simplest constitutive equations of this type are the Maxwell and Kelvin–Voigt models, which simply connect a spring and a dashpot in series and parallel, respectively. A supplementary branch is required to correctly predict the behavior of a viscoelastic solid, which leads to the Zener and Poynting–Thomson models.

To reduce the number of parameters in the integer order based models, fractional element in the viscoelastic modelling is introduced (Gil-Negrete et al. 2009). Fractional derivative order models are popular because they easily model the dynamic behaviour of a vibration mitigation device (Poojary and Gangadharan 2018). These models anticipate the properties of a material that is halfway between a Hookean solid and a Newtonian fluid (Yang et al. 2013b). A new type of element known as spring-pot is proposed as a generalisation of these qualities in a fractional order model (Torvik and Bagley 1984). The spring-pot is made up of a fractional power "α" with values ranging from 0 to 1. Because polymer damping characteristics do not exhibit a substantial frequency dependence, the appearance of fractional order in a viscoelastic model has a sound physical significance. In comparison to integer order models, fractional order models accurately

anticipate frequency-dependent behaviour. Furthermore, fractional order models could agree on a broad spectrum of viscoelastic behaviour in a basic form with fewer parameters (Gil-Negrete et al. 2009).
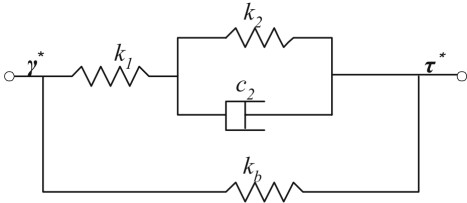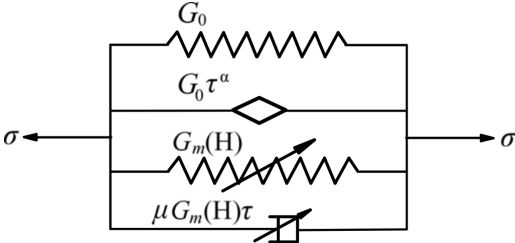
Under cyclic loading, filled elastomer material MRE exhibit hysteresis behaviour. This is due to during the loading-unloading cycle, the stress under unloading is considerably less than the stress under loading at the same strain (Dorfmann and Ogden 2005). The magnitude hysterisis is the region between the loading and unloading stress-strain curves. This hysterical behaviour of MRE is primarily due to the Mullins effect (Coquelle and Bossis 2006). Numerous explanations and phenomenological models have been proposed for the Mullins effect, primarily based on the concepts of slippage and disentanglement of polymer molecules, bond rupture between particle fillers and polymer matrix, and particle aggregation breakdown (Coquelle and Bossis 2006; Perales-Martínez et al. 2017). Hysterisis phenomena in the MRE was experimentally studied by Gundermann et al (Gundermann and Odenbach 2014). He discovered that, when MRE is magnetized and then demagnatized the particles in the matrix expected to reach intial state, which did not happen when he observed in the X-ray micro-computed tomography (XCT).

There are numerous hysterisis models that simulate hysterisis behaviour. The most classical hysterisis model is the Bouc-Wen model, which was first proposed by Bouc-Wen in 1971. To simulate the hysteretic loop, the Bouc-Wen model includes a highly nonlinear differential equation. This phenomenal expression improves model accuracy by introducing an intermediate dynamic parameter. Several phenomenal models have been developed based on this hysteresis model to capture the hysteretic behaviour of various MRE-based devices. In addition to the Bouc-Wen model, two other parametric models were proposed. The improved Dahl model, in which the Dahl hysteretic component rather than the Bouc-Wen component is used to simulate shear force to avoid over-identification of parameters, that can perfectly reproduce the force-displacement responses in the peak displacement regions (Yu 2014). The other model is the LuGre hysteretic component-based dynamic model, which employs the LuGre component to capture shear dynamics (Yu et al. 2015d). The configuration of this model is simpler than that of the Bouc-Wen model. Although Bouc-Wen has more parameters, it still effectively describes the most important phenomenon of MRE-based device behaviour. It

could also perform parameter linearization via appropriate operations, making it suitable for real-time parameter identification.
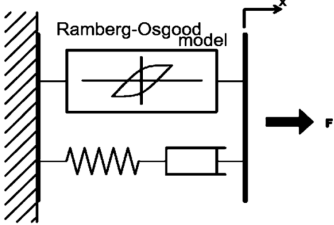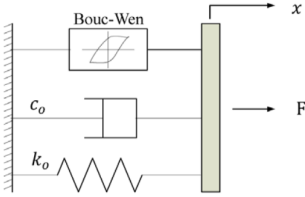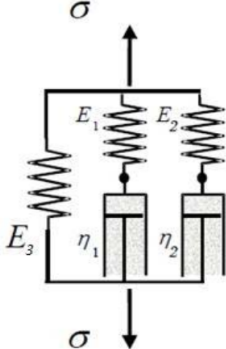
As described in the preceding paragraphs, the behaviour of MRE is estimated using a combination of viscoelatic models (integral or fractional models), and hysteritic models. In addition to those models, the model can include changes in dynamic properties. This can be considered by adding additional springs and dampers to the existing model. Different viscoelastic mathematical models developed by researchers to simulate the behaviur of MRE is listed in Table 2.2. Once the viscoelastic model for the MRE isolator is confirmed, the model parameters are evaluated using optimization techniques to minimise the mean square error between the estimated model force output and the experimentally evaluated force. This optimization is typically performed using a Matlab toolkit with a Gradient Descent algorithm to minimise the cost function (Li et al. 2010). To estimate the parameter values, the other alternative optimization approaches such as particle swarm algorithm (Li and Li 2015) or a genetic algorithm (Yu 2014) or enhanced particle swarm optimization (EPSO)(Yu et al. 2015b), or an artificial fish swarm algorithm (AFSA) (Yu et al. 2015c) or fruit fly optimization algorithm (IFFOA) (Yu et al. 2015d) were also adapted in optimization process to reduce the computation time compared to the Gradient Descent. The parameter identification on the majority of the mathematical models for MRE developed in the literature is typically performed on steady-state force versus displacement responses at different amplitude of excitation and the current, which necessitated a large number of experiments and time consuming process to develop a complete mathematical model for MRE isolators. The models for a wide frequency range under different magnetic conditions, and the amplitude of excitation is yet be developed.

Table 2.2: Various visco-elastic models in the literature

Mathematical Model	Model Details
	Author: (Li et al. 2010) **Viscoelastic model**: Spring in series with Kelvin Voigt **Additional Element**: Extra spring added in parallel with viscoelastic model to detect change in stiffness and damping **Simululated Response**: steady-state stress versus strain responses **Identification of model paramaters** : Gradient Descent algorithm
	Author: (Zhu et al. 2012) **Viscoelastic model**: Fractional kelvin voigt **Additional Element**: Additional spring and damper arranged parallel to Fractional kelvin voight to detect change in stiffness and damping. **Simululated Response**: steady-state stress versus strain responses **Identification of model parameters**: Gradient Descent algorithm

<div align="center">Continued on next page</div>

56

Table 2.2 – continued from previous page

Device	Specification
	Author: (Eem et al. 2012) **Viscoelastic model**: Maxwel Model **Hystirisis model**: Ramberg-Osgood model **Simululated Response**: steady-state force versus displacement responses **Identification of model parameters**: Nelder-Mead optimization algorithm algorithm
	Author: (Yang et al. 2013a) **Viscoelastic model**: Kelvin Voigt model **Hystirisis model**: Bouc-wen **Simululated Response**: steady-state force versus displacement responses **Identification of model parameters**: Gradient Descent algorithm
	Author: (Norouzi et al. 2017) **Viscoelastic model**: Two maxwell elements in parallel with a spring **Simulated Response**: steady-state stress versus strain responses **Identification of model parameters** : Gradient Descent algorithm
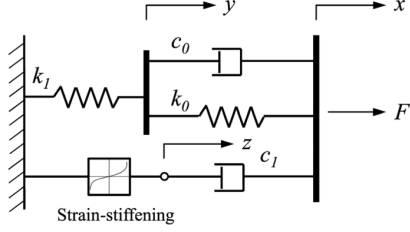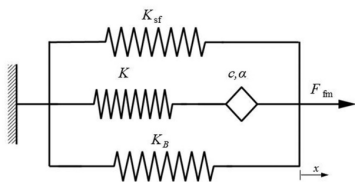
Table 2.2 – continued from previous page

Device	Specification

Author: (Behrooz et al. 2013) **Viscoelastic model**: Spring in series with Kelvin Voigt **Hystirisis model**: Bouc-wen **Additional Element**: Additional spring and damper arranged parallel to kelvin voight to detect change in stiffness and damping. **Simulated Response**: steady-state force vs displacement responses **Identification of model parameters**: Gradient Descent algorithm

Author: (Yu et al. 2016) **Viscoelastic model**: Kelvin Voigt **Hystirisis model**: Strain stiffening component **Simululated Response**: steady-state force vs displacement responses **Identification of model parameters**: particle swarm optimization algorithm

Author: (Yu et al. 2015c) **Viscoelastic model**: Kelvin Voigt **Hystirisis model**: LuGre friction **Simululated Response**: steady-state force vs displacement responses **Identification of model parameters**: fruit fly optimization algorithm

Table 2.2 – continued from previous page

Device	Specification
	Author: (Li and Li 2015) **Viscoelastic model**: Spring in series with Kelvin Voigt **Hystirisis model**: In series with a strain stiffening spring element and a dashpot element Simululated Response: steady-state force vs displacement responses **Identification of model paramaters**: Gradient Descent algorithm
	Author: (Poojary and Gangadharan 2018) **Viscoelastic model**: Fractional Zener **Additional Element**: Extra spring added in parallel with viscoelastic model to detect change in stiffness and damping **Simululated Response**: steady-state force vs displacement responses **Identification of model paramaters**: Gradient Descent algorithm
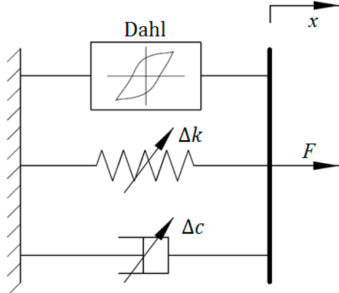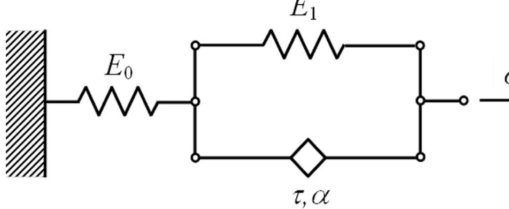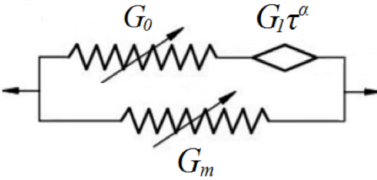
Table 2.2 – continued from previous page

Device	Specification
	Author: (Nguyen et al. 2020) **Viscoelastic model**: Fractional Zener **Additional Element**: A fractional standard solid model in parallel with the magnetic dipole interaction model and smooth Coulomb friction to represent the frequency-dependent nonlinear properties of the MRE isolator **Simululated Response**: steady-state force vs displacement responses **Identification of model paramaters**: Estimated from the steady-state force vs displacement responses plot
	Author: (Yu et al. 2019) **Viscoelastic model**: Kelvin Voigt **Additional Element**: Additional spring and damper arranged parallel to kelvin voight to detect change in stiffness and damping. **Simululated Response**: steady-state force vs displacement responses **Identification of model paramaters**: Gradient Descent algorithm
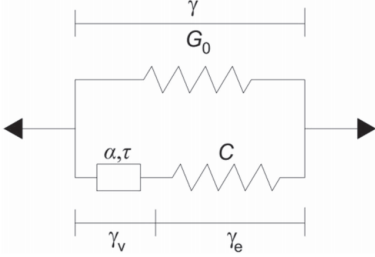
Table 2.2 – continued from previous page

Device	Specification
	Author: (Yu 2014) **MRE model**: Dahl model **Additional Element**: Additional spring and damper arranged parallel to kelvin voight to detect change in stiffness and damping **Simululated Response**: steady-state force vs displacement responses **Identification of model paramaters**: Enhanced Genetic Algorithm algorithm
	Author: (Nam et al. 2021) **Viscoelastic model**: Fractional Zener **Simululated Response**: steady-state stress versus strain responses **Identification of model paramaters**: Gradient Descent algorithm
	Author: (Zhu et al. 2020) **Viscoelastic model**: Fractional Zener **Simululated Response**: steady-state stress versus strain responses **Identification of model paramaters**: Gradient Descent algorithm

Table 2.2 – continued from previous page

Device	Specification
	Author: (Agirre-Olabide et al. 2017) **Viscoelastic model**: Fractional Zener **Simululated Response**: steady-state stress versus strain responses **Identification of model paramaters**: Gradient Descent algorithm

2.9 Semi-active Control Strategies

To optimize the efficacy of an MRE isolator, an effective control strategy is necessary. The controller for the MRE isolator must deliver a control signal to the device to isolate vibrations for the full frequency band, which must be active for a certain frequency range before becoming passive. The designed controller must be robust and adaptive to changing stimulation magnitude and frequency. In the domain of MRE device control development, fairly little research has been undertaken so far.

The controller for MRE isolator can be model-dependent and model-free. The model-free controllers, which are independent of the system model, such as the ON-OFF controller(Xu et al. 2018), PID controller (Zhao et al. 2022), ANN and fuzzy controller (FC) (Fu et al. 2016) are used to mitigate the vibration of MRE isolation system. With the advantages of simple structure and easy implementation, ON-OFF control is used in most MRE isolation control systems. However, it only has two states (the minimum stiffness and the maximum stiffness) of MRE isolators, which cannot make full use of the advantages of continuous stiffness, and also makes the response of the system easier oscillatory.

PID control, the most widely used controller in industries, has the capability to work

in a closed-loop system. As the PID control method, it is effective for certain frequency and amplitude vibrations but has poor robustness on time-varying vibrations (Fu et al. 2018a). To provide robustness and work for other frequencies and amplitude, Zhao et al. (Zhao et al. 2022) developed a PSO-based PID controller for the nonlinear vibration suppression of a square-celled sandwich plate with a multi-zone MRE filler core. By employing PSO, the optimal parameters of the PID controller were determined. The theoretical and experimental validations show that the proposed semi-active controller was effective in vibration suppression and has a significant effect on vibration control. Similarly in another work, an optimal fuzzy fractional-order PID (OFFO-PID) (Guo et al. 2020) method was developed to control the precision platform. The correction values of the five control parameters of the fractional-order PID controller are obtained through calculation by the fuzzy controller, and the five variables of the fractional-order PID are tuned in combination with the particle swarm optimization algorithm. Finally, the fractional-order PID controller outputs the control current to the MRE devices.

In recent years, fuzzy logic (FL) has drawn the interest of academicians and engineers due to its inherent robustness, ability to handle nonlinearities and uncertainties, and avoidance of the need for a precise mathematical model. To overcome the issue of chattering that is present in the on-off controller, a model-free fuzzy controller (Fu et al. 2016) was developed. The developed semi-active fuzzy logic controller (FLC) is independent of a system model and robust given the nonlinearity and excitation uncertainty of the MRE isolator. The FLC with single-frequency and multiple-frequency excitation reduces acceleration transmissibility by 54.04% at most, proving the effectiveness of the designed semi-active FLC. Similar work was also implemented (Leng et al., 2021) to control the non-resonant vibration of the jacket on offshore platforms. Dynamic object structure analysis is used to create the fuzzy core. Numerical results show that MRE isolation with a semi-active fuzzy controller (SFC) reduces deck displacement and acceleration under realistic irregular waves at different sea states. To consider time delay in the MRE isolator, a self-tuning fuzzy controller was developed by Fu et al. (Fu et al. 2020a). The real-time results conclude that the acceleration RMS with TDC has been attenuated more greatly than that without TDC. For controlling vibration for various frequencies and amplitude, a nonlinear self-tuning fuzzy controller (STFC) was developed. The self-tuning is done with nonlinear self-tuning law and is designed by using a ge-

netic algorithm to optimize scaling factors. The results show that the designed nonlinear STFC is more effective for suppressing the time-varying vibration with an amplitude of 0.5–3 m/s^2 and frequency of 45–60 Hz. Based on zero-magnetic transmissibility curves, a semi-active AFC with factor adjustment is developed (Fu et al., 2019). The AFC reduces isolation structure acceleration by 34.65% more than the conventional FC. The AFC can maintain consistent performance in the presence of time-varying excitation parameters (amplitude from 1.0 m/s^2 to 4.0 m/s^2, and frequency from 80 Hz to 110 Hz), while the conventional FC with constant factors only achieves satisfactory control around the initial design condition. To provide stability to the controller, a fuzzy semiactive vibration controller (Nguyen et al. 2017) was developed based on Lyapunov theory implemented on MRE isolator for mitigating vibration. The system is excited with random excitation and the response of the system is controlled by implementing a control algorithm. The results indicated that when compared to on-off controller which creates jerks in the system, the fuzzy controller controls the system without jerks and peaks.

Neural network controller (NN controller) contains set of neuron clouds analogous to human brain nerve cells. Based on the previous trained data, the weight and bias of the neural network selected and decision is taken based on the activation function. The neural network controller is mostly used where the system is nonlinear and it is difficult to represent it in mathematical form. Neural Network based controller are most reliable and efficient than Fuzzy, but have larger processing time. To provide the stability for the NN controller, Liu et al. (Liu et al. 2020) proposed a novel NN control scheme for the MRE-based isolator. The Lyapunov method verifies the convergence and stability of the proposed control strategy. The proposed control strategy is compared to passive skyhook controllers under harmonic motion, road bumps, and random profile excitations. The proposed NN controller reduces driver seat vibration and outperforms passive and skyhook controllers over the relevant frequency range. To reduce the processing time consumed by the neural network and control the nonlinear system, a fuzzy-neural network controller (FNNC) (Fu et al. 2020b) was developed for the MRE isolator to improve vibration attenuation. The control performance of FNNC compared with fuzzy control under sinusoidal excitation. The results show that the FNNC works better than a fuzzy controller due to the fact that a neural network controller can approximate

the nonlinear function relationship among the controlled force, excitation displacement, velocity and controlled current. The adaptive controller typically generates enormous control force, even when the system is asymptotically stable with a small gain. This is because the controller has a singularity. To address this issue, Truong et al. (Truong et al. 2022) proposed a controller with four components: an adaptive linearizing controller, a deputy adaptive neural network controller, an auxiliary part designed for the controller to address the input constraint problem, and a smooth switching algorithm used to exchange the takeover rights of the two controllers. The proposed controller was tested in simulation on a quarter-car suspension using an MRE-based absorber. The results were promising, demonstrating the effectiveness of the controller.

There are model-based controllers such as the Lyapunov-based controller (Behrooz et al. 2012), clipped-optimal controller (Opie and Yim 2011), H-infinity controller (Du et al. 2011), LQR controller (Gu et al. 2017) and sliding mode controller (Nguyen et al. 2018a) are employed to suppress the vibration in different MRE isolation applications. However, these controllers are limited in use since they require an accurate mathematic model of MRE isolator. To avoid the dependence on mathematical models, these controllers combine with neural networks or fuzzy controllers to become model free. Jin et al. (Jin et al. 2022) implemented an LQR controller developed to control the lateral stiffness of a newly designed hybrid MRE isolation system integrated with a ball-screw inerter installed in a scaled three-story building. With the implementation of the LGR controller on the hybrid isolation system, 20% improvement in vibration control performance compared with the pure MRE isolation system. Gu et al. (Gu et al. 2017) implemented LQR controller on the MRE isolator. The mathematical model for LQR is necessary for the implementation of the controller for that optimal general regression neural network (GRNN) inverse model is used. The control performance is compared with bare building, passive-on isolation system and passive-off isolation system. Testing results demonstrate that the developed controller could able to adapt to various earthquakes as well as the capability of suppressing floor acceleration and inter-storey drift simultaneously. Nguyen and Tung (Nguyen and Tung 2021) implemented using the Lyapunov stability theory to maximize vibration energy absorption. The control performance was tested for all frequencies; results show that the developed controller works for all frequencies. Similar works find in Behrooz et al. (Behrooz et

al. 2012) where he used a Lyapunov-based control technique on a Variable Stiffness and Damping Isolator (VSDI) to isolate vibration on a three-story structure. The building structure was given scaled El Centro EW seismic excitation, and the vibration in the third level was regulated using a VSDI device. The results show that Lyapunov control successfully adjusts VSDI stiffness, reducing vibration in the third level. A sub-optimal H∞ controller (Du et al. 2011) was developed for controlling the vibration of the vehicle seat. Bump and random excitation input to the vehicle seat and the control performance for H∞ controller and on-off controller measured. The H∞ controller effectively isolates the vibrations compared with on-off controllers.

2.10   Summary of Literature Survey

Designs of the MRE Isolator: The MRE isolator works on compressive, shear, torsional modes and combined modes. The compressive mode of an MRE isolator is able to function with a greater load-bearing capacity and a higher initial natural frequency. In contrast, the shear and torsional MRE isolator operate at a lower natural frequency and has a lower load-bearing capacity. For maximal field exposure of MRE, the electromagnet magnet design of the isolator is essential. For that, the preferred location of magnetizing MRE generally will be the core section of the electromagnet. The inclusion of permanent magnets in the electromagnet design reduced power consumption.

Designing parameters of MRE isolator: The designing parameters that are critical for the design of MRE isolator are the modulus of MRE, the permeability of MRE and its response time. The mathematical estimation of the shear modulus provides the amount of shift achieved in the isolator. The estimation of modulus is usually done through the dipole model. Dipole models for MR material are based on magnetic dipole theories, and the overall effect is the inter-particle dipole interactions averaged over the entire sample.

To design a magnetic circuit for an MRE isolator, it is important to know the relative permeability of the MRE. The relative permeability value of MRE mainly depends on the particle volume fraction and its orientation in the matrix. Increasing the particle volume fraction increases the permeability of the MRE. The mathematical equation for estimating the relative permeability of the MRE was provided by Maxwell Garnet.

When employing a smart device based on MRE, the response time of the magne-

torheological elastomer (MRE) material is the most important factor that influences the control performance of the vibration system. Response time is mainly depending on the strain and inductance of the coil. The faster response time can be achieved by field quenching and adding conductive multi-wall carbon nanotubes (MWCNTs).

Material overview of MRE: The MRE isolator active element is made of ferromagnetic material that is filled in an elastomer. Matrix material which is softer produces a better MR effect than hard elastomer. This is due to the ease of movement of a particle in the softer matrix and the lower initial modulus. The filler particle, which is carbonyl iron powder (CIPs), is the most utilized magnetizable particle. CIPs are considered the ideal choice for producing MREs due to their high magnetic saturation, low magnetic residual, softness, and high magnetic permeability. Plasticizers and other types of additives are added to the MRE to reduce the initial stiffness and increase the range of change in stiffness.

Synthesis of MRE Element: Isotropic and anisotropic MRE are the two types of MRE generally made for the active element in the isolator. The manufacturing procedure for isotropic MRE and anisotropic MRE is usually different. The manufacturing of isotropic MRE is generally done in without a magnetic field. In contrast, anisotropic MRE is manufactured under a magnetic field.

Performance assessment of the MRE isolator: For effective use of MRE isolator in a specific vibration isolation application, its stiffness and damping properties have to be experimentally characterized as a function of the magnetic field, the amplitude of excitation and frequency. The standard procedure for testing the isolator is provided in ISO 10846-1. The other alternative for testing the isolator is impact hammer, force/displacement transmissibility and free vibration.

Factors contributing to the performance of MRE isolator: The performance of an MRE isolator is influenced by the magnetic field, temperature, precompression, excitation amplitude, and frequency. Increasing the magnetic field on the MRE increases the amount of isolation in the receiving member at the natural frequency. Increasing temperature beyond transition temperature will reduce the modulus of the MRE. The pre-compressed state of MRE in the isolator has less MR effect due to its high initial modulus. MRE particulate composite, increasing amplitude of excitation reduces the MR effect. This is due to Payne Effect that exists in the MRE. The damping present in

MRE isolator is mainly because of the friction between the filler particle and matrix.

Viscoelastic Modelling of the MRE isolator: MRE mathematical models can be parametric or nonparametric in nature. Viscoelastic Modelling is parametric that provides physical meaning to the system. The behavior of MRE is estimated using a combination of viscoelastic models (integral or fractional models), and hysteretic models. In addition to those models, the model can include changes in dynamic properties. This can be considered by adding additional springs and dampers to the existing model. The model parameters are evaluated using optimization techniques to minimize the mean square error between the estimated model force output and the experimentally evaluated force.

Semi-active Control Strategies: The controller developed for MRE isolator can be model-based and model-free. On-off and fuzzy controllers are model-free, which produces the control output-based condition provided and the rules. Error-based controllers necessitate an exact mathematical model of the MRE isolator; without it, developing controllers for a wider range of frequency vibration may not be possible.

2.11   Research gap and the Scope of the Present Work

To improve the performance of the controller strategy for the designed MRE isolator, a viscoelastic model is necessary. However, there is currently no fully-fledged mathematical model for MRE isolators available in the literature that can provide a comprehensive viscoelastic property based on the current input and the amplitude of excitation in the frequency domain. Developing such a model is challenging and requires a large number of experiments to be carried out while considering all parameter changes.

Following the development of the mathematical model for the MRE isolator, it is necessary to create a controller for the MRE isolator that can generate the control input to the MRE isolator and achieve the desired response. The majority of the controllers developed in the literature survey were only tested in a limited range of frequency and amplitude of excitation, and the controller switching off method when the system runs in the isolation region was not investigated.

To address the research gap in the development of a comprehensive viscoelastic model for magnetorheological elastomer (MRE) isolators and to improve the performance of controller strategies for vibration control, the current research work focused

on the following specific objectives:

- Design an MRE isolator and evaluate its performance in terms of displacement transmissibility under varying current input and excitation amplitudes in the frequency domain.

- Develop a viscoelastic model for MRE isolators to predict their response in the frequency domain, while considering the effect of current input.

- Establish the relationship between the current input and the viscoelastic parameters of the MRE isolator, as well as the amplitude of excitation, to accurately predict the system response in the frequency domain.

- Develop both model-based and model-free controllers for vibration control using MRE isolators that are adaptable to changes in operational conditions and able to automatically shut down in an isolation area.

Chapter 3

DESIGN AND FABRICATION OF MRE ISOLATOR

Summary

In this chapter, MRE isolator is designed to isolate vibrations about 50 to 70% vibrations that are transmitted to the PCB. MRE isolator operates in shear mode, which gives a higher improvement owing to lower starting stiffness values. Isotropic MRE is manufactured with weight ratio of 72% carbonyl iron, 16% silicone rubber, and 12% silicone oil. For magnetising MRE, electromagnet is designed to magnatize MRE about 0.3 Tesla. Using ANSYS Maxwell software, the efficacy of field generation in the electromagnet is assessed, and validated using magnetic circuit analysis.

3.1 Introduction

Modern aeronautical, maritime, and vehicular applications rely heavily on electronic equipment for control, navigation, reconnaissance, and communication. The advanced and extremely dependable electronic packages must be able to run for over 20 years and withstand severe environmental vibration.

A typical circuit design implemented on a printed circuit board contains parts such as transistors, resistors, capacitors and integrated circuits. PCBs which are mounted inside relatively rigid and heavy electronic boxes are the most susceptible to severe environmental disturbances. If these disturbances are not controlled, the PCB output may change or it breaks due to excessive vibration. To avoid these vibrations, an effective isolator needs to be designed.

71

3.2 The design of MRE isolator

PCBs generally have a mass of a few grams. For such systems, the natural frequency is higher. For those system, damage due to low frequency range of vibrations is very high. To protect the circuit board from low frequency vibration, MRE isolator is designed.

Printed circuit board which are made of Epoxy fiberglass having length (l), width (w), and thickness (h), Supported on all four edges, can be mathematically analyzed to determine its natural resonance frequency of vibration, f_n, from the following equations(US patent 6233816B1):

$$f_{n1} = \frac{\pi}{2} \sqrt{\frac{k_{PCB}}{\delta} \left(\left(\frac{1}{l}\right)^2 + \left(\frac{1}{w}\right)^2 \right)} \qquad (3.1)$$

where, k_{PCB} is stiffness of the PCB and $\delta = \frac{mass}{area} = \frac{W}{g(l.w)}$

$$k_{PCB} = \frac{(E.h^3)}{12(1 - \mu^2)} \qquad (3.2)$$

With inclusion of MRE isolator, the natural frequency of the modified system is

$$f_{n2} = \frac{1}{2\pi} \sqrt{\frac{K_{MRE}}{m_{PCB}}} \qquad (3.3)$$

where, K_{MRE} stiffness of MRE and m_{PCB} mass of the MRE.

Then, the stiffness of the MRE, which is derived from natural frequency f_{n2} is

$$K_{MRE} = \left(\frac{f_n}{2\pi}\right)^2 m \qquad (3.4)$$

But, stiffness of the MRE is the related to shear area A and the modulus of the MRE G_P. The relation equation is gives as

$$K_{MRE} = \frac{AG_P}{t} \qquad (3.5)$$

where, t is the thickness of the MRE.

During the design phase, the active element of the MRE isolator operates in shear mode, and the MRE is shaped like a ring. The ring-shaped MRE is suggested because it has the benefit of preventing shaft movement by gripping all sides. In this work, two ring-shaped MREs are considered for use in order to increase the loading capacity of the

device. Now, the area where the shear load acts on the MRE ring has been determined.

$$A = 2\pi D L \qquad (3.6)$$

where, D is the inner ring diameter, and L is the depth of the ring. MRE is considered a particulate matrix. Then, the mathematical expression for the shear modulus of the particulate matrix is (Mital et al. 2020)

$$G_{PC} = \frac{\varphi^{0.67} G_m}{1 - \varphi^{0.67}\left(1 - \frac{G_m}{G_p}\right)} + \left(1 - \varphi^{0.67} G_m\right) \qquad (3.7)$$

where, G_m and G_p are shear moduli of the matrix and filler, and φ are the volume fractions of the particles.

Due to the magnetic field, there is a change in the shear modulus of MRE. The change in shear modulus is (Shen et al. 2004)

$$\delta G = \left(36\varphi\mu_m\mu_0\beta^2 (H_0)^2 \left(\frac{R}{d}\right)^3 \xi\right) \qquad (3.8)$$

where, μ_m and μ_0 are the permeability of matrix and vacuum, R is the radius of the particle, d is the distance between the particles and H_0 is external field strength.

The equation for estimation of permeability of MRE using the Maxwell Garnett mixing rule (Kärkkäinen 2000) is

$$\mu_{eff} = \mu_m + 2\varphi\mu_m \frac{\mu_p - \mu_m}{\mu_p + \mu_m - \varphi(\mu_p - \mu_m)} \qquad (3.9)$$

where, μ_m and μ_p are permeability of the matrix and particle. φ is the volume fraction of the particle.

The stiffness of the MRE, with the application of a magnetic field, is equivalent to

$$k_{MRE} + \delta k_{MRE} = \frac{A(G_{PC} + \delta G)}{t} \qquad (3.10)$$

The natural frequency of the isolator, with the application of a magnetic field, is equivalent to

$$f_n = 2\pi\sqrt{\frac{k_{MRE} + \delta k_{MRE}}{m}} \qquad (3.11)$$

Figure 3.1: MRE isolator components

3.3 MRE synthesis and design components

The field-induced enhancements are critical for MRE isolators to achieve isolation over a wide frequency range. Past studies have revealed that silicone rubber as a matrix for MRE isolator could achieve a high relative MR effect (Khairi et al. 2019). For the proposed design, a two-ring shaped MRE resilient elements are prepared (inner diameter 40 mm, outer diameter 50 mm and thickness 5 mm). The Sample images and other isolator components images are shown in Figure 3.1. The MRE is synthesized with the silicone matrix and CIP fillers. The silicone matrix is procured from Aditya Silicone Rubber (MurtiSil, Rtv 1010) and the CIP fillers are of type CC (manufacturer: BASF, size distribution: 3-5 µm). As reported by the past studies, an optimum content of 72% by a weight ratio of CIP is chosen for the synthesis process (Khairi et al. 2019). Additionally, Silicone oil is added as an additive for the ease of the synthesis process. These materials are mixed thoroughly with a weight ratio of 72% carbonyl iron, 16% silicone rubber, and 12% silicone oil, and the mixture is poured into the mould. The mould was kept in the vacuum chamber for about 20 min to remove the mixer trapped air bubbles. After the vacuuming process, the MRE samples are cured for about 24 hours at room temperature under constant pressure.

The proposed MRE isolator operates in shear mode, as it offers a larger enhancement due to lower values of initial stiffness. A schematic representation of the MRE isolator is presented in the Figure 3.2 and the individual components images are shown in Figure 3.1. The details about the list of components, weight of each component, and their permeability are listed in Table 3.1. The isolator comprises of main isolator body and the casing. The isolator body has the stationary electromagnet, a movable central core,
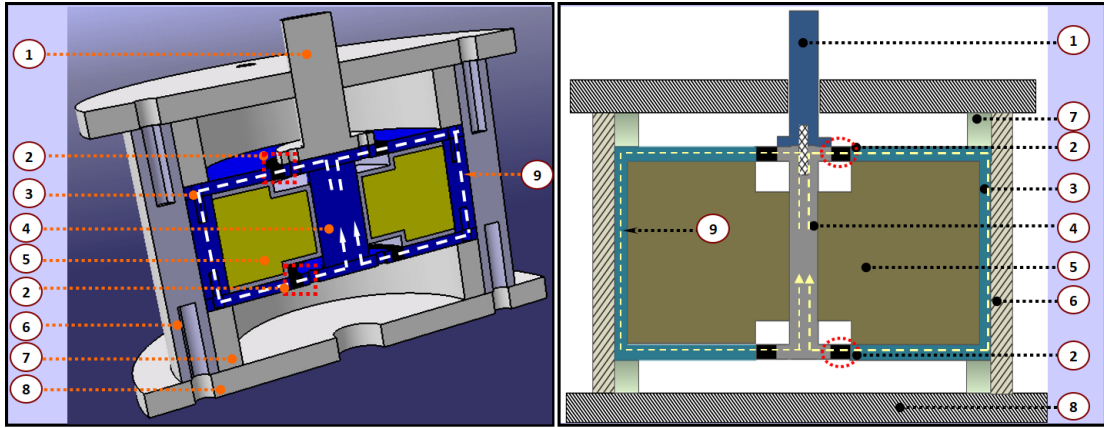
1. Aluminium shaft 2. MRE 3. Steel plate core 4. Moving Steel core 5. Coil 6. Cylindrical Aluminium case 7. Aluminium support rings 8. Aluminium base plate 9. Cylindrical steel core

Figure 3.2: Schematic representation of MRE isolator

Table 3.1: Mass and permeability of the different Parts of the MRE isolator.

S.no	Parts in MRE isolator	mass (kg)	Permeability
1.	MRE	0.008	1.7
2.	Stationary steel plate core	1.77	100
3.	Moving cylindrical steel core	0.098	100
4.	Electromagnetic coil	1.196	1
5.	Aluminium piston	0.0425	1
6.	Aluminium casing	3.154	1
7.	Support rings	0.410	1
8.	Top and bottom mounting base plate	1.314	1

two ring-shaped MRE elements and an aluminium piston attached to the movable central core. The electromagnet consists of a copper coil (20 AWG gauge wire with 980 number turns (Resistance is 6.02 Ω and inductance is 51.7 mH)) wound around the bobbin (inner diameter 20 mm, Outer diameter 100 mm and height 40 mm) (Guðmundsson 2011). The core material (fixed and moving steel core) is manufactured from low-carbon steel. For the proposed design, two ring-shaped MRE resilient elements are attached between the fixed and the moving core at the top and bottom of the isolator. A non-magnetic piston is attached to the moving steel core to accommodate the motion transmission from the shaker to the receiving end. To accommodate the vertical motion of the moving cylindrical core a gap of 10 mm is maintained between the MRE resilient element and the coil. A stationary steel plate core and the central moving cylindrical steel core are

employed to concentrate the flux lines through the MRE. The electromagnetic coil is designed such that the flux lines that pass through the core are perpendicular to the loading direction of MRE resilient element.

The casing of the isolator is a cylindrical aluminium housing of dimension (inner diameter 120 mm and outer diameter 150 mm and height 170 mm). Two aluminium support rings (inner diameter 100 mm and outer diameter 120 mm and height 25 mm) are provided at the top and bottom to facilitate the movement of the central core. Two mounting plates one at the bottom and other at the top (plate diameter 180 mm and thickness of 10 mm) are provided to firmly position the MRE isolator body in the casing. The isolator assembly is rigidly fixed to the electrodynamic shaker using the bottom mounting plate.

3.4   Magnetic Field analysis of MRE isolator

Under the shear mode of operation, the magnetic flux lines perpendicular to the applied load. In order to consider that, an electromagnetic coil designed such that the coil field energizes the MRE, and the flux line that passes through the MRE is perpendicular to a shear load. The performance of the coil is analyzed using Ansys Maxwell 15 software.

(a)   (b)
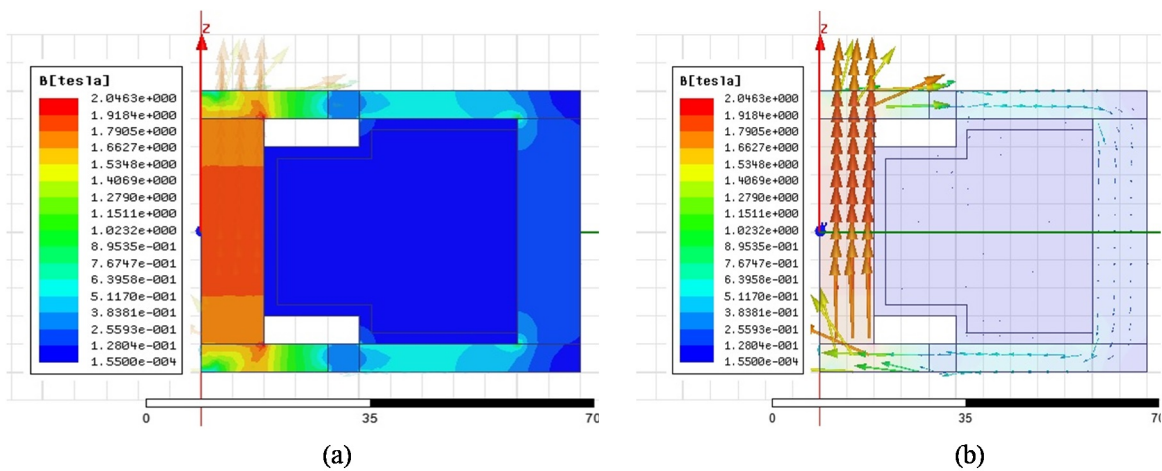
Figure 3.3: Magnetic (a) field strength (b) flux lines generation in electromagnet (Ansys Maxwell 15)

Designed of electromagnet for MRE isolator aimed for generating maximum about 0.3 T(As per Literature survey minimum magnetic field required to achieve maximum MR effect in 0.3 T) in the MRE. The number turns in the coils considered as 981. Based

on the observations depicted in Figure 3.3, it is apparent that the magnetic flux lines traverse the MRE resilient element, indicating that it is well-suited for the proposed design of the electromagnet. The simulated results suggest that a maximum magnetic flux density of approximately 0.37 T can be achieved through the MRE resilient element with an input current of 3 A. Furthermore, the magnetic flux density values for input currents of 1 A and 2 A were found to be 0.123 T and 0.246 T, respectively. These simulated results were subsequently verified with a Gauss meter, which confirmed that the designed electromagnet performed in a manner consistent with the simulated conditions.

3.5 Validation of Magnetic flux generation through magnetic circuit analysis

The magnetic flux density is sensitive to the cross-sectional geometry of electromagnet. Here, the magnetic flux is not uniformly distributed over the cross section of the electromagnet. Sometimes, accurately measuring the magnetic flux density with a Tesla meter, is difficult. In order to identify the equivalent magnetic flux density at the MRE element, the magnetic circuit analysis was done on the electromagnet.
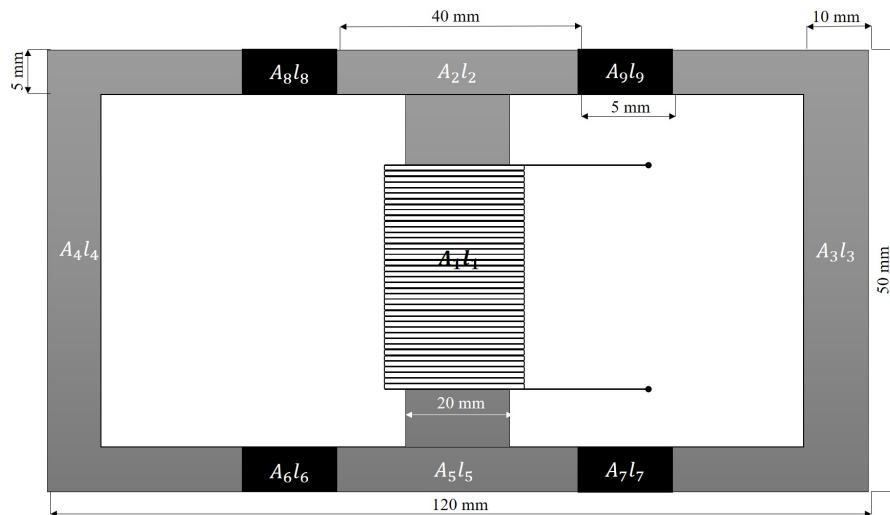
Figure 3.4: Magnetic circuit analysis of the MRE isolator

In the equivalent magnetic circuit of the electromagnet, various area sections of the electromagnet (Figure 3.4), the reluctance at every magnetic conductor is connected series. So, the equivalent reluctance can be presented as

$$R_e = \frac{2l_9}{\mu_m A_9} + \frac{l_1}{\mu_c A_1} + \frac{l_2}{\mu_c A_2} + \frac{l_3}{\mu_c A_3} + \frac{l_4}{\mu_c A_4} + \frac{l_5}{\mu_c A_5} \qquad (3.12)$$

where, l_i (i = 1 to 9) the path lengths of MRE the electromagnet and the MRE, respectively, μ_m and μ_c are the permeability of the MRE and conducting path material of the electromagnet, A_i (i = 1 to 9) are the cross-sectional areas of the MRE and the electromagnet. The magnetic flux density Φ due induced current can be derived as follows:

$$\Phi = \frac{f}{R_e} \qquad (3.13)$$

where, f is the magnetic motive force. Then, the magnetic flux density B is given by

$$B = \frac{\Phi}{A_m} = \frac{f}{A_m R_e} = \frac{NI}{A_g R_e} \qquad (3.14)$$

where, N is the number of coils turns, I is the induced current. The intensity of the magnetic field (H) can be determined from the magnetic flux density divided by μ_0:

$$H = \frac{B}{\mu_0} \qquad (3.15)$$

Because of the induced current, the equivalent magnetic flux and intensity of the electromagnet increased linearly. For 981 number of in the coil and the current 3 A, the electromagnet generated a maximum magnetic flux density of 0.37 T at MRE, which is same as in electromagnet analysis in ANSYS MAXWEL.

3.6   Chapter conclusions

A shear mode MRE isolator for PCBs with a very low natural frequency that will isolate about 50 to 70% of vibrations was successfully developed. A softer isotropic MRE with a weight ratio of 72% carbonyl iron, 16% silicone rubber, and 12% silicone oil was manufactured. Designed an electromagnet for the MRE isolator that generate 0.3 T magnetic field, which was analysed using Ansys Maxwell and validated with magnetic circuit analysis.

Chapter 4

PERFORMANCE ASSESSMENT OF THE MRE ISOLATOR

Summary

In this chapter, performance of the MRE isolator is evaluated experimentally. A collection of tests are designed to assess the performance using the displacement transmissibility test. On the basis of the amount of current applied to the isolator and the variation in excitation amplitude, the performance parameters are analysed during the tests. The results indicate that the performance of an isolator can be altered by varying the magnetic field, excitation amplitude, and excitation frequency.

4.1 Introduction

MRE isolation characteristics can be evaluated experimentally using dynamic mechanical analysis (DMA), rheometers, or force vibration tests. The ISO: 10846-1:2008 and ISO: 10846-2:2008 testing standards serve as the foundation for force vibration tests on MRE, which focus on characterizing the frequency-dependent dynamic stiffness and loss factor. The force vibration tests can be extended to directly measure isolation characteristics such as force or displacement transmissibility. The displacement transmissibility is the ratio of the displacement/velocity/acceleration at the output side to the displacement/velocity/acceleration at the input side. When the device must be protected from vibrations caused by the point of attachment, displacement transmissibility is preferred. The force transmissibility (FT) is defined as the ratio of force at the output side to force at the input side (Hegde et al. 2015), and it is taken into account when the source of vibration is to be isolated from the system of concern. The response function in both

79

approaches are the same, but the system of reference differs.

It is critical to have a thorough understanding of the influence of dynamic deformation in order to use the novel field-induced characteristics of MRE to achieve wide frequency range vibration isolation. The purpose of this study is to evaluate the variation in isolation characteristics of MRE under different deformation levels and magnetic fields using a series of displacement transmissibility tests. The isolation characteristics are investigated using displacement transmissibility measurements on the designed isolator with excitation frequencies ranging from 15 Hz to 80 Hz, magnetic fields ranging from 0 A to 3 A, and amplitude excitation ranging from 1.25 mm to 2.25 mm.
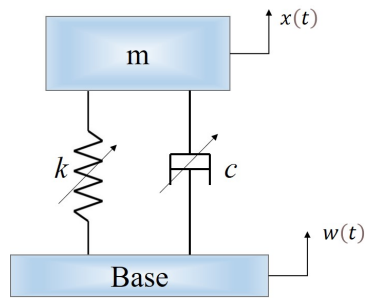
Figure 4.1: Kelvin Voigt SDOF transmissibility model

4.2   Theoretical background

The isolation characteristics of MRE are assessed from the displacement measurement. A simple single degree of freedom (SDOF) of the base excitation system comprising mass m and an isolator is shown in Figure 4.1. MRE is represented by an equivalent Kelvin–Voigt spring of stiffness k and the damping capacity c. The displacement excitation input $x(t)$ given at the base and response of the system at mass $w(t)$ is shown in Figure 4.1.

The movement of differential equation of the SDOF is given by

$$m\ddot{x}(t) + k\left(x(t) - w(t)\right) + c\left(\dot{x}(t) - \dot{w}(t)\right) = 0 \tag{4.1}$$

When the system is subjected to harmonic excitation $w(t) = We^{i\omega t}$ then response of the system is given by

$$x(t) = Xe^{j\omega t} \tag{4.2}$$

80

where, X is amplitude of the response and W is amplitude of excitation. The system equation in frequency domain represented as

$$\left(-m\omega^2 + ic\left(\omega\right)\omega + k\left(\omega\right)\right)X = \left(ic\left(\omega\right)\omega + k\left(\omega\right)\right)W \tag{4.3}$$

where, $k\left(\omega\right)$ and $c\left(\omega\right)$ are the frequency-dependent stiffness and damping capacity, respectively. The ratio of response amplitude to excitation amplitude is given by

$$\frac{X}{W} = \frac{k\left(\omega\right) + ic\left(\omega\right)\omega}{-m\omega^2 + ic\left(\omega\right)\omega + k\left(\omega\right)} \tag{4.4}$$

The complex transmissibility of the system, $H^*\left(\omega\right)$, which represents the amplification of vibrations is expressed in the complex form as (Ramorino et al., 2003)

$$H^*\left(\omega\right) = \left(H' + iH''\right) = \frac{X}{W} \tag{4.5}$$

The modulus of the complex transmissibility or displacement transmissibility (DT) of the system is represented as

$$DT = |H^*\left(\omega\right)| = \sqrt{\left(H'\right)^2 + \left(H''\right)^2} = \sqrt{\frac{\left(c(\omega)\omega\right)^2 + \left(k(\omega)\right)^2}{\left(k\left(\omega\right) - m\omega^2\right)^2 + \left(c(\omega)\omega\right)^2}} \tag{4.6}$$

Equation 4.6 represents the frequency dependency of DT. Apart from frequency, the DT of MRE is also influenced by the input strain and the magnetic field. These variations are assessed from the ratio of response amplitude and excitation amplitude at different magnetic field and strain as represented in Equation 4.6.
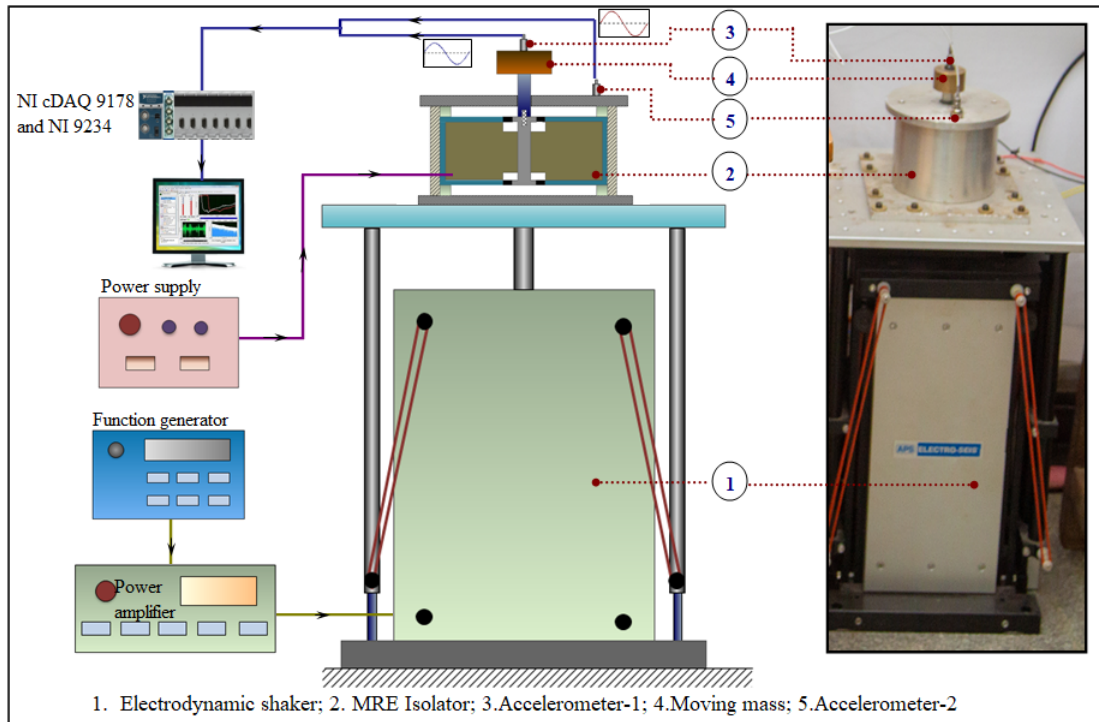
Figure 4.2: Schematic representation of the test setup for measuring the displacement transmissibility response of the isolator

4.3 Experimental setup for transmissibility test

A displacement transmissibility test was used to determine the isolation performance of the MRE isolator. To determine the effect of vibration isolation in frequency domain at various excitation amplitudes and input currents various tests were conducted. The experimental setup is depicted schematically in Figure 4.2. The MRE isolator was attached to an inertial mass of 0.583 g, and the isolator was mounted on the electrodynamic shaker (APS 420 ELECTRO-SEIS). Two accelerometers (KISTLER type 8774A50) were used to measure the input and output accelerations; one was placed on the base plate and the other on top of the inertial mass. The MRE isolator was connected to a programmable power source, which supplies an input current up to 3 A to the coil. The initial testing of the MRE isolator in passive mode revealed that the natural frequency was around 30 Hz, and the corresponding value at 3 A input current is 50 Hz. Consequently, to assess the performance of the MRE isolator, a region close to the resonance region is considered. Thus, performance assessment of the MRE isolator is focused on the frequency region of 15 Hz to 80 Hz. To study the amplitude ascendancy on the performance of the MRE

isolator, the tests were conducted at different amplitude of excitation between 1.25 mm to 2.25 mm. To have an accurate control over amplitude dependency, initial tests were conducted to calibrate the voltage output of the function generator in terms of amplitude of excitation, where 2 V represents 1.25 mm amplitude excitation, and 4 V represents 2.25 mm amplitude excitation. A sine sweep frequency of 15 Hz to 80 Hz was generated with duration 8 s from the function generator to shaker, and the disturbances were transferred to the inertial mass via the MRE isolator. For each test, the current to the coil varied from 0 to 3 A with a 0.5 A step increment. The accelerometer sensor responses at the base and inertial mass were collected (2.5K samples in 8 s) using a data acquisition device (NI 9234) and analyzed with LabVIEW software.
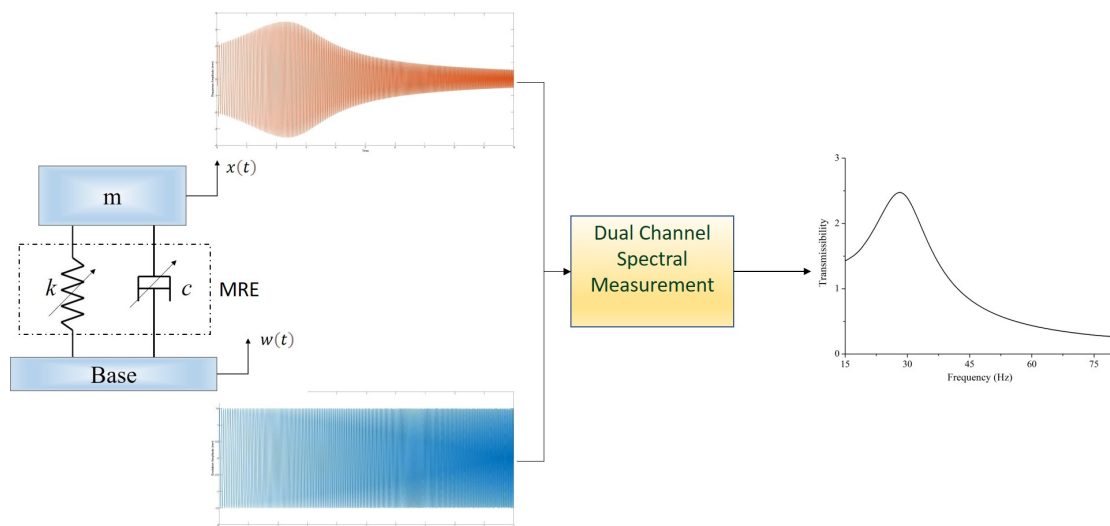
Figure 4.3: Process of estimating transmissibility

4.4   Results and discussion

With tested results, the collected sensor data from different tests were analysed in the displacement transmissibility plots. The process of estimating the displacement transmissibility is shown in Figure 4.3. The influence of magnetic field and excitation amplitude on the trasmissbility of the MRE isolator are analysed separately in following subsection.
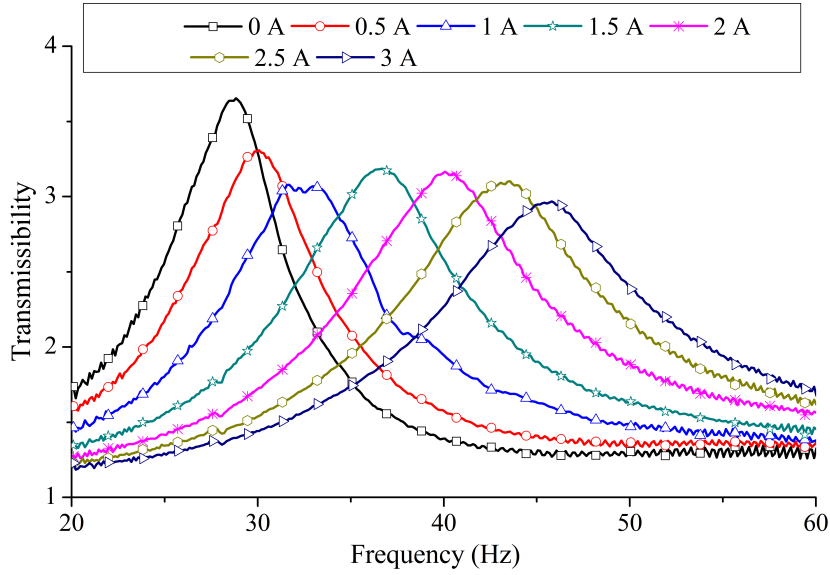
Figure 4.4: Displacement transmissibility of MRE isolator at different current input

4.4.1 Magnetic field dependency of transmissibility

Figure 4.4 depicts the displacement transmissibility responses of the MRE isolator at different input currents under 1.5 mm amplitude of excitation. As evident from the graph, the natural frequency of the system increases with an increase in input current. At 0 A input current, the natural frequency of the system is 28 Hz, and it increased to 47.2 Hz for the input current of 3 A with a frequency shift of 19.2 Hz. The amount of shift in the natural frequency at different input currents is listed in Table 2. Among the tested conditions, the frequency shift is lower for the input current is 0.5 A, and it is maximum for 3 A current input. The shift in natural frequency of the system with the input current is associated with the enhancement in the stiffness under the influence of magnetic field. Additionally, the damping characteristics of the system also vary in response to the magnetic field. Using following relations, the stiffness, and damping characteristics of MRE resilient element are extracted from the transmissibility plots. The effective stiffness k_{eff} of the isolator expressed as

$$k_{eff} = m \, (2\pi f_n)^2 \qquad (4.7)$$

84

where, m is inertial mass and f_n are the natural frequency of the isolator. The transmissibility T_r of the isolator is

$$T_r = \sqrt{\frac{1 + \left(2\frac{\omega}{\omega_n}\xi\right)^2}{\left(1 - \frac{\omega}{\omega_n}\right)^2 + \left(2\frac{\omega}{\omega_n}\xi\right)^2}} \qquad (4.8)$$

where, ω excitation frequency in rad/s and ω_n natural frequency in rad/s At natural frequency, where $\frac{\omega}{\omega_n} = 1$, then the damping ratio ξ of the isolator expressed as

$$\xi = \sqrt{\frac{1}{4(T_{rn}{}^2 - 1)}} = \frac{c}{2\sqrt{km}} \qquad (4.9)$$

where, T_{rn} represents transmissibility at the natural frequency and c is the damping coefficient. The stiffness and the damping ratio values listed in Table 4.1 confirms that with the increase in input current the stiffness and the damping increases. At 3 A input current, the enhancement in the stiffness is 184.76%. Compared to stiffness variation, the enhancement in the damping is not significant. A maximum enhancement of 19.96% in damping is noticed as the input current is increased to 3 A.

Table 4.1: Stiffness and damping ratio of the MRE under various current Inputs

Current (A)	Natural frequency (Hz)	Frequency shift (Hz)	Stiffness (KN/m)	Damping ratio	Relative increase in Stiffness	Relative increase in Damping
0	28	-	17.97	0.1506	-	-
0.5	29.87	1.87	20.46	0.1633	13.84%	8.43%
1	33	5	24.97	0.1743	38.90%	15.76%
1.5	37.12	9.12	31.60	0.1673	76.79%	11.11%
2	41.5	13.5	39.49	0.1679	119.67%	11.50%
2.5	44.62	16.62	45.66	0.1699	154%	12.87%
3	47.2	19.2	51.20	0.1806	184.76%	19.96%
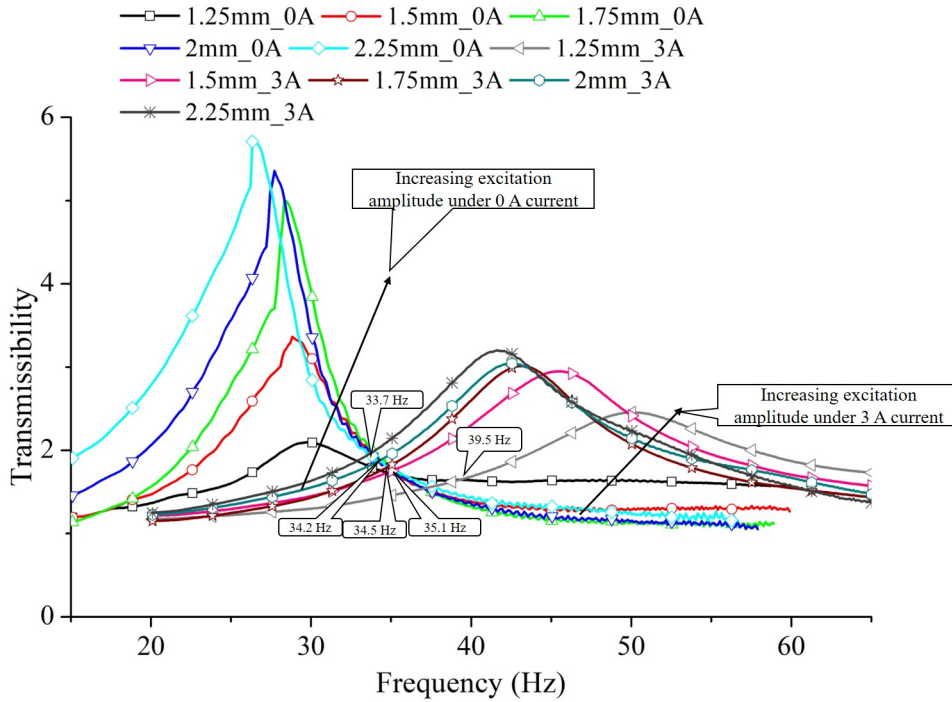
Figure 4.5: Transmissibility of MRE isolator with different excitation input without magnetic field 0 A and with magnetic field 3 A

4.4.2 Amplitude dependency of transmissibility

The property of MRE isolator is sensitive to the input amplitude of excitation. This typical behaviour is associated with Payne effect (Sorokin et al. 2014a) exhibited by MRE under the dynamic loading, which is characterized by the decrease in stiffness with an increase in input strain under dynamic loading. Figure 4.5 shows a comparison between the displacement transmissibility response of MRE isolator registered at different amplitude of excitation corresponding to 0 A and 3 A input current. As evident from the graph, the natural frequency decreases with an increase in the amplitude of excitation. This response is consistent under both passive (0 A) and active (3 A) state. From the response plots, natural frequency, frequency shift, stiffness and damping values are extracted at different amplitude of excitation and input current and the corresponding values are listed in Table 4.2.

As shown in Table 4.2, the natural frequency of the isolator system decreases with an increase in amplitude of excitation. Under passive state, for an input amplitude of 1.25 mm, the natural frequency of the system is 31 Hz, and with increasing the input current to 3 A, the natural frequency is increased to 52.70 Hz, with a total frequency shift of 21.07 Hz. For the amplitude of excitation of 2.25 mm, the natural frequency of
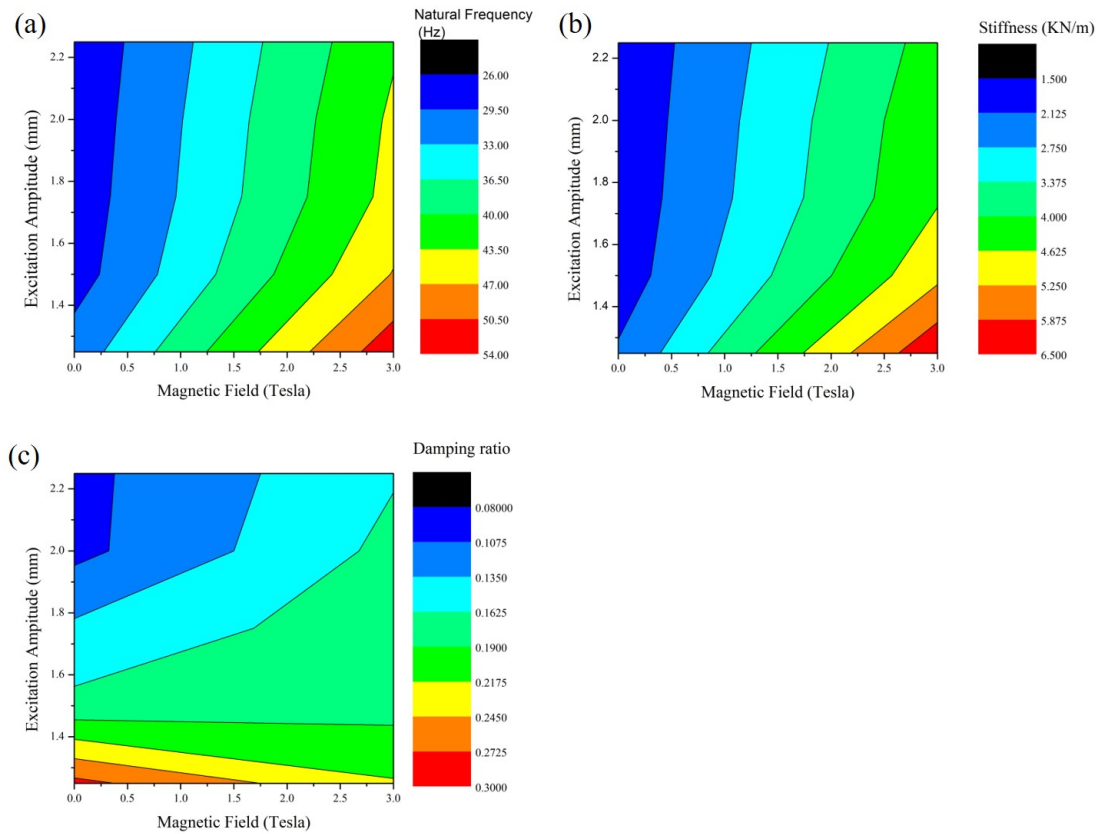
Figure 4.6: Variation of (a) natural frequency, (b) stiffness, (c) damping ratio with respect to applied magnetic field and excitation amplitude

Table 4.2: Properties of MRE isolator under different amplitude of the excitation

Excitation Amplitude (mm)	Without magnetic field (0 A)			With magnetic field (3 A)			Overall Change		
	Natural frequency (Hz)	Stiffness (KN/m)	Damping ratio	Natural frequency (Hz)	Stiffness (KN/m)	Damping ratio	Frequency Shift (Hz)	Relative increase in Stiffness	Relative increase in Damping
1.25	31	22.03	0.28	52.70	63.93	0.22	21.07	190.09%	-22.91%
1.50	28	17.98	0.17	47.19	51.09	0.18	19.18	184.16%	3.0%
1.75	27.6	17.47	0.14	44.59	45.61	0.18	17	161.09%	28.3%
2	27.3	17.09	0.10	44.09	44.60	0.17	16.79	160.01%	62.3%
2.25	27	16.72	0.01	43.09	42.60	0.16	16.09	154.78%	67%

the system registered at 0 A is 27 Hz, and it increases to 43.09 Hz for an input current of 3 A. It is also observed that, the frequency shift is a function of input amplitude. At larger excitation amplitude, the frequency shift with respect to the active state of MRE decreases.

With an increase in amplitude of excitation, the stiffness and the damping ratio of the isolator system is decreased. Among the tested input excitation amplitude levels,

the stiffness and the damping ratio values are maximum for an input amplitude of 1.25 m. At 0 A input current, the stiffness of the isolator is reduced from 22.03 KN/m to 16.72 KN/m for varying the amplitude of excitation from 1.25 mm to 2.25 mm. Corresponding values for the input current of 3 A current decreases from 63.93 KN/m to 42.60 KN/m. This implies that the stiffness reduction with increasing strain is more pronounced in the presence of a magnetic field (Sorokin et al. 2014b). With increased excitation amplitude, the overall relative change in relative stiffness of the MRE isolator decreases from 190.08% to 154.78%. The damping ratio of MRE isolator is decreased with an increase in amplitude of excitation. At 0 A input current, the damping ratio is decreased from 0.28 to 0.1 as the input amplitude of excitation is varied from 1.25 mm to 1.65 mm (Yarra et al. 2019). At 3 A input current, the corresponding changes in damping ratio is from 0.22 to 0.16. The damping in the MRE isolator is due to frictional sliding at the interfaces between the free rubber and the particles (Fan et al. 2011). At low strain levels, the particle can easily slide over the rubber, causing friction and thus resulting in higher damping ratio. At higher strain levels, the rubber locks the particle and partially allows the particle to slide over the rubber, resulting in relatively lower damping (Liu et al. 2020). The relative increase in damping ratio under 0 A and 3 A current input with increasing excitation amplitude is from -22.91% to 67% indicates that damping improves higher for large strains than lower strain under magnetic field.

4.5   Chapter conclusions

Designed a test set-up for testing the performance of the MRE isolator under different current inputs to the isolator and the amplitude of excitation for sweep frequencies.

By varying the current input to the MRE isolator from 0 A to 3 A, the percentage increase in relative stiffness of the MRE changes is found to be 184.7%, and the natural frequency shifts from 28 Hz to 47.2 Hz. These results conclude that the MRE isolator changes the stiffness with the applied magnetics.

By varying the amplitude of excitation to the MRE isolator from 1.25 mm to 2.25 mm under 0 A and 3 A current input, the performance of the isolator was evaluated. In the MRE isolator under passive state with increasing amplitude of excitation, the natural frequency of the system reduces, which is due to the Payne effect. When the MRE isolator is subjected to the maximum magnetic field, the relative increase in stiffness

of the MRE is reduced from 190% (compared to the passive state) to 154.7%. This indicates that the Payne effect, which causes an increase in stiffness with increasing magnetic field, is more pronounced in the magnetized state than in the passive state. This concludes that the Payne effect is more predominant in the magnetized state than in the passive state. The damping property of the MRE isolator improves better during the magnetized state than passive state.

Chapter 5

MATHEMATICAL MODELLING OF MRE ISOLATOR

Summary

In this chapter, the viscoelastic model for MRE isolator is developed in the frequency domain. The viscoelastic model is composed of Zener and Bouc-Wen components, which reflect the system's viscoelasticity and hysteresis. The parameters of the generated viscoelastic model are dependent on the current input to the isolator and the magnitude of excitation. To estimate the model parameter under the effect of current input, MATLAB's system identification toolbox is used to estimate a linear state space equation from experimental data under varying magnetic fields. Later, the parameters of the viscoelastic model are calculated by minimising the mean square error between the linear state space model response and the viscoelastic model state space response. The function is minimised using the gradient descent approach included in the MATLAB optimization package. Once the model parameters of the viscoelastic model are determined, a polynomial equation is used to determine the link between the model parameter and the current input to the isolator. The developed model matches the linear state space model with a maximum of 96.66% accuracy and a minimum of 89.47% accuracy.

The amplitude dependence model parameter is computed using the CS frequency. The viscoelastic model parameters are determined based on the modification of the model's current input (previously established magnetic-dependent viscoelastic model) such that the CS frequency in the generated model matches the experimental value.

5.1 Introduction

Adopting phenomenological modelling methodologies based on viscoelastic constitutive relations is used to describe the prediction of MRE isolator response. These models

91

are constructed within the framework of a spring and a dashpot, which concurrently explain the magnetic field and magnitude of excitation. As described in Chapter 2, model estimation for response of the system for single frequency in time domain required large number of experiments to develop the full fledged model. To overcome that, model developed in frequency domain has more advantages and reduces the number of experiments and time.

In this chapter, developing a mathematical model for the system via a simplified approach based on the CS frequency. The MRE isolator is mathematically modelled using viscoelastic model and the state space approach was used to identify the viscoelastic parameters. The viscoelastic model considered for present work consists of Zener and Bouc-wen elements. The Zener viscoelastic model represents the viscoelastic material properties of the MRE whereas Bouc-Wen represents the hysteresis properties and this element traces the transmissibility of the MRE isolator accurately over the wide frequency. The current and excitation amplitude are depended variables, their interaction can affect the behaviour of the MRE isolator. Therefore, to simplify the model and enable prediction of the MRE response at different amplitudes using a controller stopping criteria, a relationship between the current and the excitation amplitude was established. This relationship allows for more accurate modelling of the MRE behaviour and can help optimize the design of MRE-based systems. The amplitude dependent properties of the viscoelastic model are estimated by relating the current input to the MRE isolator model to the excitation amplitude based on the CS frequency.
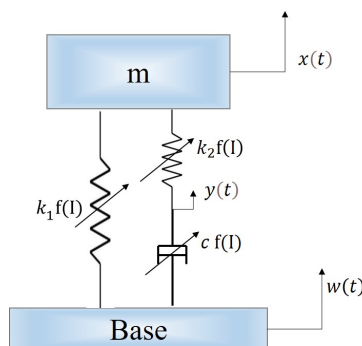
Figure 5.1: Zener SDOF transmissibility model

5.2 Zener Viscoelastic model

The viscoelastic behavior of the MRE was modelled as Zener element since the model correctly predicts the behavior of a viscoelastic solid. In Figure 5.1, the Zener based mathematically model of the MRE isolator is represented. The system is excited with input displacement $w(t)$ and the isolator response $x(t)$ at the inertial mass (m). The MRE represented by an equivalent Zener viscoelastic model, which contains spring k_1 parallel to a series of elements damper c and spring k_2.

The movement of differential equation of the mathematical model in complex domain is represented as

$$m\ddot{x}(t) + k_1(x(t) - w(t)) + c(\dot{x}(t) - \dot{y}(t)) = 0 \tag{5.1}$$

$$k_2(y(t) - w(t)) = c(\dot{x}(t) - \dot{y}(t)) \tag{5.2}$$

The displacement amplitude of input excitation $w(t)$, response $x(t)$ and intermitted $y(t)$ is

$$w(t) = W_0 e^{j\omega t} \tag{5.3}$$

$$x(t) = Xe^{j\omega t} = X_0 e^{j\theta} \tag{5.4}$$

$$y(t) = Ye^{j\omega t} \tag{5.5}$$

The substitute the equation 5.3,5.4 and 5.5 in equation 5.1 and 5.2, the system equation rewritten as

$$-m\omega^2 X + k_1(X - W_0) + jc\omega(X - Y) = 0 \tag{5.6}$$

$$k_2(Y - W_0) = c\omega(X - Y) \tag{5.7}$$

then

$$Y = X\frac{jc\omega + W_0}{k_2 + jc\omega}X_0 e^{j\theta} \tag{5.8}$$

$$X = \frac{k_1 k_2 W_0 + jck_1 W_0 \omega}{k_2 (k_1 - m\omega^2) + jc\omega(k_2 + W_0)(k_1 - m\omega^2)} \qquad (5.9)$$

Let $A = (k_1 - m\omega^2)$

$$X = \frac{k_1 k_2^2 A W_0 - c^2 \omega^2 k_1 W_0 (k_2 + W_0) + j[k_1 k_2 c\omega W_0 A (k_2 + W_0) + ck_1 k_2 A W_0 \omega]}{(k_2 A)^2 + (c\omega(k_2 + W_0)A)^2} \qquad (5.10)$$

Let $\alpha = k_1 k_2^2 A - c^2 \omega^2 k_1 (k_2 + W_0)$ and $\beta = [k_1 k_2 c\omega A (k_2 + W_0) + ck_1 k_2 A \omega]$ and $\gamma = (k_2 A)^2 + (c\omega(k_2 + W_0)A)^2$

Then

$$X = W_0 \frac{\alpha + j\beta}{\gamma} = X_0 e^{j\theta} \qquad (5.11)$$

Modulus of the X

$$|X|^2 = X_0^2 = W_0^2 \left[\left(\frac{\alpha}{\gamma}\right)^2 + \left(\frac{\beta}{\gamma}\right)^2 \right] \qquad (5.12)$$

Then, the amplitude X_0 and phase θ of the response is

$$X_0 = W_0 \sqrt{\left[\left(\frac{\alpha}{\gamma}\right)^2 + \left(\frac{\beta}{\gamma}\right)^2 \right]} \qquad (5.13)$$

$$\theta = tan^{-1}\left(\frac{\beta}{\alpha}\right) \qquad (5.14)$$

Then response of the system is

$$x(t) = W_0 \sqrt{\left[\left(\frac{\alpha}{\gamma}\right)^2 + \left(\frac{\beta}{\gamma}\right)^2 \right]} \sin\left(\omega t + tan^{-1}\left(\frac{\beta}{\alpha}\right)\right) \qquad (5.15)$$

Equation 5.15 confirms that the displacement response of the MRE isolator varies with the frequency. Apart from frequency, the response of MRE is also influenced by the input strain and the magnetic field.
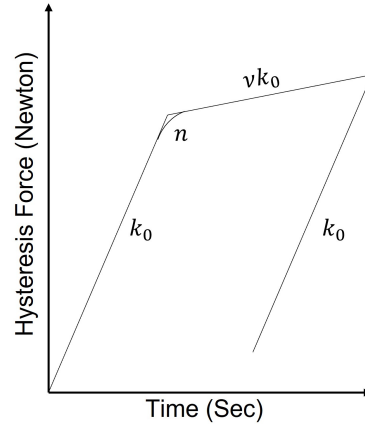
Figure 5.2: Hysteresis loop of Bouc-Wen

5.3 Bouc–Wen Model

The hysteresis behavior of the MRE isolator was estimated using Bouc–Wen model. The Bouc–Wen model is a hysteretic model that is frequently utilized in engineering and scientific research. Furthermore, the hysteretic restoring force of model and displacement diagram is continuous and smooth. The model, depicted in Figure 5.2, can be used to simulate the restoring force of the MRE isolator.

The force–displacement relationship of this model is expressed as follows:

$$F(x) = vk_0 x + (1 - v)k_0 z \tag{5.16}$$

In addition, the derivative component of hysteretic force z is

$$\dot{z} = \frac{1}{x_y} \left(A\dot{x}(t) - \beta \dot{x}(t) |z^n(t)| - \alpha |\dot{x}(t)| z^n(t) \right) \quad n = 1, 3, 5 \ldots \ldots \tag{5.17}$$

where, z is the hysteretic displacement of the system, A denotes the area of the hysteretic loop, and the shape of the hysteretic loop is controlled by parameters β and α, n denotes the smoothness of the hysteretic curve and v represents the ratio of the back-to-front stiffness of the yield value.

The hysteretic properties of the structure will change in different ways depending on the values of the parameters β and α. When $\beta + \alpha > 0$, as illustrated in Figure 5.3 (a), (b), (c), the structure exhibits soft characteristics, and hysteretic restoring force of the system decreases as the displacement response increases. In the loading stage, the structure is linear when $\beta + \alpha = 0$. When $\beta + \alpha = 0$, the structure hardens, and hysteretic

95

$(\alpha_{\text{Wen}} = \beta_{\text{OPS}}, \beta_{\text{Wen}} = \gamma_{\text{OPS}})$ from Wen, 1976
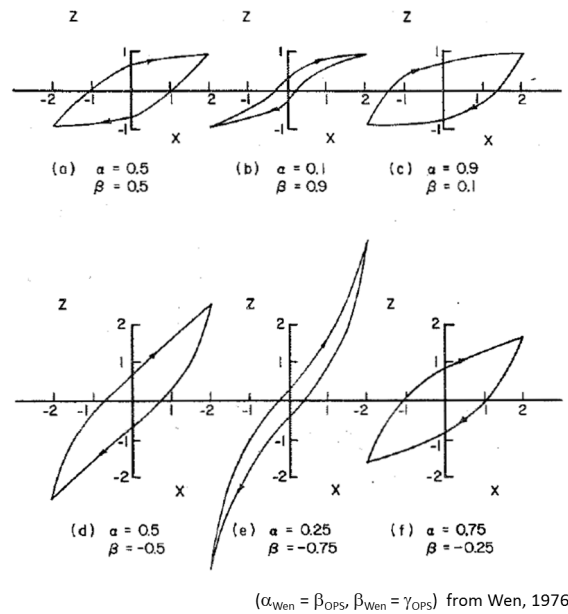
Figure 5.3: Influence of parameters on the hysteresis behaviour (Wen 1976)

restoring force of the system increases as the displacement response increases. Figure 5.3 (b), (d) show that when the ratio of $\beta|\alpha|$ is relatively large, the enveloping graph of the system hysteretic restoring force curve is larger and the curve shape is relatively full, demonstrating that the structural system consumes more energy under this parameter. When the ratio is small, the overall enveloped area of Figure 5.3 (c), (d), (e), (f) is small, and the energy dissipation characteristics of the structural system are relatively weak in comparison to the others.
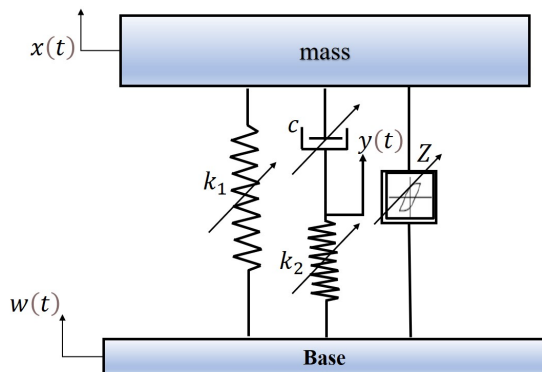
Figure 5.4: Viscoelastic model of the MRE isolator

5.4   State-space-equation of MRE isolator

A single-degree-of-freedom system (SDOF) representation of the MRE isolator model is shown in Figure 5.4. The model comprises of Zener (Nguyen et al. 2018b) and Bouc-Wen (Yu et al. 2015c) combined together, representing the viscoelastic and hysteresis behaviour of the MRE isolator. The governing equation of the MRE isolator model with the Zener and Bouc-Wen elements is,

$$m\ddot{x}(t) + (k_1 + \delta k_1)(x(t) - w(t)) + (c + \delta c)(\dot{x}t - \dot{y}t) + z = 0 \qquad (5.18)$$

$$(k_2 + \delta k_2)(y(t) - w(t)) = (c + \delta c)(\dot{x}t - \dot{y}t) \qquad (5.19)$$

where, z is hysteretic force. δk_1, δk_2 and δc parameters are the change of properties under the influence of the magnetic field.

$$\dot{z} = \alpha\,(\dot{x}(t) - \dot{w}(t)) - \beta\,|\dot{x}(t) - \dot{w}(t)|\,z - \gamma\,|z|\,(\dot{x}(t) - \dot{w}(t)) \qquad (5.20)$$

where, α, β and γ are non-dimensional parameters responsible for the shape and size of the hysteretic loops.

The state-space equation for the system given as

$$\begin{bmatrix} \dot{x}(t) \\ \ddot{x}(t) \\ \dot{y}(t) \\ \ddot{y}(t) \\ \dot{z}(t) \end{bmatrix} = \begin{bmatrix} 0 & 1 & 0 & 0 & 0 \\ -\frac{(k_1+\delta k_1)}{m} & -\frac{(c+\delta c)}{m} & 0 & \frac{(c+\delta c)}{m} & -\frac{1}{m} \\ 0 & 1 & -\frac{(k_2+\delta k_2)}{(c+\delta c)} & 0 & 0 \\ 0 & 0 & d_3 & 0 & 0 \\ 0 & \alpha & 0 & 0 & 0 \end{bmatrix} \begin{bmatrix} x(t) \\ \dot{x}(t) \\ y(t) \\ \dot{y}(t) \\ z(t) \end{bmatrix} + \begin{bmatrix} 0 & 0 \\ \frac{(k_1+\delta k_1)}{m} & 0 \\ \frac{(k_2+k2)}{(c+\delta c)} & 0 \\ 0 & 0 \\ 0 & -\alpha \end{bmatrix}$$

97

$$\begin{bmatrix} w(t) \\ \dot{w}(t) \end{bmatrix} + \begin{bmatrix} 0 & 0 \\ 0 & 0 \\ 0 & 0 \\ 0 & 0 \\ -\beta & -\gamma \end{bmatrix} \begin{bmatrix} |\dot{x}(t) - \dot{w}(t)| z(t) \\ (\dot{x}(t) - \dot{w}(t) |z(t)| \end{bmatrix}$$

$$(5.21)$$

where, $x(t)$, $y(t)$ and $w(t)$ are the response, intermitted, and input excitation in time-domain signals. The MRE isolator viscoelastic model parameters are sensitive to the magnetic field, excitation amplitude, and frequency. To incorporate the control strategies, identification of these parameters is crucial. A procedure to identify the parameters are discussed in the following section.
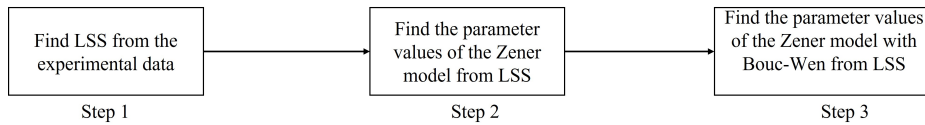
Figure 5.5: Steps for identifying viscoelastic model parameters

5.5 Viscoelastic model parameter identification procedure

MRE isolator properties are strongly nonlinear functions of magnetic flux density, excitation frequency, and displacement amplitude. Considering all the parameters and developing a mathematical model for MRE isolator is quite a difficult task, since it involves the nonlinearity. A distinction between the linear and nonlinear response in a viscoelastic material is depicted in Figure 5.7. The force and displacement signal under the linear region is represented in Figure 5.7 (a) and (b). Corresponding signals under the nonlinear region are represented in Figure 5.7 (e) and (f). The frequency-domain representation of the force signal under the linear and nonlinear regime is illustrated in Figure 5.7 (c) and (g) respectively. By eliminating the parameter t, the viscoelastic response is represented in the form of a force-displacement hysteresis loop. In linear viscoelastic region, the hysteresis loop will be a proper ellipse (Figure 5.7 (d)). The con-

$$J = \sum_{i=1}^{N} (x_{Exp}(i) - x_{Model}(i))^2$$
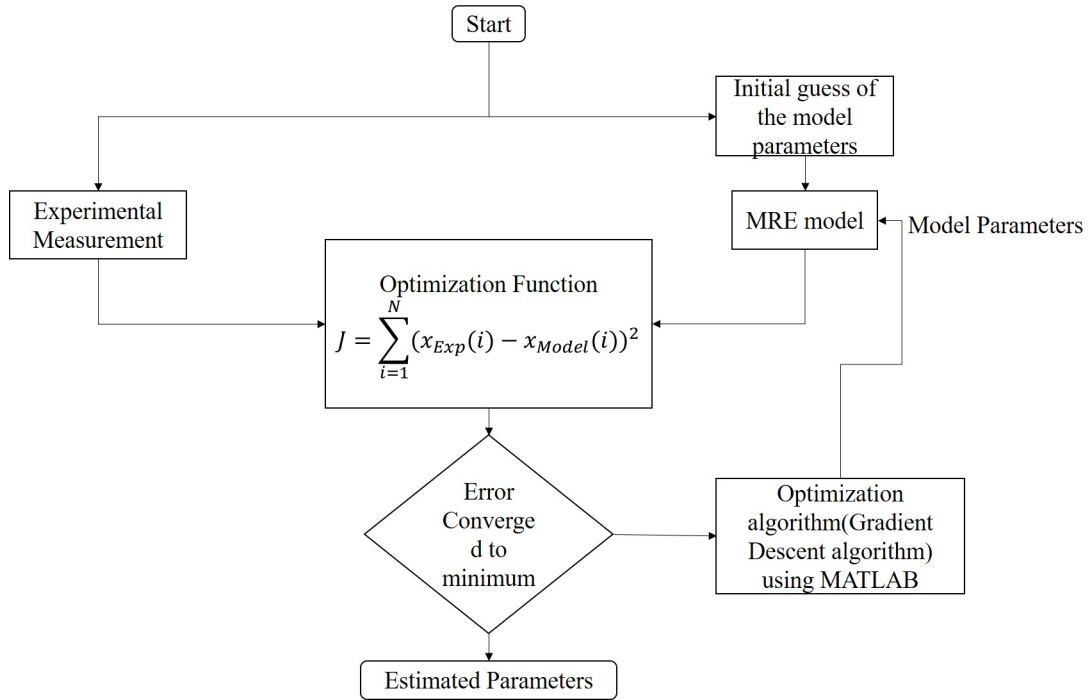
Figure 5.6: Flow chart of identifying model parameters
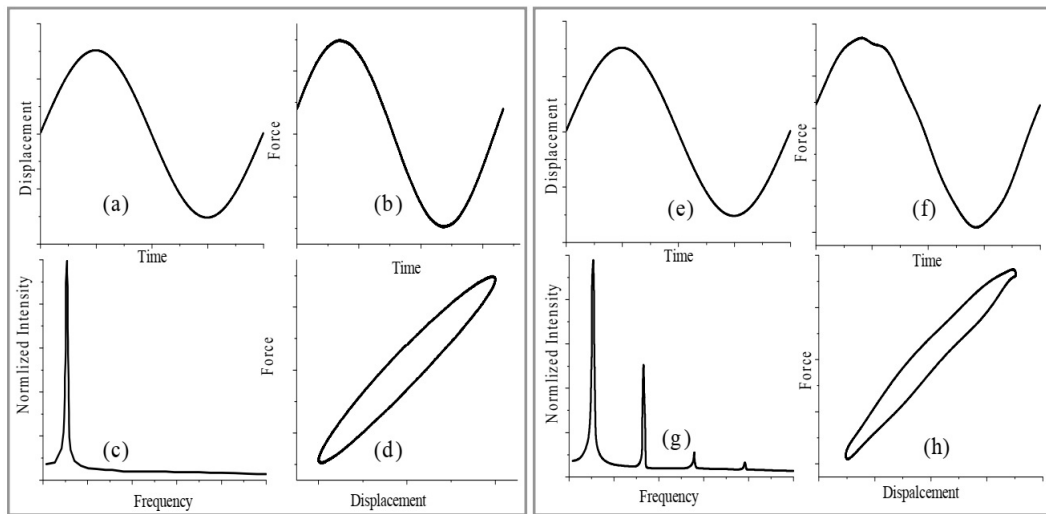
Figure 5.7: (a) Input displacement, (b) Output response of force, (c) Frequency domain representation of response force (d) Hysteresis plot corresponding to linear response of a viscoelastic material. (e) Input displacement, (f) Output response of force, (g) Frequency domain representation of response force (h) Hysteresis plot corresponding to nonlinear response of a viscoelastic material.

tribution from high-order harmonics gives rise to a non-elliptical shape of the hysteresis loop, which represents the nonlinear viscoelastic behavior (Figure 5.7 (h)).

To simplify this process, in the current work, the nonlinear response of the MRE isolator is converted to linear response using the system identification toolkit in the MATLAB, and then the MRE isolator is represented as a second order linear state space

(LSS) equation. The linear state space matrix identified from system identification process is nonparametric in nature and its parametric form of viscoelastic model is obtained by using optimization toolkit in MATLAB (Li et al. 2010). The method of estimating the model parameter is presented in the Figure 5.6. For the given optimization function, the parameter of the model is identified using optimization algorithm (for present case gradient descent algorithm) using MATLAB optimization toolkit. Figure 5.5. depicts the process of determining the parameters of the viscoelastic state-space model. The following paragraph provides a detailed description of each individual process.

Step1: In this stage, a linear second-order state-space equation is extracted using the MATLAB system identification toolkit for the measured input and output sine sweep signal. Continuous time-domain second-representation of the order state-space model is,

$$\frac{ds}{dy} = A\, s\,(t) + B\, u\,(t) \tag{5.22}$$

$$x_{NPSS}(t) = C\, s\,(t) + D\, u(t) \tag{5.23}$$

where, $s(t)$ is the state vector, $u(t)$ is the input vector, $x_{NPSS}(t)$ is displacement response of the nonparametric the state-space equation. Matrix A is the state matrix, B is the input matrix, C is the output matrix, and D is the feedthrough matrix

Step 2: The state-space equation obtained in step 1 is in nonparametric form, and it does not have any physical meaning. The model is represented in parametric form by incorporating in Zener based state-space equation. The parameters of this model are identified using Simulink parameter optimization toolkit by minimizing the sum squared error between Zener parametric state-space response $(x_{ZPSS}\,(t)$ and NPSS (nonparametric state space model) response (x_{NPSS}). The parametric form of the model with Zener based viscoelastic state-space model response is expressed as,

$$\begin{bmatrix} \dot{x}(t)_{PSS} \\ \ddot{x}(t)_{PSS} \\ \dot{y}(t) \\ \ddot{y}(t) \end{bmatrix} = \begin{bmatrix} 0 & 1 & 0 & 0 \\ -k_1/m & -c/m & 0 & c/m \\ 0 & 1 & -k_2/c & 0 \\ 0 & 0 & 0 & 0 \end{bmatrix} \begin{bmatrix} x(t)_{PSS} \\ \dot{x}(t)_{PSS} \\ y(t) \\ \dot{y}(t) \end{bmatrix} + \begin{bmatrix} 0 & 0 \\ k_1/m & 0 \\ k_2/c & 0 \\ 0 & 0 \end{bmatrix} \begin{bmatrix} w(t) \\ \dot{w}(t) \end{bmatrix}$$

$$\tag{5.24}$$

$$x_{ZPSS}(t) = \int \int \left(\begin{bmatrix} -k_1/m & -c/m & 0 & c/m \end{bmatrix} \begin{bmatrix} x(t) \\ \dot{x}(t) \\ y(t) \\ \dot{y}(t) \\ z(t) \end{bmatrix} + \begin{bmatrix} k_1/m & 0 \end{bmatrix} \begin{bmatrix} w(t) \\ \dot{w}(t) \end{bmatrix} \right) dt$$

$$\tag{5.25}$$

The objective function to find the parameters of the Zener based visco-elastic model is (Peng et al. 2014)

$$J = \sum_{i=1}^{N} \left(x_{ZPSS}(i) - x_{NPSS}(i) \right)^2 \tag{5.26}$$

Where, N denotes the number of data available in the signal. Step 3: The Bouc-Wen is a hysteresis element considered for modelling the hysteresis behavior. Its parameters are identified using Simulink parameter optimization toolkit by minimizing the sum squared error between NPSS response $(x_{NPSS}(t))$ and the viscoelastic state-space model (VSS) response $(x_{VSS}(t))$. The response of the viscoelastic state-space model expressed as

$$\ddot{x}_{VSS} = \begin{bmatrix} -(k_1 + k_1)/m & -(c+c)/m & 0 & (c+c)/m & -1/m \end{bmatrix} \begin{bmatrix} x(t) \\ \dot{x}(t) \\ y(t) \\ \dot{y}(t) \\ z(t) \end{bmatrix} + \begin{bmatrix} (k_1 + k_1)/m & 0 \end{bmatrix}$$

$$\begin{bmatrix} w(t) \\ \dot{w}(t) \end{bmatrix} + \begin{bmatrix} 0 & 0 \end{bmatrix} \begin{bmatrix} |\dot{x}(t) - \dot{w}(t)| z(t) \\ (\dot{x}(t) - \dot{w}(t) |z(t)|) \end{bmatrix}$$

$$\tag{5.27}$$

$$x_{VSS} = \int \int \ddot{x}_{VSS} dt \tag{5.28}$$

The objective function to find the Bouc-Wen parameter is

$$J = \sum_{i=1}^{N} (x_{VSS}(i) - x_{NPSS}(i))^2 \qquad (5.29)$$

5.6 Parameter estimation and generalizing the variation with respect to the input current

Table 5.1: Linear state-space matrix identified from MATLAB system identification toolkit

Current (A)	A	B	C	D	Best Fit
0	$\begin{bmatrix} -41.28 & -233.2 \\ 139.5 & -50.73 \end{bmatrix}$	$\begin{bmatrix} -4433 \\ 6568 \end{bmatrix}$	$\begin{bmatrix} -0.02091 & 0.0007475 \end{bmatrix}$	[0]	81.84%
0.5	$\begin{bmatrix} -39.09 & -251.8 \\ 147.6 & -64.51 \end{bmatrix}$	$\begin{bmatrix} 5409 \\ -7936 \end{bmatrix}$	$\begin{bmatrix} 0.01798 & -0.0006775 \end{bmatrix}$	[0]	83.74%
1	$\begin{bmatrix} -34.31 & -275.1 \\ 166.4 & -74.49 \end{bmatrix}$	$\begin{bmatrix} 5454 \\ -1.028e4 \end{bmatrix}$	$\begin{bmatrix} 0.01576 & -0.0006483 \end{bmatrix}$	[0]	86.5%
1.5	$\begin{bmatrix} -19.73 & -298.4 \\ 200.3 & -96.28 \end{bmatrix}$	$\begin{bmatrix} -6522 \\ -1.388e4 \end{bmatrix}$	$\begin{bmatrix} -0.01341 & 0.0005952 \end{bmatrix}$	[0]	88.93%
2	$\begin{bmatrix} -13.4 & -320.7 \\ 228.3 & -105.8 \end{bmatrix}$	$\begin{bmatrix} -7199 \\ 1.799e4 \end{bmatrix}$	$\begin{bmatrix} -0.01172 & 0.0005517 \end{bmatrix}$	[0]	90.87%
2.5	$\begin{bmatrix} -10.04 & -343.8 \\ 247 & -116.6 \end{bmatrix}$	$\begin{bmatrix} -8478 \\ 2.162e4 \end{bmatrix}$	$\begin{bmatrix} -0.01044 & 0.0005271 \end{bmatrix}$	[0]	92.34%
3	$\begin{bmatrix} -8.749 & 361.8 \\ -262.5 & -122.4 \end{bmatrix}$	$\begin{bmatrix} 9288 \\ 2.534e4 \end{bmatrix}$	$\begin{bmatrix} 0.009468 & 0.0004949 \end{bmatrix}$	[0]	93.2%

Table 5.1 shows the nonparametric linear second order state space matrix estimated

using the system identification toolkit (MATLAB) for various input currents. The state space matrix is linear, and its linearity component is assessed in terms of best fit (Estimated from system identification toolkit from MATLAB), which represents the percentage of fit with respect to experimental data. For an input current of 0 A, the linear state space matrix provides the best fit of about 81.84%. This indicates that the MRE isolator has a nonlinearity of approximately around 18.16%. The nonlinearity in the MRE isolator decreases from 18.16% to 6.8% as the current to the isolator increases from 0 A to 3 A.

When a material undergoes deformation, it can exhibit nonlinear behaviour. This means that the relationship between the applied force and the resulting deformation is not proportional, and can change depending on the magnitude and type of force applied. This is often the case when the material is subjected to large forces, such as in high-impact applications or when subjected to high-frequency vibrations. However, increasing the stiffness of the material can often lead to a decrease in the material's nonlinearity response to excitation. This is because a stiffer material is less prone to deforming in response to external forces, and is therefore less likely to exhibit nonlinear behavior. As a result, the system becomes more linear, which means that the relationship between the applied force and the resulting deformation becomes more predictable and proportional. In other words, increasing material stiffness can help to mitigate the nonlinear behaviour of the material, resulting in a more linear response to excitation. This can be beneficial in many applications, as a more predictable and proportional response can make it easier to design and control systems

The parameters of the Zener viscoelastic model for different current input to MRE isolator estimated from optimization process are listed in Table 5.2. The hysteresis behaviour accounts for the nonlinearity present in the transmissibility response. The source of non-linearity is either the magnetic field or the input strain (Wang et al. 2017). In the present study, the hysteresis element Bouc-Wen parameters were estimated only for the response corresponding to 0 A input current and 1.5 mm amplitude of excitation. The corresponding Bouc-Wen parameters α, β, γ, and n estimated from optimization process are -2172, 30, 30, and 1, respectively. The Bouc-Wen parameters for other current inputs are also same as that for 0 A input current. By considering that the maximum error achieved by the viscoelastic model for other current input in estimating the experimen-

tal natural frequency and transmissibility at natural frequency is about 1.6% and 3.8%. Hence, Bouc-Wen parameters for other current input considering 0 A current input is justified.

Table 5.2: Identified optimized Zener model parameter

Current	Model Parameters		
(A)	k_1 (KN/m)	c (N-s/m)	k_2 (KN/m)
0	30.52	63.89	557.72
1	38.58	75.91	612.52
2	58.08	84.46	669.39
3	73.63	98.77	711.36
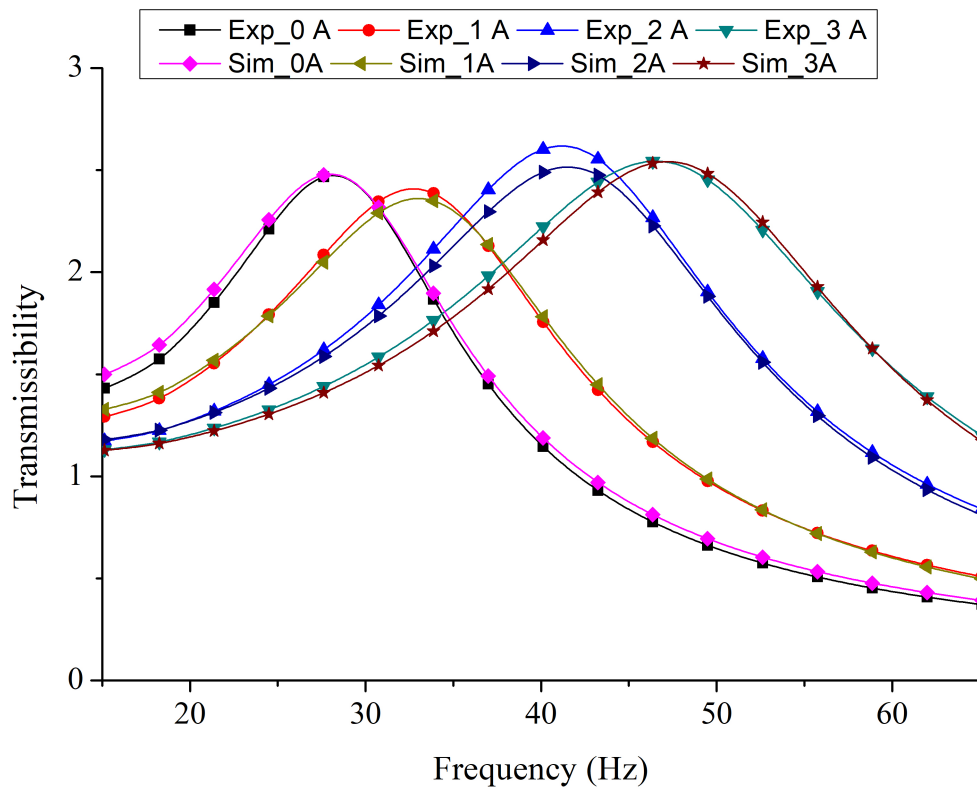
Figure 5.8: Comparison between experimental transmissibility and the viscoelastic model optimized parameter transmissibility for current input 0 A,1 A, 2 A and 3 A

A comparison between the experimental and the predicted transmissibility response from the viscoelastic model with optimized parameters at different current inputs is presented in Figure 5.8. It can be visualized that; the viscoelastic model accurately predicts the natural frequency of the MRE isolator with the least error of 1.6% registered at 2 A input current. However, the magnitude of transmissibility predicted by the model at the natural frequency deviates with respect to the experimental data, with a maximum error of 3.8% corresponding to the 2 A input current. The corresponding error for an input current of 1 A is 1.53%, and it is negligible for 0 A and 3 A input currents. At 0 A input current, the predicted response by the optimized parameters of the viscoelastic model perfectly simulates transmissibility response, but for other current inputs, the model estimates natural frequency for transmissibility rather than amplitude, especially for 1 A and 2 A current input. This disparity is primarily due to the hysteresis behaviour accounted for in the model.
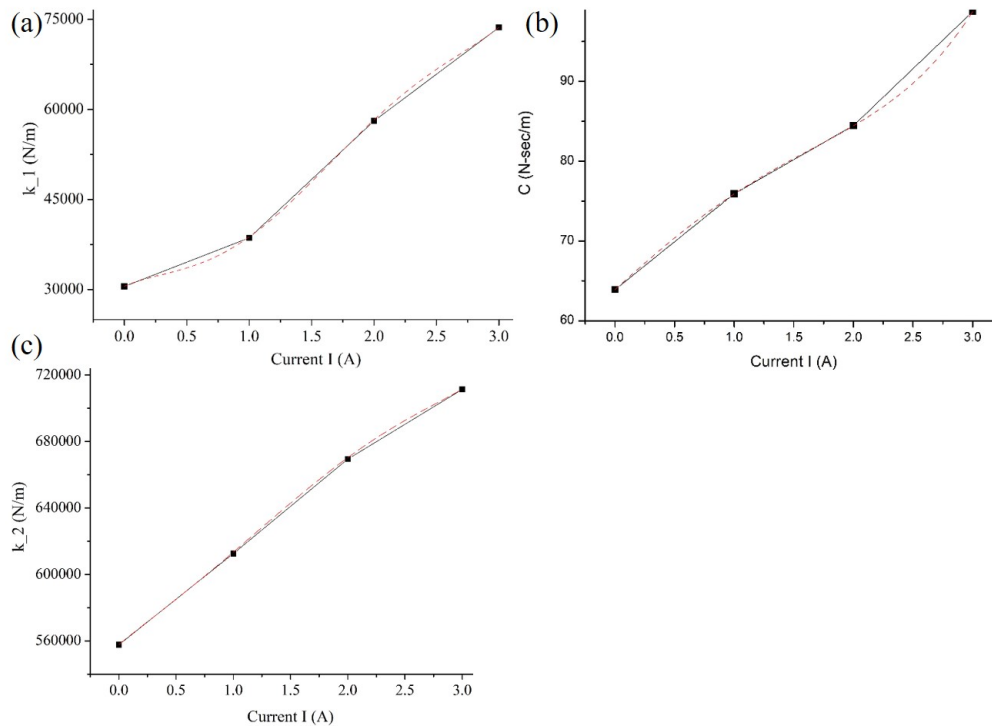
Figure 5.9: Curv Fitting of model parameters

To implement the control strategies in the MRE isolator, the viscoelastic model parameter under variation of current input must be generalized. A 5th order polynomial function is chosen to generalize the variation of the parameters with respect to the input current i. The chosen polynomial equation coefficient estimated by using curve fitting

technique. The curve fitting of the experimental data is shown in Figure 5.9. The mathematical expression for generalizing variation in the Zener model parameters is

$$k_1 f(I) = 1112i^5 - 8628i^4 + 21400i^3 - 14860i^2 + 9201i + 30540 \qquad (5.30)$$

$$cf(I) = -0.010667i^5 + 0.62364i^4 - 1.9485i^3 - 0.083182i^2 + 13.415i + 63.888 \quad (5.31)$$

$$k_2 f(I) = 331.3i^5 - 4394i^4 + 10840i^3 + 10840i^2 + 49240i + 557900 \qquad (5.32)$$
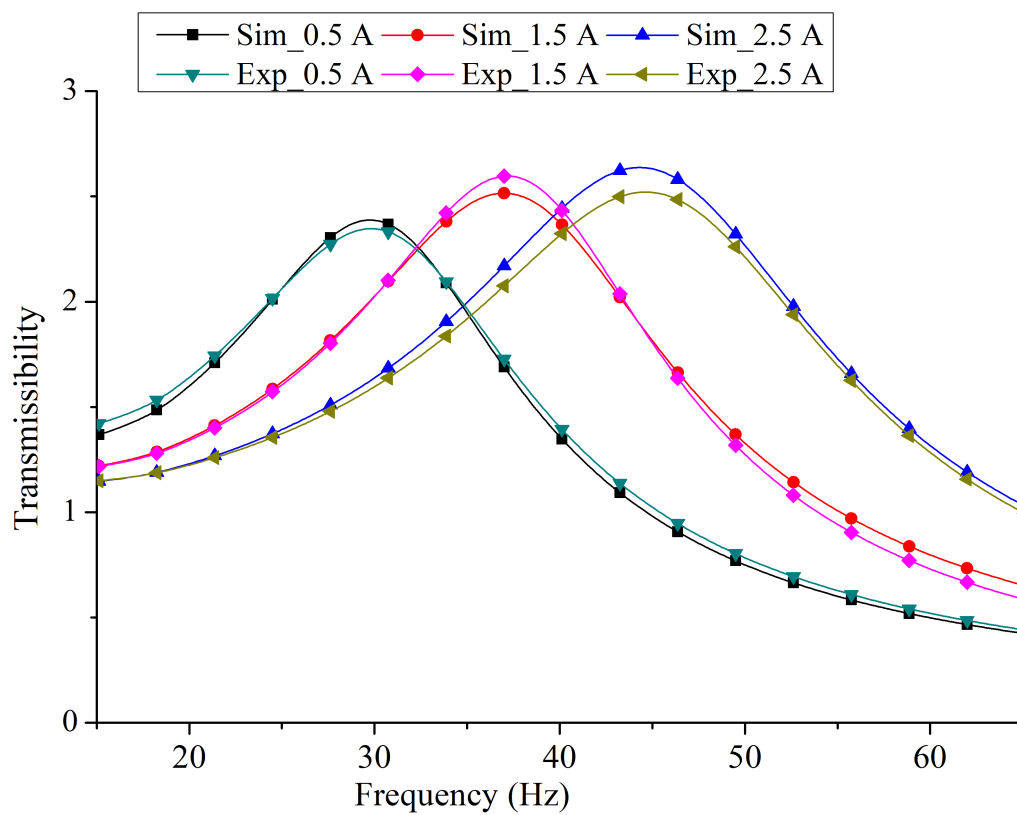
Figure 5.10: A comparison between the Experimental and generalised mathematical expression predicted transmissibility response for current input 0.5 A,1.5 A and 2.5 A

The mathematical expression to generalize the variation in parameters of the Zener model parameters with the applied current is obtained with respect to the input currents of 0 A,1 A, 2 A and 3 A. However, for developing model-based control, it is important to assess the ability of the generalized expression to predict the transmissibility response of MRE isolator. The ability of the proposed model to predict the transmissibility response is assessed in terms of the responses are estimated at 0.5 A, 1.5 A and 2.5 A. The values of the parameters corresponding to this input current are estimated using the

Equation 5.30, 5.31 and 5.21 and substituted in Equation 5.31 to get the model predicted transmissibility response.

A comparison between the experimentally determined transmissibility response and the model predicted response at 0.5 A, 1.5 A, and 2.5 A is presented in Figure 5.10. As visualized in Figure 5.10, the transmissibility responses predicted by the model effectively portray the experimentally determined responses at 0.5 A, 1 A, and 2.5 A. The model predicts the natural frequency of isolator with an error of less than 1%. The model, however, indicates that the error in estimating the amplitude of the transmissibility is approximately 4.6% for 2.5 A, 3.2% for 1.5 A, and 1.7% for 0.5 A. It is concluded that the developed viscoelastic model efficiently estimates the natural frequency of the MRE isolator, but less efficiently estimates the amplitude of transmissibility for few currents.

The ability of the model in portraying the experimentally determined is expressed in terms of fitness value. The fitness values are estimated from Equation 5.33 which is given below.

$$FT\% = \left[\frac{\text{norm}(T_P - T_E)}{\text{norm}(T_P - \text{mean}(T_E))} \right] \text{ x } 100 \qquad (5.33)$$

where, T_P predicted transmissibility and T_E experimental transmissibility of the MRE isolator

In Table 5.3, The fitness value of the model predicted response is least about 89.47% for 2.5 A and highest about 96.66% for 1 A and 0.5 A, implying that model moderately fit the experiment transmissibility can be used for control implementation.

Table 5.3: Fitness value of the viscoelastic model for different current

	Applied Current on the MRE isolator						
Fitness value%	0 A	0.5 A	1 A	1.5 A	2 A	2.5 A	3 A
	95.23	96.66	96.66	92.46	92.06	89.47	93.29
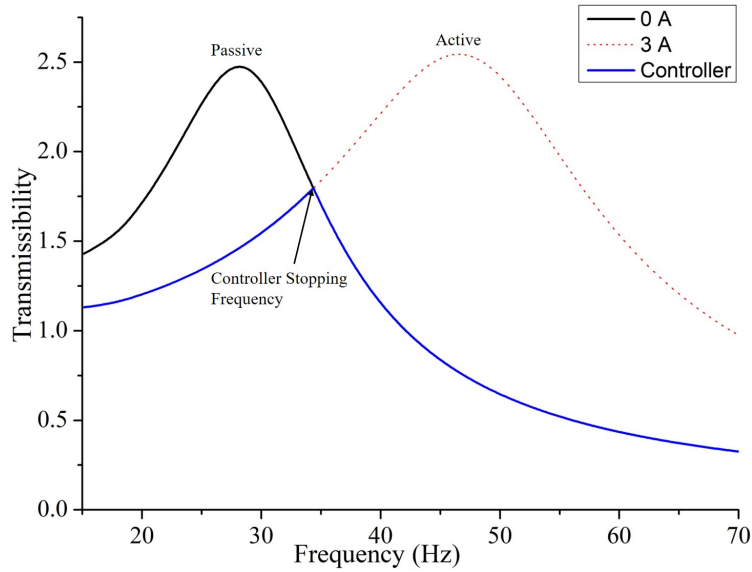
Figure 5.11: Transmissibility plot of MRE isolator

5.7 The relationship between the excitation amplitude and current supplied to the isolator

The transmissibility response differs with the change in input amplitude of excitation under passive as well as active states. To develop an effective control strategy, these responses need to be represented in the form of mathematical expressions where the parameters of the viscoelastic models are identified for each amplitude of excitation under passive and active states. This approach is time-consuming and requires a huge amount of experimental data. To simplify this process, a novel method based on the CS frequency is developed to incorporate the amplitude-dependent attributes to the MRE isolator model. The CS frequency concept is formulated based on the operation of an efficient controller. This concept is illustrated by the frequency response curves shown in Figure 5.11. The response of MRE isolator under passive state (0 A) is represented by a frequency response curve with lower natural frequency, and the active state (3 A) is characterized by a response curve with higher natural frequency. To restrict the isolator system from reaching the resonance region corresponding to the passive state, the controller should be operated under active state so that it traces the response curve corresponding to the 3 A input current. The controller should turn off the supply to the isolator when it reaches the frequency corresponding to the intersection of the active and passive state, representing the CS frequency. In addition, it is very important that

the control signal should be off at the stopping frequency so that the isolator traces the response curve corresponding to the passive state; otherwise, the isolator system passes through the resonance region of the active state, and violates the law of the efficient controller.

Table 5.4: Required current input for the model-based controller for the change of excitation input

Excitation amplitude(mm)	CS frequency (Hz)	Current Input (A)	
		Exp	Model
1.25	39.51	3	4.8
1.50	35.16	3	3.4
1.75	34.52	3	3
2	34.25	3	2.85
2.25	33.78	3	2.55

For developing a controller based on the controller stopping frequency, it is important to identify different amplitudes of excitation. The controller stopping frequencies estimated from the displacement transmissibility test corresponding to different amplitudes of excitation (Figure 4.5) are listed in Table 5.4. As evident from the experimental response (Figure 4.5) and model-predicted response (Figure 5.8) plots, the difference exists with respect to the controller stopping frequency. For example, the CS frequency for the transmissibility response of MRE isolator model corresponding to 1.50 mm amplitude of excitation is 34.8 Hz and the corresponding value estimated from experimental is 35.16 Hz. This difference needs to be accounted otherwise; it deteriorates the performance of the controller. To match the experimentally determined stopping frequency, the current input I to the model needs to be estimated. For the 1.50 mm CS frequency is lower than the experimentally determined value. This implies that the input current needs to be increased from 3 A since the CS frequency is less than the experimental value. However, for 2.25 mm amplitude of excitation, the current need to be decreased from 3 A as the CS frequency of the model is more than the experimental value. To accurately predict the CS frequency, the response of MRE isolator model for a specific amplitude of excitation under passive state is considered as a reference. For the developed isolator, the response curve corresponding to the amplitude of 1.5 mm under passive state is chosen as the references curve. With respect to this curve, the current

input to the isolator is either decreased or increased from 3 A to obtain the accurate CS frequency for the required input current and the excitation amplitude.

To incorporate semi-active control strategies, the values of viscoelastic model parameters must be estimated with respect to the amplitude of excitation as well. A polynomial function is chosen for this purpose in order to establish a generalized equation that describes the relationship between the current input to the MRE isolator model and the amplitude of excitation. The polynomial equation current I expressed as a function of excitation amplitude A is written as

$$I = 45.67 - 66866.66A + 3.5E7\,A^2 - 6.13E9\,A^3 \tag{5.34}$$

where, A denotes the amplitude of excitation.
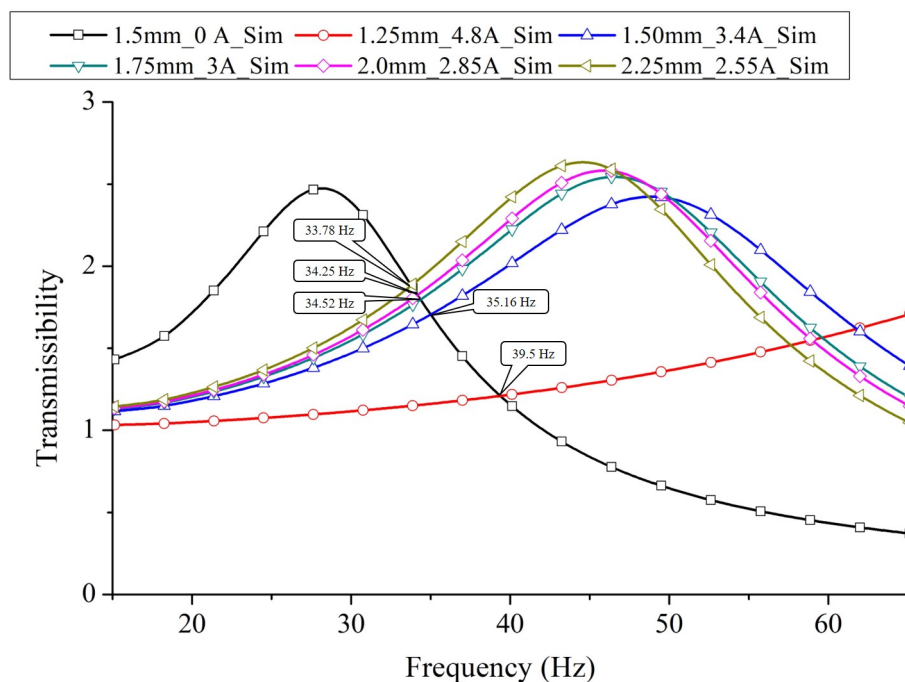
Figure 5.12: Simulated amplitude dependency of the MRE isolator

For a given amplitude of excitation, the current input I to the MRE isolator model is estimated using Equation 5.34. The parameters of the model (Equations 5.30-5.32) are estimated for this current, and the corresponding values are listed in Table 5.5. Using these parameters, the transmissibility response is estimated according to equation 5.20, and the corresponding plots for amplitudes of excitation ranging from 1.25 mm to 2.25 mm is shown in Figure 5.12. The CS frequency is the intersection of the passive

response of the MRE isolator model with its active response. This is the key parameter for developing the isolator model and model-based control technique. The experimental transmissibility test confirms that the CS frequency was decreased with the amplitude of excitation. The similar behaviour is predicted by the isolator model. At 1.25 mm amplitude, the stopping frequency of isolator corresponding to the input current of 3 A is 39.51 Hz. The same value is estimated from using the mathematical model. This confirms that CS frequency predicted by the isolator model gives a similar feature corresponding to the experimental transmissibility under different amplitudes of excitation. The developed model effectively depicted the amplitude and field sensitive responses, which can be used to develop controller algorithms.

Table 5.5: Estimated parameter values of the viscoelastic model for the different amplitude of excitation

Excitation amplitude (m)	Evaluated current (A)	Model paramter values		
		k_1 (KN/m)	c (N-s/m)	k_2 (KN/m)
1.25	4.8	272.15	236.22	834.82
1.50	3.4	844.52	121.49	748.97
1.75	3	764.43	108.56	724.45
2	2.85	742.83	105.02	715.25
2.25	2.55	700.3o	99.51	696.85

5.8   Conclusions

A parametric model for MRE isolator was developed using viscoelastic theory. For the developed viscoelastic model, parameters were estimated using an optimization function for different current inputs predicting MRE response in the frequency domain. The relationship between the current input to MRE isolator and the model parameters was established in a polynomial equation. The simulation results conclude that the model simulates the linear state space response with minimum and maximum fitness of 89% and 96% respectively.

The amplitude dependent model parameters of the MRE isolator are estimated using CS frequency. A relationship between the current input to the MRE isolator and with

amplitude of excitation is established with a polynomial equation. The simulation results conclude that the developed model accurately predicts the CS frequency of the MRE isolator.

Chapter 6

MODEL BASED AND MODEL FREE CONTROLLER FOR MRE ISOLATOR

Summary

This chapter focuses primarily on the controller development for the MRE isolator. The development of a model-based fuzzy (MBF controller) controller for providing control output depending on the position of the PCB and stopping control output based on the specified condition. In addition to the MBF controller, a model-based sliding mode controller (MBSM controller) is developed to produce the necessary response at the receiver end. The viscoelastic model generates the intended response signal of the MRE isolator, and the sliding mode controller tracks the desired response by supplying control input to the MRE isolator. In simulation, the performance of both model-based controllers under random excitation is compared, and it is determined that the MBSM controller performs more effectively than the MBF controller.

If the mathematical model for the system is unknown, a radial basis function neural network sliding mode controller is used to implement control (RBSM controller). To achieve the desired response, the weights of the neural network are changed such that the sliding mode controller generates the necessary control input to the isolator. The simulation results demonstrate that the RBSM controller functions well under all circumstances. The simulation results demonstrate that the RBSM delivers the expected control output.

6.1   Introduction

Success of MRE isolator necessitates an effective control strategy. The controller should activate the isolator for a specific frequency range of interest. When the frequency excitation reaches the isolation region, the controller should turn off and should function as a passive device. Furthermore, the controller should be adaptable to changes in amplitude

113

and frequency of excitation. The controller developed for MRE isolator can be based on the position of the oscillating member (on-off controller) or the error difference between the desired and actual. Both the type controller required a complete mathematical model for MRE isolator to generate control output.

This chapter is dedicated to the development of a model-based fuzzy controller (MBF controller) , model-based sliding mode controller (MBSM controller) and model free radial basis neural network sliding mode controller (RBSM controller) for MRE isolator.

In MBF controller, with the given excitation, the fuzzy controller generates the controller output to the MRE isolator. But this controller output is enabled and disabled depending on the control condition based on the MRE model. The controller performance is evaluated in both simulation and real-time to determine the efficiency of vibration isolation over a wide frequency range.

In a MBSM controller, the predicted desired response generated from the mathematical model is collected by the sliding mode controller to track the desired response with the provided controller output to the MRE isolator.

In model free RBSM controllers, the desired response is not known; consequently, in order to control vibration for varying frequencies and amplitudes of excitation, sliding mode controllers need to be programmed with different gain settings. The radial basis neural controller is the mechanism that enables this to take place. In order to achieve the desired response from the MRE isolator, the neural network controller makes adjustments to the weights based on the frequency and amplitude of the signal. The following section provides the complete details of the developed controller.

6.2 Model based Controllers

Model-based controllers gather information on the desired response from a model and generate the control output. In this section, Model-based Fuzzy controller (MBF controllers) and model-based sliding mode controllers (MBSM controller) are presented within the model-based controller category. The MBF controller generates output based on the displacement response and relative displacement response of the oscillating component, while the MBSM controller monitors the model's desired response to generate output. The following section elucidate more information about these controllers.

6.2.1   Model based Fuzzy controller

Developing an appropriate control strategy is very critical for using MRE isolator real-life applications. Researchers in the past have reported on the MRE isolator based on on-off (Du et al. 2011) and model-free fuzzy controller (Nguyen et al. 2017a). These controllers are model free and easy to implement. However, the above-mentioned controller has an inherent disadvantage that it generates control output for all frequencies, which is not essential and the controllers are not adaptive to the change of amplitude of excitation. To address these shortcomings, the current research is focused on the development of a MBF controller for vibration isolation. The developed viscoelastic state space model was utilised to halt the fuzzy controller's control output when the excitation frequency exceeded the CS frequency. This is accomplished by comparing the passive viscoelastic state space model response of the MRE isolator $\ddot{x}_{I_0}$, with the response from active viscoelastic state space model response $\ddot{x}_I$. The condition for enabling or disabling the fuzzy controller is given below

$$
Fuzzy = \begin{cases} \ddot{x}_{I_0} \leq \ddot{x}_I & 0 \\ \ddot{x}_{I_0} > \ddot{x}_I & 1 \end{cases} \tag{6.1}
$$

where, 0 and 1 denote the fuzzy controller, which receives the off and on command respectively.

    Fuzzy sets serve as the basis for fuzzy logic controllers. Because it does not need an exact model of the system to be controlled, it is the most often used controller. Fuzzy logic operates by executing rules that link the controller's inputs to the desired outputs. Typically, these rules are derived from the designer's intuition or understanding of the regulated system's functioning.
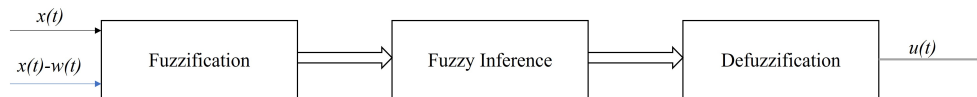
Figure 6.1: Block diagram of the Fuzzy controller

    A fuzzy controller generates the required output in three steps: fuzzification, fuzzy inference, and defuzzification. Figure 6.1 depicts the series of operations that uses the steps to produce output. The following section illustrates a detailed description of each

process.
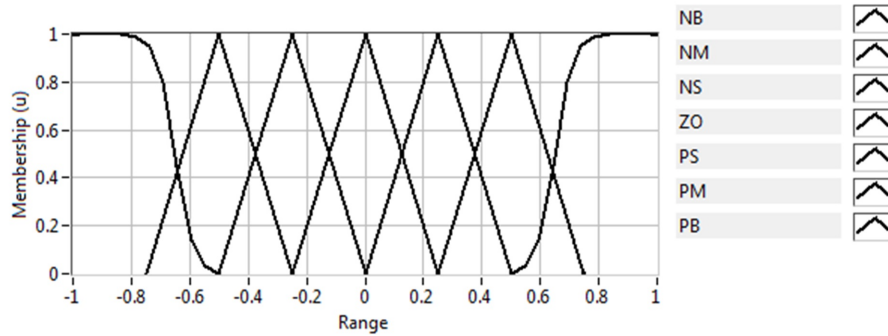
Figure 6.2: Triangular and sigmoidal membership function of $x(t)$, $(x(t) - w(t))$ and $u(t)$

Fuzzification

In this phase, the displacement response $x(t)$, relative displacement response $(x(t) - w(t))$ and controller output $u(t)$ signals are scaled for unity for better differentiation. The fuzzy controller initially converts both the continuous numerical signal into linguistic variables. The linguistic variables named as positive big (PB), positive medium (PM), positive small (PS), zero (ZO), negative small (NS), negative medium (NM), and negative big (NB). This process of conversion is called Fuzzification. The range of each linguistic variable for input and output variables are depicted in Figure 6.2, and for each linguistic variable, a specific membership function (Triangular membership or sigmoidal membership function) is assigned. The detailed mathematical information about triangular and sigmoidal membership functions are provided in the subsection. The designation of membership functions of displacement and relative displacement are $\mu_{x(t)}(d)$ and $\mu_{x(t)-w(t)}(r)$ for the fuzzy set of $x(t)$ and $(x(t) - w(t))$, and the output membership is $\mu_{u(t)}(i)$ for the fuzzy set $u(t)$

Triangular membership

The triangular membership is defined for NM, NS, ZO, PS and PM of the input and output signals. If a, b and c represent the lower, centre, upper boundary of the input and output signal then the membership function $\mu_{x(t)}(d)$, $\mu_{x(t)-w(t)}(r)$ and $\mu_{u(t)}(i)$ mathematically represent as (Zhao and Bose 2002) .

116

$$\mu_{x(t)}(d) = \begin{cases} 0 & \text{if } d \leq a \\ \frac{d-a}{b-a} & \text{if } a \leq d \leq b \\ \frac{c-d}{c-b} & \text{if } b \leq d \leq c \\ 0 & \text{if } d \leq c \end{cases} \qquad (6.2)$$

$$\mu_{x(t)-w(t)}(r) = \begin{cases} 0 & \text{if } r \leq a \\ \frac{r-a}{b-a} & \text{if } a \leq r \leq b \\ \frac{c-r}{c-b} & \text{if } b \leq r \leq c \\ 0 & \text{if } r \leq c \end{cases} \qquad (6.3)$$

$$\mu_{u(t)}(i) = \begin{cases} 0 & \text{if } i \leq a \\ \frac{i-a}{b-a} & \text{if } a \leq i \leq b \\ \frac{c-i}{c-b} & \text{if } b \leq i \leq c \\ 0 & \text{if } i \leq c \end{cases} \qquad (6.4)$$

where, d, r and i are the universe of discourse of the triangular membership function for the $x(t)$, $(x(t) - w(t))$ and $u(t)$ fuzzy set

Sigmoidal membership function

The sigmoidal membership function is defined for input and output signal linguistic variables NB and PB. The selected sigmoidal membership will improve the control processing and stability of the controller. This member function has an exponential function that depends on two parameters. The sigmoidal membership function is mathematically defined as (Zhao and Bose 2002).

$$\mu_{x(t)}(d) = \frac{1}{1 + e^{-a(d-c)}} \qquad (6.5)$$

$$\mu_{x(t)-w(t)}(r) = \frac{1}{1 + e^{-a(r-c)}} \qquad (6.6)$$

$$\mu_{u(t)}(i) = \frac{1}{1 + e^{-a(i-c)}} \qquad (6.7)$$

where, d, r and i are the universe of discourse of the sigmoidal membership function for the $x(t)$, $(x(t) - w(t))$ and $u(t)$ fuzzy set.

The fuzzy inference

After Fuzzification, the next phase is the fuzzy inference, where in the present study Mamdani fuzzy inference (Mamdani and Assilian 1975) method is considered. This inference contains 49 rules (Table 6.1) on linguistic variables based on the on-off control algorithm. Based Mamdani fuzzy inference, fuzzy operation OR (OR = max) on two fuzzy input membership functions.

Table 6.1: List of rules used in the fuzzy controller

		Relative Displacement						
		PB	PM	PS	ZO	NS	NM	NB
	PB	NB	NB	NB	NB	ZO	ZO	ZO
	PM	NM	NM	NM	NM	ZO	ZO	ZO
	PS	NS	NS	NS	NS	ZO	ZO	ZO
Displacement	ZO	ZO	ZO	ZO	ZO	ZO	ZO	ZO
	NS	ZO	ZO	ZO	PS	PS	PS	PS
	NM	ZO	ZO	ZO	PM	PM	PM	PM
	NB	ZO	ZO	ZO	PB	PB	PB	PB

Then, the maximum value of for the membership the function $\mu_{u(t)}(d)$ and $\mu_{(x(t)-w(t))}(r)$

$$\mu_{D \cup R}(dr) = max(\mu_{u(t)}(d), \mu_{(x(t)-w(t))}(r)) \qquad (6.8)$$

Apply implication method (min)

$$sat\left(\mu_{u(t)}(i)\right) = \begin{cases} 0 & \text{if } \mu_{u(t)}(i) = 0 \\ \mu_{u(t)}(i) & \text{if } 0 < \mu_{u(t)}(i) < \mu_{D \cup R}(dr) \\ \mu_{D \cup R}(dr) & \text{if } \mu_{u(t)}(i) \geq \mu_{D \cup R}(dr) \end{cases} \qquad (6.9)$$

Apply aggregation method for 49 rules (max)

$$\mu_{u(t)_{sum}}(i) = \sum_{j=1}^{49} sat\left(\mu_{u(t)}(i)\right)_j \qquad (6.10)$$

Defuzzification

The last phase of the operation is performed to produce the required current for controlling the system stiffness. This process is called Defuzzification. In this process, the centre-of-gravity method is adapted to compute the output driving current I. The calculated output of the fuzzy is scaled to the required value and supplied to the MRE isolator. The mathematical expression to represent the fuzzy output calculated from the centre of gravity (COG) / centroid of area (COA) method is (Hellendoorn and Thomas 1993),

$$I = \frac{\sum_{j=1}^{n} i_j . \mu_{u(t)_{sum}}(i)_j}{\sum_{j=1}^{n} \mu_{u(t)_{sum}}(i)_j} \tag{6.11}$$

where, n represents the number of elements of membership function $\mu_{u(t)_{sum}}$.
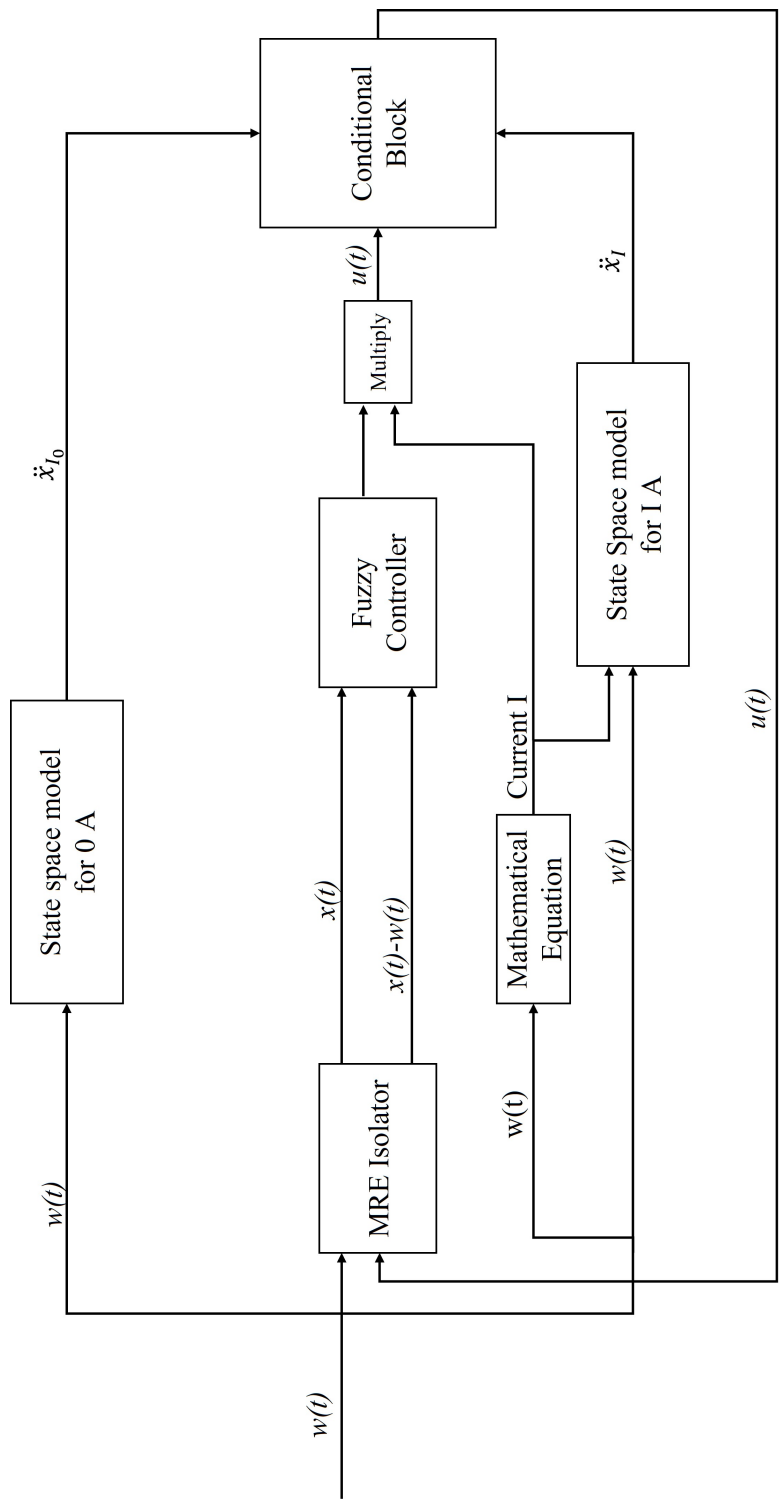
Figure 6.3: Block diagram of the MBF control scheme

The block diagram depicts the process of generating control input $u(t)$ to the MRE isolator using MBF controller (Figure 6.3). The MRE isolator and two state-space models 0 A and I A are fed with the excitation signal input $w(t)$. For the given excitation, the response generated from system and models are $x(t)$, $\ddot{x}_0$ and $\ddot{x}_I$. For generating response $\ddot{x}_I$, the current I in the state space model is estimated using Equation 5.34 based on the given amplitude of excitation signal. The fuzzy controller receives the $x(t)$ and $x(t) - w(t)$ responses from the MRE isolator and generates a unit control output signal $u(t)$. This signal is multiplied by current input I to obtain the required value for scaling the control output. Based on the condition block (Equation 6.1), the fuzzy controller output is sent to the MRE isolator.

6.2.2 Model Based sliding mode controller

Sliding mode controller is an error-based controller that produces control output depending on desired value. The desired value is a vital information for the controller and can be estimated using the system's known mathematical model. Since the sliding mode controller is robust, and efficient for nonlinear systems, it can withstand parametric uncertainties and external disturbances. The controller is most suitable for MRE isolators.

Two steps are involved in the design of a sliding mode controller (Liu and Wang 2011). The first step is to mathematically define the sliding surface so that the MRE isolator can be confined over it in order to get the appropriate system response. The second step is to calculate the expression for switched feedback gains needed to move state trajectory of the plant to the sliding surface. Finally, using the Lyapunov stability theory, the developed controller is proved to be stable.

The sliding surface variable s defined as (Liu and Wang 2011)

$$s(x) = c^T x = \sum_{i=1}^{n} c_i x_i = \sum_{i=1}^{n} c_i x_i + x_n \tag{6.12}$$

where, x is the state vector, the slope of the sliding surface $c = \begin{bmatrix} c_1 & c_2 & ..... & c_{n-1} \end{bmatrix}^T$

In sliding mode control, parameters $c_1 c_2 ...... c_{n-1}$ should be selected so that Equation 6.12 satisfying Hurwitz condition.

121

For second-order system, design sliding mode function as

$$s = \dot{e} + c_1 e, \ where \ c_1 > 0 \qquad (6.13)$$

Now let the desired output be x_d then the error e and error rate $\dot{e}$ will be

$$e = \ x_d(t) - x(t) \quad \dot{e} = \ \dot{x}_d(t) - \dot{x}(t) \qquad (6.14)$$
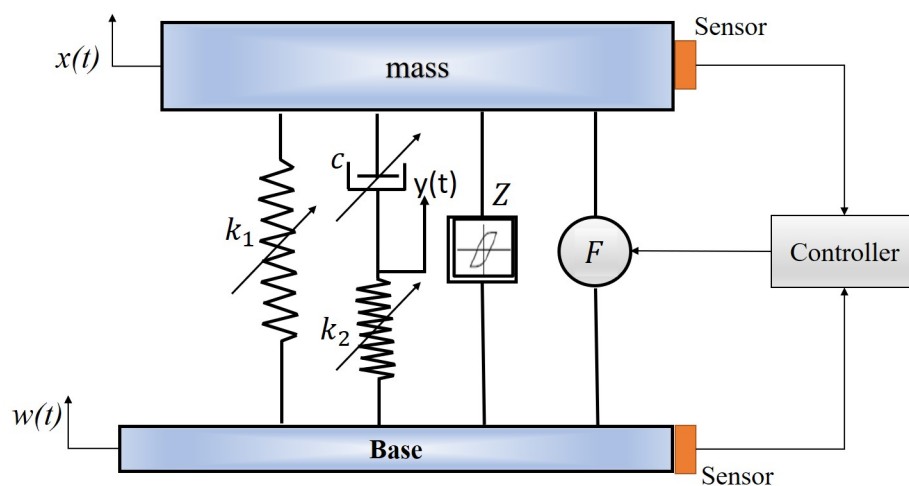
Figure 6.4: SDOF of the MRE isolator

For control application, the MRE based semi-active isolator with inclusion of sliding mode controller is shown Figure 6.4. The control output $F(t)$ from sliding mode controller is added to model in order to produce desired output.

The governing equation of system is

$$m\ddot{x}(t) + (k_1)(x(t) - w(t)) + (c)(\dot{x}(t) - \dot{y}(t)) + z(t) + F(t) = 0 \qquad (6.15)$$

$$(k_2)(y(t) - w(t)) = (c)(\dot{x}(t) - \dot{y}(t)) \qquad (6.16)$$

where, Z is hysteretic force. The Bouc-Wen element of the model is represented as,

$$\dot{z}(t) = \alpha(\dot{x}(t) - \dot{w}(t)) - \beta|\dot{x}(t) - \dot{w}(t)|z(t) - \gamma|z(t)|(\dot{x}(t) - \dot{w}(t)) \qquad (6.17)$$

where, α, β and γ are non-dimensional parameters responsible for the shape and size of the hysteretic loops. The system viscoelastic parameters are altered by varying the applied current and excitation amplitude.

122

Equation 6.15 is rewritten as

$$\ddot{x}(t) = -\frac{1}{m}\left(k_1\left(x\left(t\right) - w\left(t\right)\right) + c\left(\dot{x}\left(t\right) - \dot{y}\left(t\right)\right) + z(t) + F(t)\right) \tag{6.18}$$

Let

$$f(t) = k_1\left(x\left(t\right) - w\left(t\right)\right) + c\left(\dot{x}\left(t\right) - \dot{y}\left(t\right)\right) + z(t) \tag{6.19}$$

then $\ddot{x}(t)$ will be

$$\ddot{x}(t) = -\frac{1}{m}\left(f(t) + F(t)\right) \tag{6.20}$$

Lyapunov function as

$$V = \frac{1}{2}s^2 \tag{6.21}$$

The derivative of the s variable written as

$$\dot{s} = \ddot{e} + c_1\dot{e} = -\frac{1}{m}\left(f(t) + F(t)\right) + \dot{x}_d(t) + c_1\dot{e} \tag{6.22}$$

To guaranty stability, $\dot{V} \le 0$ Then,

$$\dot{V} = s\dot{s} = s\left(-\frac{1}{m}\left(f(t) + F(t)\right) + \dot{x}_d(t) + c_1\dot{e}\right) = -\eta\, sgn(s) \le 0 \tag{6.23}$$

With known $f(t)$, the desired control force is

$$F(t) = m\left(\ddot{x}_d + \eta.sgn\left(s\right) + c_1\dot{e}\right) - f(t) \tag{6.24}$$

With the known desired response $\ddot{x}_d$ from the viscoelastic model, the sliding model uses single gains of η and c_1 to track the desired response with the generated controller input to the MRE isolator.
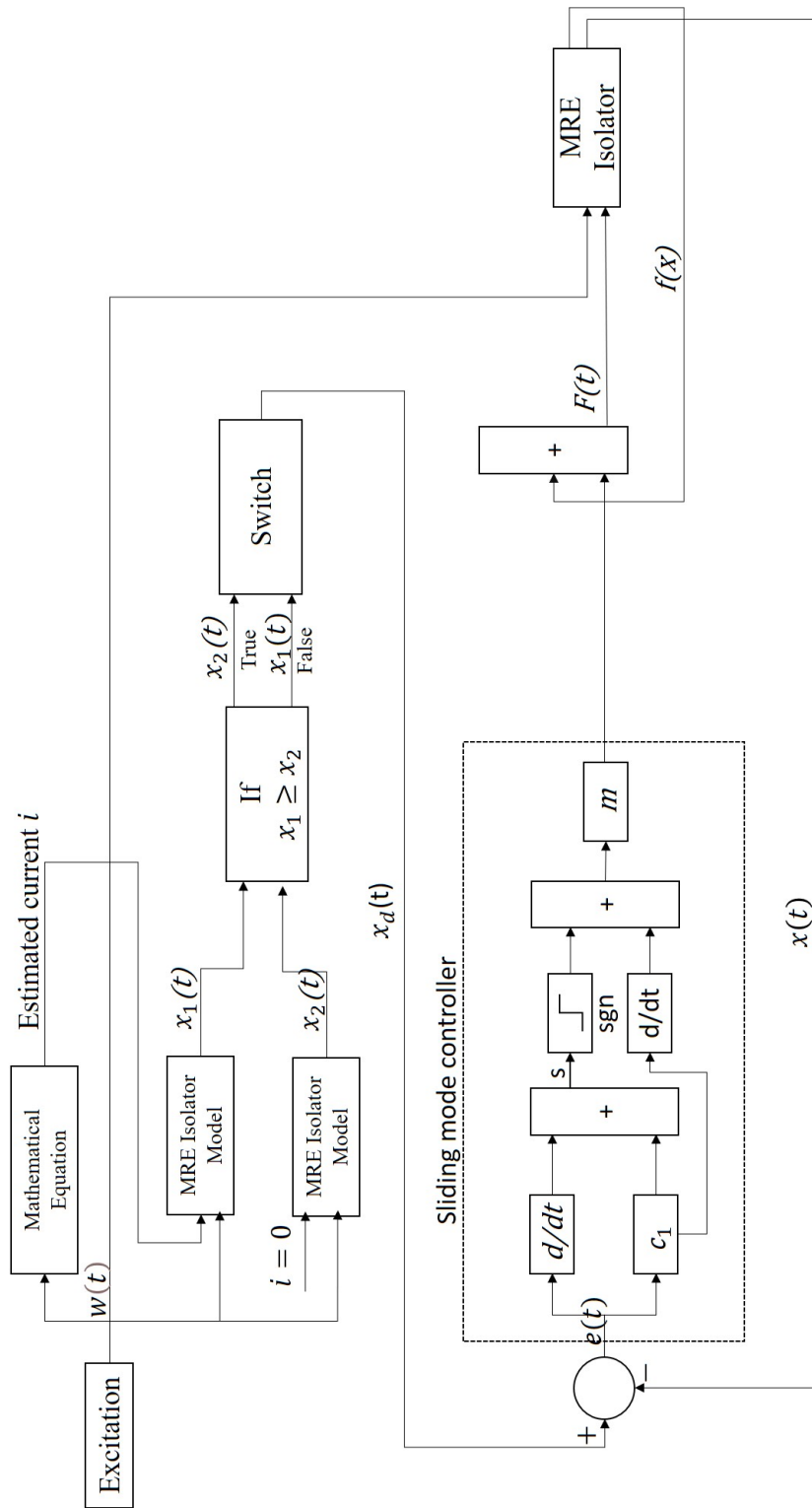
Figure 6.5: Block diagram of the MBSM controller

The process of estimating the control input to MRE isolator using MBSM controller is depicted in Figure 6.5. The MRE isolator and Isolator mathematical models are fed with the excitation signal input $w(t)$. For the given excitation, the response generates from the system and models are $x(t)$, $x_1(t)$ and $x_2(t)$. For generating the response $x_1(t)$, the current I in the isolator model is estimated using Equation 5.34 based on the given amplitude of the excitation signal. Depending on the error input, the MBSM controller generates control output $F(t)$, feeds into the isolator and tracks the desired response $x_d(t)$ for the selected gains. The desired response $x_d(t)$, a reference to the controller, is generated based on the control condition shown in the block diagram.
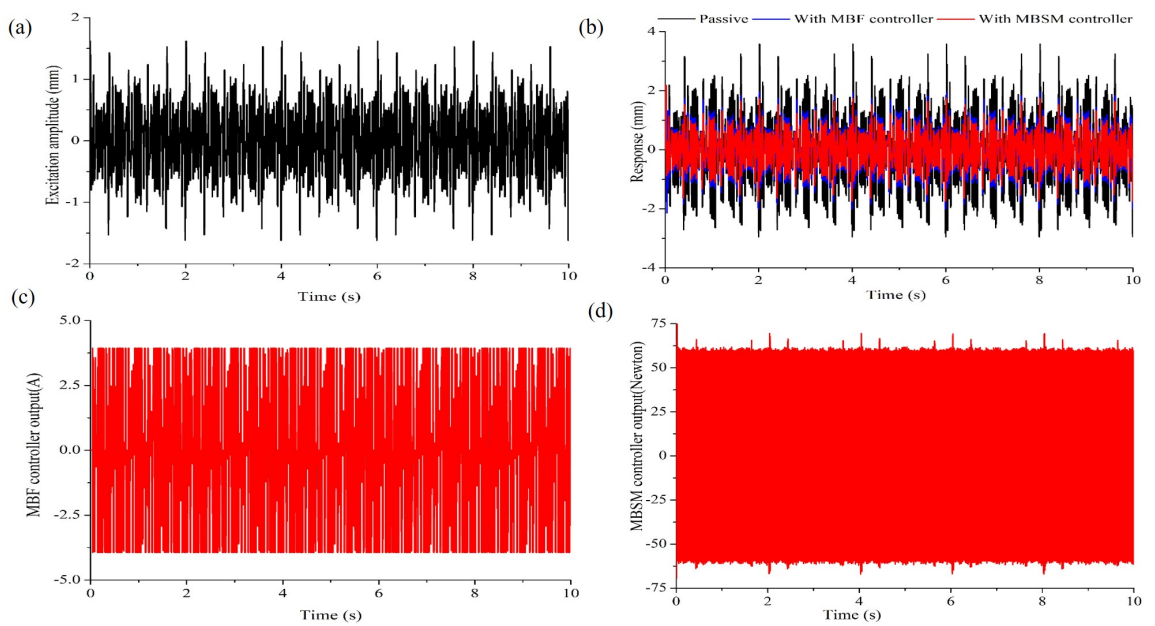
Figure 6.6: (a) Input Excitation to MRE isolator (b) Response of the MRE isolator (c) Control output from the MBF controller (d) Control output from the MBSM controller

6.2.3 Performance assessment of the model-based controller under Multi amplitude and frequency sine excitation

To check the adaptability and compared the isolation performance of the MBF and MBSM controllers, MRE isolator excited with Multi amplitude and frequency sine excitation input under simulated conditions. The input excitation contains the different combination of amplitudes (1.25 mm, 1.5 mm, 1.75 mm, 2 mm and 2.25 mm) and frequencies (15 Hz, 17.5 Hz, 25 Hz, 28 Hz and 30 Hz). The selected frequencies in the sine excitation are chosen in such way that all frequencies lie near or above the reso-

nance frequency of the passive system. The mathematical expression for averaged sine excitation is given below.

$$w(t) = \frac{\begin{aligned}1.25sin(2\pi 28t) + 1.5sin(2\pi 15) + 1.75sin(2\pi 25t) \\ + 2sin(2\pi 17.5t) + 2.25sin(2\pi 30t)\end{aligned}}{5} \qquad (6.25)$$

With the given input excitation (Figure 6.6 (a)), the comparison between the passive and control response of the system is shown in Figure 6.6(b).

The MBF controller produces the control output (Figure 6.6(c)) with the given inputs of displacement response $x(t)$ and relative displacement response $(x(t) - w(t))$. The MBF controller control output which is varying from 3.94 A to -3.94 A (Figure 6.6 (c)) . This controller output from the controller input to the MRE isolator that produces the response contains transient behavior which exists up to 48 ms and then it reaches steady state. The isolation achieved in the receiver in comparison with passive with the implementation of the MBF controller is 41.39%.

For the chosen gains $c_1 = 150$ and $\eta = 50$, MBSM controller produces the control output (Figure 6.6(d)) with the given error signal $e(t)$. The MSM controller produces the control output ranges from 61 N to -61 N, as shown in Figure 6.6 (d). The MBSM controller output from the controller input to the MRE isolator that produces the response contains transient behavior which exists up to 28 ms and then it reaches steady state. The isolation achieved in the receiver in comparison with passive with the implementation of the MBF controller is 49.19%.

In comparison, with the implementation of MBSM controller, the transient response reaches 20 ms earlier than the transient response achieved using MBF controller. The RMS value of the passive response of the MRE isolator is 1.20 mm. In contrast, the RMS value of the response with the MBF and MBSM controllers is 0.07 mm and 0.06 mm, respectively. The isolation capability with using MBSM controller is 7.9% lesser than the MBF controller. The numerical comparison between the MBF controller and the MBSM controller concludes that the MBSM controller performs better in isolating vibrations in the receiver and the system response reaches a steady state much earlier than the MBF controller. Although the MBSM controller is superior than the MBF controller, the implementation of the MBSM controller results in jerks in the inertial mass because the control output from the controller comprises a pulse-like signal as

compared to the continuous fluctuation in current the MBF controller outputs.

6.3   Model Free radial basis neural network function sliding mode controllers (RBSM controller)

Making a mathematical model for an MRE isolator is a time-consuming process that requires a large number of experimental tests under various conditions, as well as parametric optimization for estimating viscoelastic model parameters. In this section, if the desired response of the $\ddot{x}_d$ in the Equation 6.24 in unknown then controlling method using sliding mode controller without using mathematical model is explained. The radial basis neural network is added to sliding mode controller in order to achieve desired response $\ddot{x}_d$ using sliding mode controller. The neural network adjusts the values of $f(t)$ the Equation 6.24 in such way that the desired response $\ddot{x}_d$ is achieved using sliding mode controller. The adjustment $f(t)$ usually done through the change of weights in the neural network. The controller is particularly useful when system is operating in limited range of frequencies and amplitudes.
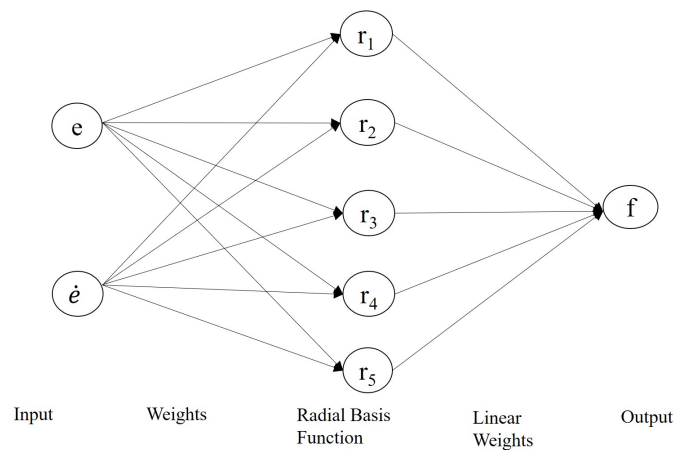
Figure 6.7: The architecture of a radial basis function neural network.

6.3.1   Radial basis neural network function)

Neural networks are made up of neuron clouds analogous to human brain nerve cells and primary objective of the nerve cell is to communicate and process information from our senses. The output is created using the trained neural network's activation function and the provided input. The multilayer perceptron (MLP) is a form of feedforward neural

127

network. MLP neural networks have several layers, and the convergence of optimisation targets is much slower than in radial basis neural networks because they only have one hidden layer (Jayawardena et al. 1996). Despite having only one layer, the RBFNN has been shown to be a universal approximation. The RBFNN has a few applications, including function approximation, interpolation, classification, and time series prediction (Wu et al. 2012). The RBFNN is a feed-forward neural network with three layers: input, hidden, and output (Park and Sandberg 1991). Figure 6.7. depicts the usual architecture of the RBFNN. The input layer is a vector, while the hidden layer is made up of n neurons. The radial basis function activates each neuron in the buried layer, which has weights and biases. The weight vector has the same dimension as the input vector.

The Euclidean distance between the weight vector wi and the input vector xi is defined by $||xi\,(t) - wi_j(t)||$

The activation function of the neural network is (Park and Sandberg 1991)

$$H_j = exp\left(-\frac{||xi\,(t) - wi_j(t)||^2}{2\Omega}\right) \qquad (6.26)$$

where, Ω a positive scalar value and j is the number of neurons in the hidden layer. The neural network to approximate f will be

$$f(t) = W^T h\,(x) + \epsilon \qquad (6.27)$$

where, ε is the approximation error of the neural network; $h\,(x)$ The Gaussian function of the neural network; W ideal neural network weights with the variations in viscoelastic model parameters for the input $xi = [e\ \dot{e}]$, neural network to output $\widehat{f}\,(t)$ will be

$$\widehat{f}\,(t) = \widehat{W}^T h\,(x) \qquad (6.28)$$

The desired control force is

$$F(t) = m\,(\ddot{x}_d + \eta.sgn\,(s) + c_1\dot{e}) - \widehat{f(t)} \qquad (6.29)$$

Then, the derivative of s variable is

$$\dot{s} = -\frac{1}{m}\left(f(t) + m\left(\ddot{x}_d + \eta.sgn\left(s\right) + c_1\dot{e}\right) - \widehat{f(t)}\right) + \dot{x}_d\left(t\right) + c_1\dot{e} = -\frac{1}{m}\left(\widetilde{f}(t)\right) + \left(\eta.sgn\left(s\right)\right)$$

(6.30)

where

$$\widetilde{f}(t) = f(t) - \widehat{f}\left(t\right) = W^T h\left(x\right) + \epsilon - \widehat{W}^T h\left(x\right) = \widetilde{W}^T h\left(x\right) + \epsilon$$

(6.31)

and $\widetilde{W} = W - \widehat{W}$

The Lyapunov function defined for the RBSM controller as

$$V = \frac{1}{2}s^2 + \frac{1}{2}\gamma\widetilde{W}^T\widetilde{W}$$

(6.32)

The derivative of V

$$\dot{V} = -\widetilde{W}^T\left(\gamma\dot{\widehat{W}} + \frac{1}{m} sh\left(x\right)\right) - s\left(\epsilon + \left(\eta.sgn\left(s\right)\right)\right)$$

(6.33)

To guaranty stability, $\dot{V} \le 0$

Then $\dot{V} = -\widetilde{W}^T\left(\gamma\dot{\widehat{W}} + \frac{1}{m} sh\left(x\right)\right) - s\left(\epsilon\right) - \eta\left|s\right| \le 0$

Due to the approximation error, ε is limited and sufficiently small. To achieve $\dot{V} \le 0$, the design of the controller should be $\eta \ge \epsilon$, so that $-\widetilde{W}^T\left(\gamma\dot{\widehat{W}} + \frac{1}{m} sh\left(x\right)\right) = 0$

The adaptive law of the neural network is

$$\dot{\widehat{W}} = -\frac{1}{m}\frac{1}{\gamma} s\, h(x)$$

(6.34)

Equation 6.34 calculates estimated adaptive weights of the neural network. In Equation 6.28, these weights are replaced to approximate the unknown resistive force $f(t)$. This $f(t)$ is added to the sliding mode controller output to accomplish the MRE isolator's required control performance. The chattering component $(sgn(s))$ in the Equation 6.24 is minimized with the inclusion of by the neural network component force in the equation.
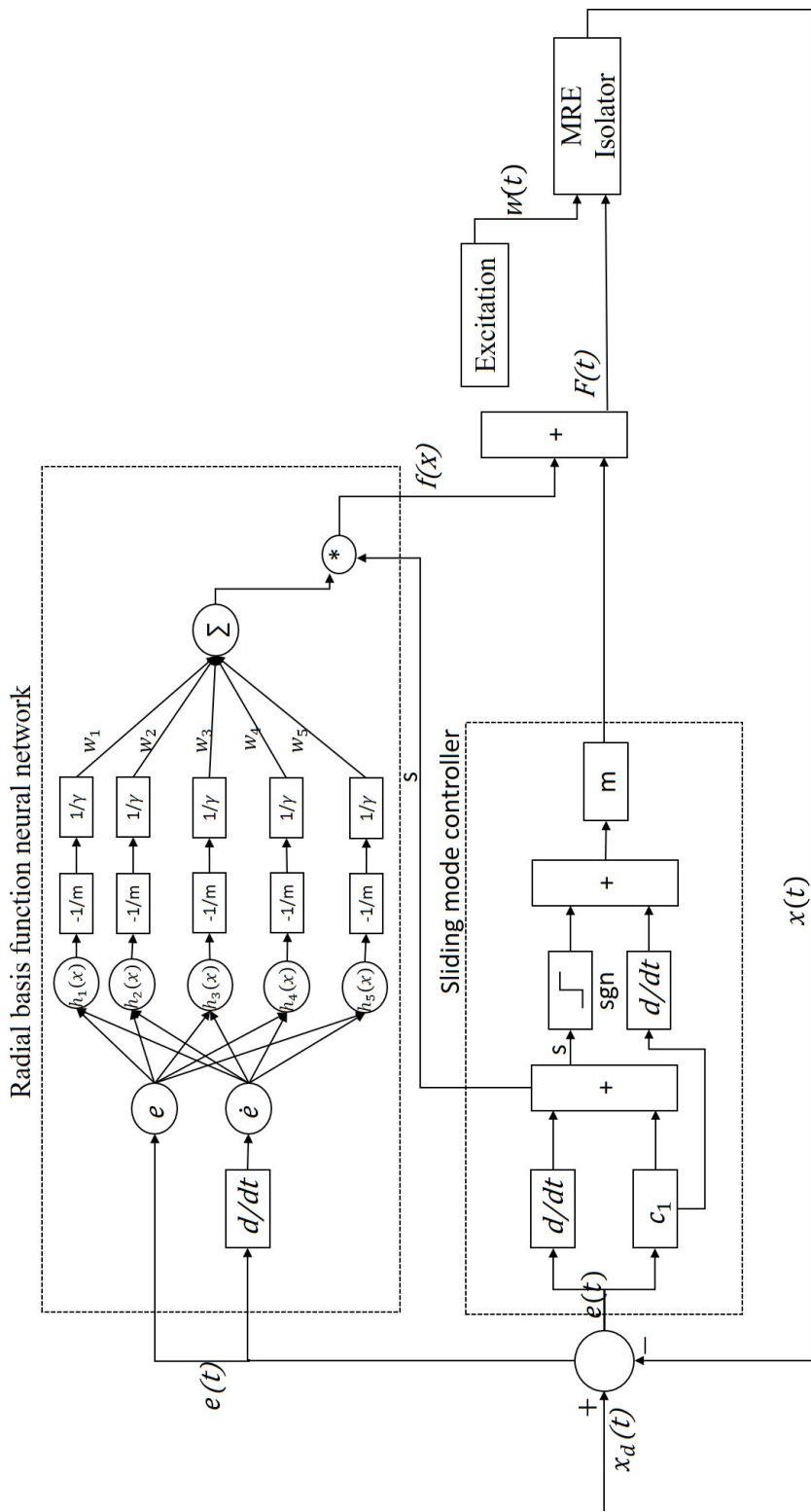
Figure 6.8: Block diagram of the RBSM control scheme

Figure [6.8](#) depicts a block diagram of an RBSF controller. The MRE isolator is excited by the excitation $w(t)$ and generates response $x(t)$. The error signal $e(t)$, the difference between the desired $x_d(t)$ and $x(t)$ isolator response, is calculated and fed to the sliding mode control and neural network. The sliding mode controller generates the sliding surface $s(t)$ with the error and error rate signals. The adaptive rule uses a sliding surface and the Gaussian function $h(t)$ to evaluate neural network weights. The neural network adjusts the weights, and the property function $f(t)$ is computed. Finally, the control output of the sliding mode is added to the property function $f(t)$, and the control output $F(t)$ is sent to the MRE isolator.

6.3.2 Performance assessment in simulation

In this section, RBSM controller implemented on the MRE isolator in simulation is measured under the excitation of a single sine input with varying amplitude and frequency. The simulation amplitudes and frequencies were chosen based on the maximum isolation condition, which is at the natural frequency of the system and the CS frequency. A total of ten conditions were chosen for vibration control via controller. Five of the ten conditions were chosen at the natural frequency of the system, 28 Hz, with varying amplitudes of excitation ranging from 1.25 mm to 2.25 mm. The other five conditions are chosen at the CS frequency criteria, which are 39.5 Hz, 35.16 Hz, 34.52 Hz, 34.25 Hz, and 33.78 Hz. In each set of conditions, the neural network adjusts the weighting so that sliding mode controller produces desired output. For training the neural network, the data consists of inputs error and error rate and the property function $f(t)$ which is estimated from the performance results of sliding mode controller.

The performance of sliding mode controller is measured on the MRE isolator using single sinusoidal excitation at 28 Hz frequency with amplitudes of excitation of 1.25 mm, 1.50 mm, and 1.75 mm. Without taking into account the model, the implementation of sliding model control is considered. Because the desired response estimated from the mathematical model is unknown, it is assumed that the desire is zero for the sliding mode controller. The performance of the controller is now entirely dependent on the controller gains c and η. As shown in the Figure [6.9](#), the sliding mode controller is turned off for the first two seconds and then turned back on for the next two seconds. For the first set of amplitude and frequency of excitation, the sliding mode controller gains c_1 and η were
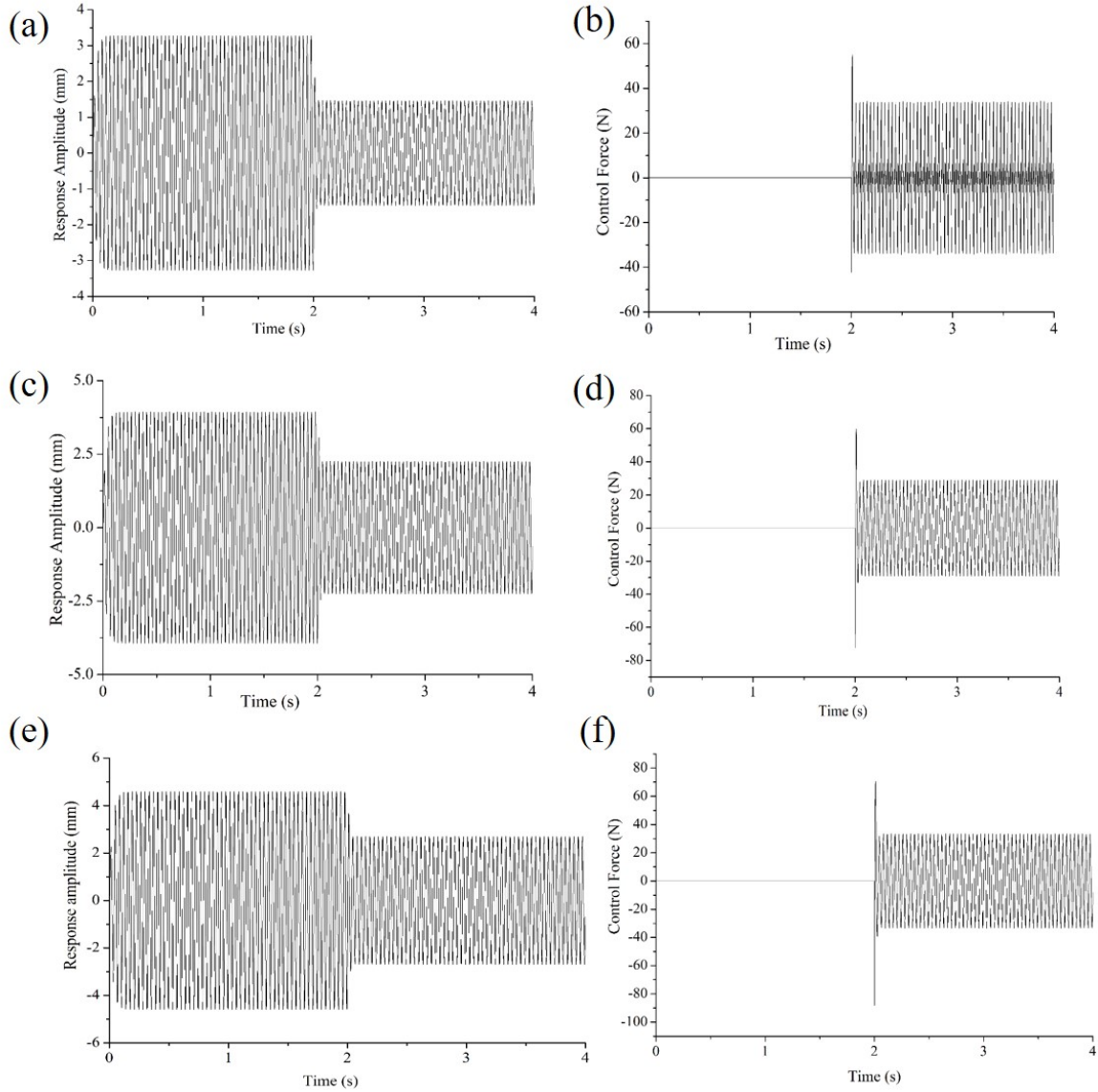
Figure 6.9: With the implementation of sliding mode controller (a) , (c) and (e) Response of the MRE isolator (b) , (d) and (f) Controller force generation under 1.25 mm, 1.50 mm, 1.75 mm,2 m and 2.25 mm amplitude of excitation at 28 Hz frequency

set to 15 and 35, respectively. With those gains, the controller generates control force (Figure 6.9(b)), which is fed into the MRE isolator to isolate the vibrations from the source by 55.8% (Figure 6.9(a)), as specified in the table. Similarly, for amplitudes of excitation of 1.50 mm and 1.75 mm, the controller gains c_1 and η were chosen to achieve the required isolation of 51.8% (Figure 6.9(c)) and 41.2% (Figure 6.9(e)), respectively, which is 15 and 8, and 8 and 3. The controller output force for those gains is shown in Figure 6.9(d) and Figure 6.9(f).

Based on the above controller performance analysis, it is concluded that in the absence of a mathematical model for the MRE isolator, the sliding mode controller gains

132

must be changed every time. As a result, in order to effectively implement a sliding mode controller over a wide frequency range, gains of the controller must be scheduled for each set of conditions. For that, an addition of radial basis neural network was chosen for controlling the vibration over a wide frequency range. The details of the controller performance of the RBSM controller are analyzed in the next section.

The performance of the RBSM controller was investigated at various excitation amplitudes and frequencies. A radial basis neural network was initially created for ten sets of conditions which is listed in table. The weight of the neural network is chosen in such a way that the sliding mode controller produces the required control output for the desired vibration isolation. The neural network automatically changes its weights as the amplitude of excitation changes, causing the controller output from the sliding mode controller to change and achieve required isolation.
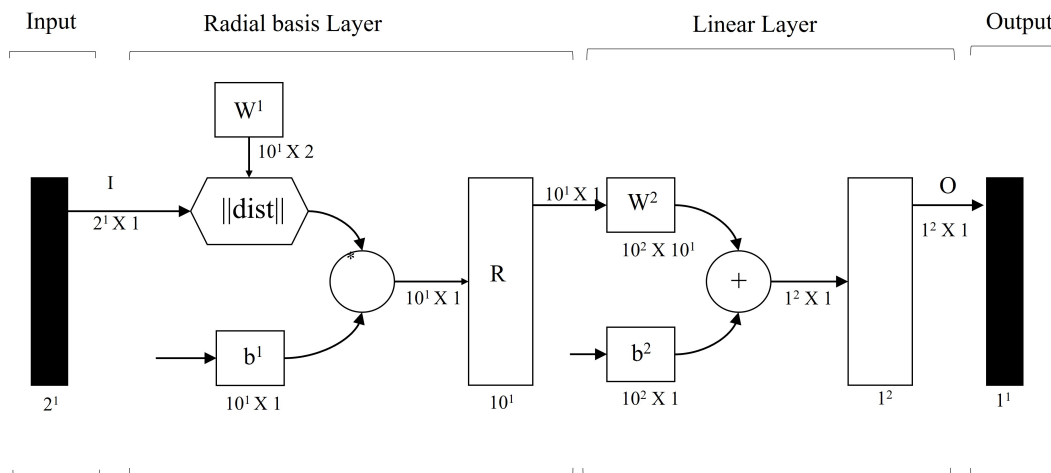
Figure 6.10: Radial basis neural network

The structure of a radial basis neural network is 2-10-1. (2 neuron input layer-10 neuron in the hidden layer-1 neuron in the output layer). Figure 6.10. depicts the evaluation process of neural network for a given input. 10 scenarios are studied, each with a different frequency and magnitude of excitation (Ten cases are listed in Table 6.2). Because the input vector size was 10, the hidden layer takes into account 10 neurons. The weight of linear layer and bias are selected so that only one neuron is engaged for each error and error rate input. To obtain the weights and biases of a neural network used in a RBSM controller, the unknown resistive force $f(t)$ for a given set of inputs (error and error rate) is determined manually for each set of conditions which are mentioned in Table 6.2. Then, for set of error and error rate input and output of the unknown resistive

force $f(t)$, the neural network is trained using the gradient descent method to obtain the weights and biases, which are used to estimate the resistive force $f(t)$ in the controller. The weights of neural network and biases are chosen as

$$W^1 = \begin{bmatrix} 0.00125 & 0.21991 \\ 0.00150 & 0.26389 \\ 0.00175 & 0.30787 \\ 0.00125 & 0.31023 \\ 0.00150 & 0.33137 \\ 0.00225 & 0.47755 \\ 0.00200 & 0.35185 \\ 0.00175 & 0.37956 \\ 0.00225 & 0.39584 \\ 0.00200 & 0.43039 \end{bmatrix} \quad b^1 = \begin{bmatrix} 0.83255 \\ 0.83255 \\ 0.83255 \\ 0.83255 \\ 0.83255 \\ 0.83255 \\ 0.83255 \\ 0.83255 \\ 0.83255 \\ 0.83255 \end{bmatrix} \quad W^2 = 10^{12} \begin{bmatrix} -1.469 \\ 4.154 \\ -4.823 \\ 1.187 \\ 0 \\ -1.552 \\ 3.680 \\ -5.163 \\ -9.782 \\ 4.966 \end{bmatrix}^T \quad b^2 = [260944770.7]$$

$$(6.35)$$

With the neural network weights chosen, the RBSM controller was implemented on the MRE isolator, with sliding mode gains c_1 and η set to 130 and 0.1, respectively. Because the controller gain η is 0.1, the controller output has no chattering effect. The amplitude of excitation (1.25 mm to 2.25 mm) to the MRE isolator changes every 4 second over a 20 second period, as shown in Figure 6.11 (c). Similarly, the frequency of sinusoidal excitation changes every 2 seconds over a 20 second period, as shown in Figure 6.11 (d). For each set of condition, the controller is turned off for 1 second before turning back on for the next second. The Figure 6.11(a) depicts the response of the MRE isolator for each set of conditions with and without controller input (Figure 6.11(b)) to the MRE isolator. The maximum vibration isolation (55.8%) occurs between 2 and 4 seconds, corresponding to an excitation amplitude of 1.25 mm and a frequency of 28 Hz.

Table 6.2: Performance characteristics of MRE isolator at different frequencies and amplitude

Frequency (Hz)	Excitation amplitude(mm)	Transmissibility (0 A)	Transmissibility (3 A)	Isolation (%)
28	1.25	2.47	1.09	55.8%
39.5	1.25	1.19	1.19	0 %
28	1.50	2.47	1.39	51.8%
35.16	1.50	1.68	1.68	0%
28	1.75	2.47	1.45	41.2%
34.52	1.75	1.77	1.77	0%
28	2	2.47	1.47	40.4%
34.25	2	1.81	1.81	0%
28	2.25	2.47	1.51	38.8%
33.78	2.25	1.88	1.88	0%
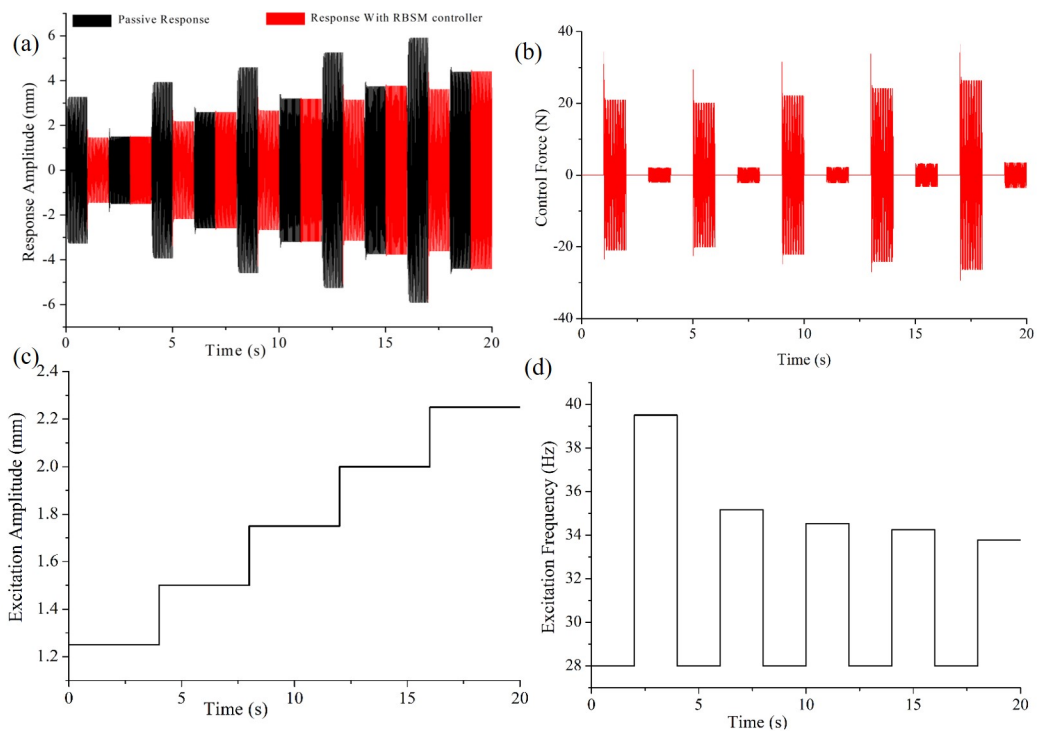
Figure 6.11: With the implementation of tuned RBSM controller (a) Response of MRE isolator with and without controller (b) Control Force of the controller (c) Variation of excitation amplitude with respect to time (d) Variation of excitation frequency with respect to time

The control force of the controller corresponds to the maximum isolation at 3 to 4 seconds. With the implementation of control, the isolation of vibration at natural frequency

of 28 Hz decreases from 55.8% to 38.8% as the amplitude of excitation increases from 1.25 mm to 2.25 mm, which is the desired performance from the controller. The implementation of a controller at the frequencies of excitation of 39.5 Hz, 35.16 Hz, 34.52 Hz, 34.25 Hz, and 33.78 Hz results in the least amount of vibration isolation (0%), as shown in the Figure 6.11(a). This is because at those frequencies, the system already achieves isolation without the need for any control input.
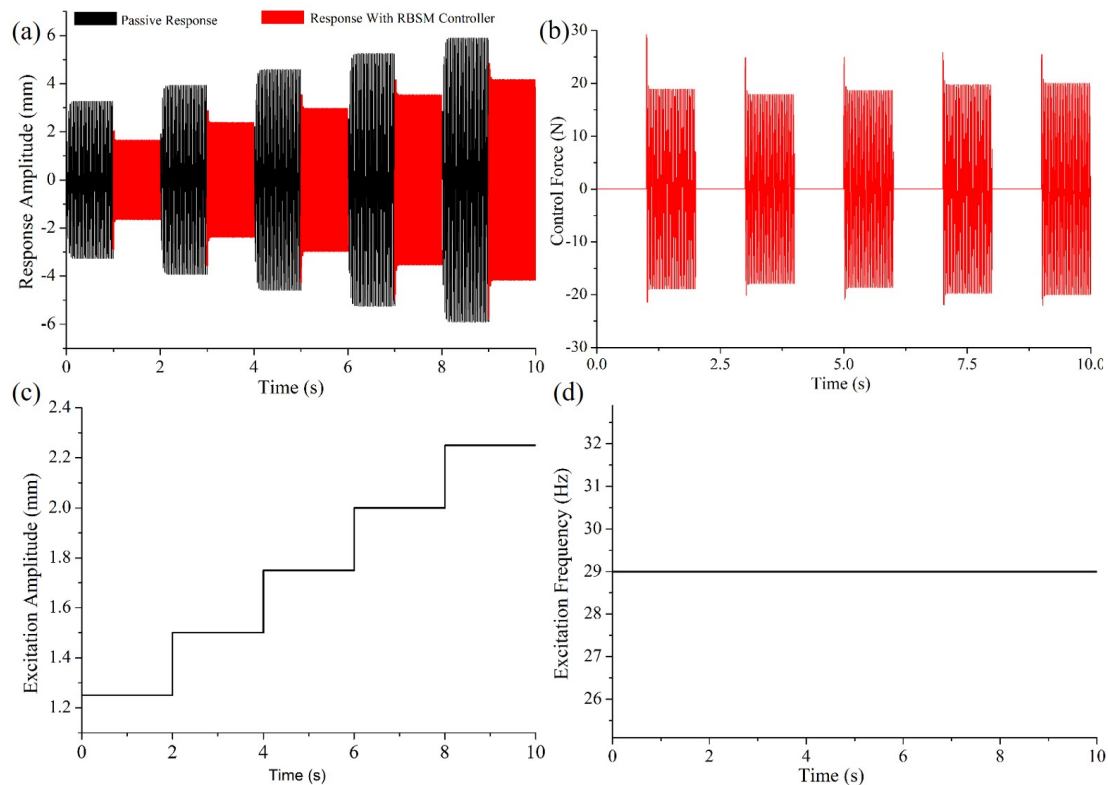
Figure 6.12: With the implementation of RBSM controller (a) Response of MRE isolator with and without controller (b) Control Force of the controller (c) variation of excitation amplitude with respect to time (d) variation of excitation frequency with respect to time

The current control performance analysis for the RBSM controller was only for a small set of excitation amplitudes and frequencies. Predicting performance in between frequencies required the use of additional set of data or additional neuron. To test the performance in between the frequencies, the predicted frequency and amplitudes must be closest to the chosen data in order to provide an accurate prediction. This is because the activation function under consideration is a radial basis function. Considering the facts, the excitation frequency of 29 Hz is chosen to predict the performance of the controller for different excitation amplitudes (1.25 mm to 2.25 mm). Figure 6.12(a) depicts the performance of the RBSM controller under these conditions. The excitation ampli-

tude changes every 2 seconds (Figure 6.12(c)), while the excitation frequency remains constant throughout the simulation (Figure 6.12(d)). The controller is turned off for 1 second and then turned back on for 1 second for each set of data (Figure 6.12(b)). According to the response plot (Figure 6.12(a)), it is confirmed that for different amplitude of excitation, the desired amount of isolation is achieved with the given control input to the MRE isolator (Figure 6.12).

6.4 Real-time implementation of the controller

In the implementation of a real-time controller, the microcontroller communicates with sensor components and actuator. These microcontrollers feature a CPU with a preset processing speed that switches on actuator components for the correct period of time without jittering. The micro-functionality of the controller is defined by the program that has been burnt into it. Various control parameters in the host program may affect the microcontroller's control output through serial interface connection. Following sections provides the experimental setup for implementing of controller real-time and results related to the controller.
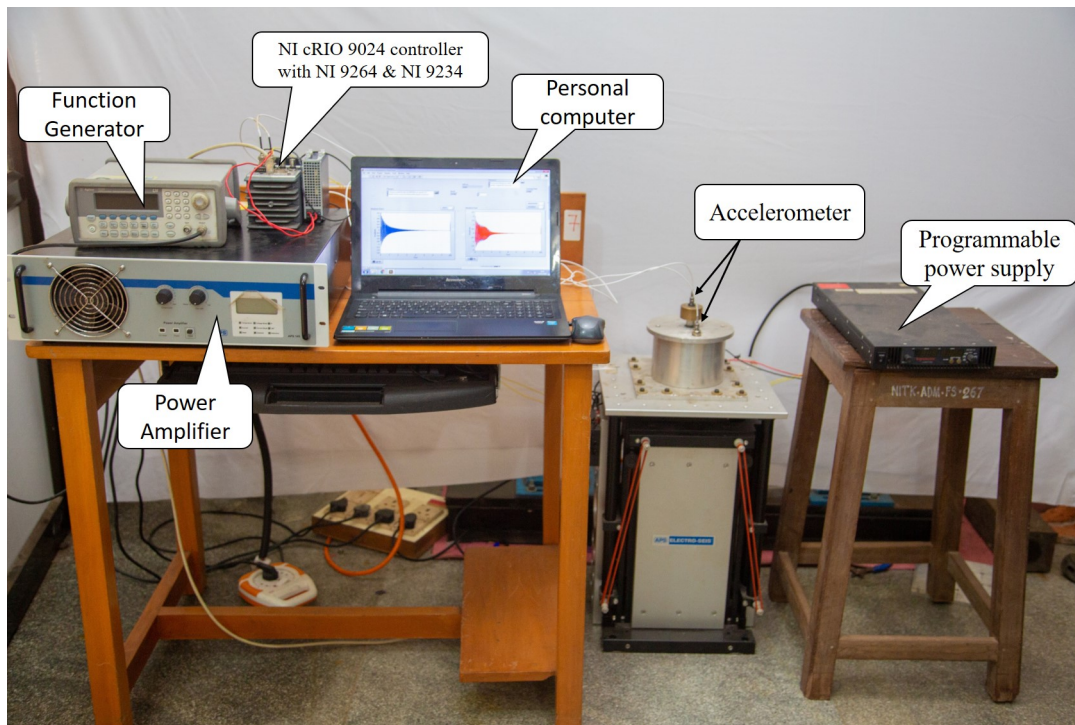
Figure 6.13: Experimental setup photograph for controlling vibration using MRE isolator.

6.4.1 Experimental set-up for real-time implementation

The performance of the MRE isolator during control implementation was investigated in real time. The experimental setup for measuring the performance of the MRE isolator is shown in Figure 6.13. The MRE isolator was mounted on the shaker table (Model: APS 420, APS DYNAMICS, INC). The real-time implementation control algorithm was implemented using an NI cRIO (Compact RIO Controller) -9024 embedded real-time controller. The function generator generates a sine sweep excitation signal with 2.5 V excitation amplitude for frequencies ranging from 15 Hz to 50 Hz. These signals were generated for a duration of 10 s, and its execution was controlled by using NI 9264 voltage output module. The generated sine sweep signal was fed into the amplifier and the amplified signal is received by the shaker. Two accelerometers (Model:8774A50, Kistler) were used, one mounted on the table and the other on the inertial mass to measure the input and output response respectively. The data from the sensors were collected using the NI 9234 DAQ module acquired through LabVIEW 2015.
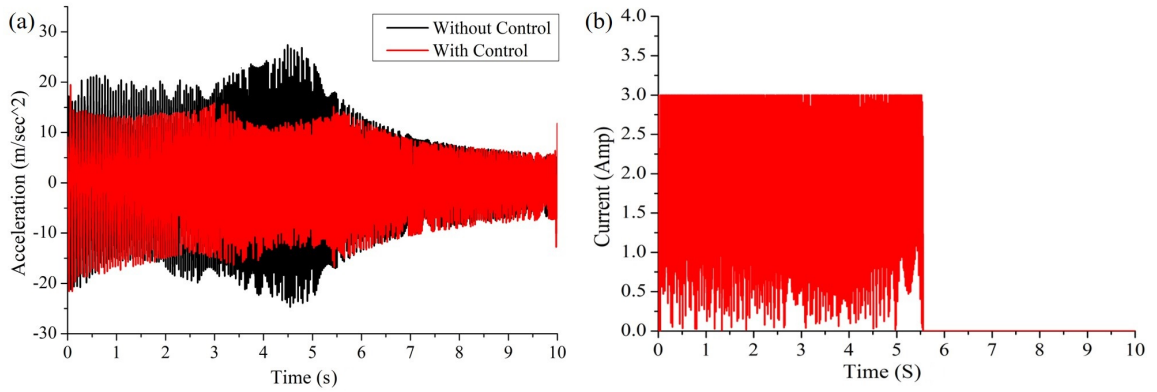
Figure 6.14: Plots of (a) Controlled and uncontrolled acceleration response; (b) controller output generates.

6.4.2 Performance assessment of the MBF controller Implementation

For real-time implementation of the controller for regulating vibrations at broad-bandwidth frequencies, the chosen controller must be robust and sensitive to frequency and amplitude changes. In addition to the features listed above, the controller must know when to stop itself when it enters the isolation area. As per understanding in the simulation of performance assessment, the implementation of the developed MBSM controller creates chattering (since the sgn function exists in the control output equation) in the response, and the developed RBSM controller works only for a limited frequency and amplitude. With the ready availability of fuzzy controller devices in the market and ease of implementation, the MBF controller was chosen for implementation in real-time in this study.

The response of MRE isolator without a controller for a given amplitude of excitation input is shown in Figure 6.14(a). Under passive state, the response of the MRE isolator generates a maximum acceleration of around 27.39 m/s^2. The controller calculates and produces controller output based on the given inputs such as acceleration response $\ddot{x}(t)$ and relative acceleration $(\ddot{x}(t) - \ddot{w}(t))$ response, which is shown in Figure 6.14.(b). The MBF controller output in Figure 6.14.(b) is about 3 A maximum and 0 A minimum. This control output from the controller is supplied to MRE isolator for vibration regulation in the inertial mass. With the given control signal, the system response reaches a steady state value of about 60 ms at the initial stage. It then starts isolating vibration in the receiving inertial member. This 60 ms delay in controlling the vibration is because of

139

the delay of activation of the electromagnet (Based on inductance and resistance of the coil) by about 24 ms and the delay in activating MRE element by 36 ms.

The maximum isolation of vibrations due to the controller in the inertial mass is about 55.55% at natural frequency. By analyzing the response of the MRE isolator, one can conclude that the controller effectively reduces vibration in the inertial mass up to 35 Hz, as evidenced by the control output signal, which stops at 5.5 s and then allows the system to operate passive state. During the controller off position, the time necessary for the MRE to revert back to its original state is zero milliseconds, since the active state of the MRE response has already reached its passive state. From control results, it is confirmed that the MBF controller is an effective control strategy and can be easily incorporated into MRE devices. This controller is adaptable and can be used to achieve wide frequency range isolation.

6.5 Conclusions

Model-based MBF controller and MBSM controller were developed for MRE isolator to regulate inertial mass vibrations. Under random excitation, the performance of both controllers was tested. The MBF controller works 8% less efficiently than the MBSM controller in isolating the vibration.

Apart from the model-based controller development, model free RBSM controller was also developed. The controller performance was evaluated for the different amplitude of excitation and frequency to check the adaptability. Simulation results conclude that the developed controller is efficient in regulating the vibration.

In practical application, The MBF controller was implemented in real-time. Results reveal that the developed controller was efficient in regulating vibrations in an inertial mass of 0.583 kg. Consequently, the objective of controlling vibration in PCB boards has been achieved.

Chapter 7

SUMMARY AND CONCLUSIONS

7.1 Summary of the current work

The aim of the current work is to design an MRE isolator for micron-level vibration control, especially for electronic circuit board. To implement an MRE isolator in real-word situation, the significant hurdle faced in developing the mathematical model for MRE isolator and control development is addressed in the current research.

A shear mode semi-active MRE isolator is designed to isolate vibration whose system natural frequency is around 30 Hz. The isotropic MRE is manufactured with weight ratio of 72% carbonyl iron, 16% silicone rubber, and 12% silicone oil. To magnetize the MRE element in the isolator, an electromagnet is designed. The magnetic circuit analysis and ANSYS MAXWELL software are used to calculate the magnetic field generation in the MRE and electromagnet.

A series of displacement transmissibility tests are performed on the MRE isolator at various current input and excitation amplitudes under sweep frequencies. The results show that MRE changes stiffness in a magnetic field, increasing overall natural frequency of the system. On the other hand, the change in stiffness decreases as the amplitude of excitation increases. This phenomenon is in-compliance with the Payne effect often observed in the particulate composite. The damping ratio of the MRE isolator increases with increasing current input but decreases with increasing excitation amplitude. This behaviour is observed in both passive and active states of the MRE isolator.

A viscoelastic model with Zener and Bouc-Wen elements is developed for the MRE isolator. The Zener element in the model is used to portray the viscoelastic properties of the MRE isolator. The Bouc-Wen element, on the other hand, is used to represent the

hysteresis behaviour of the MRE isolator. The state space approach is used to estimate model parameters. A linear second-order state-space equation is generated from non-linear experimental data using MATLAB system identification tool kit. Once the linear state space is determined, the unknown parameter values of the viscoelastic model are estimated by minimising the mean square error between the linear state space response and the model response. The function is optimized using gradient descent algorithm that is used in MATLAB optimization toolkit. Using the known model parameters with respect to current input, a polynomial equation is used to establish a relationship between the viscoelastic model parameter and the current input to the isolator. This state-space approach of modelling reduces the number of experiments required to develop the mathematical model for the MRE isolator over a wide frequency range. The parameters values of the model for the different excitation amplitudes are estimated based on the CS frequency (CS frequency), which eventually reduced the amount of experimentation is required further, and the polynomial equation is used to establish the relationship between the current input to the isolator and the amplitude of excitation. This equation is used to predict parameter values of the model with respect to excitation amplitude.

For implementing MRE isolator actual system, Model-based controllers and model-free controller are developed for controlling the vibrations in the inertial member for wide frequencies. Model-based controllers are developed using the developed mathematical model. The MBF controller and MBSM controller are developed under model-based controller. Because the rules are based on an on-off controller, previously developed model free Fuzzy controllers produce control output even in the isolation region. To stop the controller in the isolation region, control condition is developed to control the output of the Fuzzy controller. A MBSM controller is developed in addition to the MBF controller to produce the desired response at the receiver end. The desired response signal of the MRE isolator is generated by the viscoelastic model, and the sliding mode controller is the main controller that tracks the desired response by providing control input to the MRE isolator. In simulation, the performance of both model-based controllers are compared under random excitation condition.

It is difficult to develop a mathematical model for a non-linear system. In the absence of model, it is not viable to utilise a sliding mode controller for the MRE isolator since its gains vary with each change in operating parameters. To run sliding mode control

with single gain, a radial basis neural network is added to the sliding mode controller which estimated the unknown force by adjusting the weights of the neural network. The simulation results show that the RBSM controller works properly at different magnitude of excitation and frequency. In the concluding phase of the study, a real-time implementation of the MBF controller was implemented on an MRE isolator for sine sweep excitation. The findings demonstrate that the proposed controller is capable of regulating the vibration of inertial mass across a broader frequency range.

7.2   CONCLUSIONS

A successful design of shear mode MRE isolator was made for regulating the vibration in the PCBS. With instalment of MRE isolator, the overall natural frequency of the system reduces to 30 Hz compared system without isolator where the natural frequency is in Khz. The new modified system works effectively in regulating vibration for higher frequencies. For lower frequencies which are correspond to amplification region in the transmissibility plot, the vibration was regulated using current input to the isolator.

The designed isolator performance test results concludes that MRE isolator changes stiffness under magnetic field and increases the overall natural frequency of the system. However, under passive and active conditions, the change in stiffness decreases as the amplitude of excitation increases which is due to Payne effect. Overall, the shift in the natural frequency and relative increase in stiffness due to Payne effect decreased from 21.07 Hz to 16.09 Hz and 190.09% to 154.78% with increasing the amplitude of excitation from 1.25 mm to 2.25 mm. The damping ratio in the passive MRE isolator and the active MRE isolator decreased with the increasing excitation amplitude; however, in comparison to the passive condition, the damping ratio in the active condition (Under 3 A current input) is higher by approximately 67% (Under 2.25 mm amplitude of excitation) . Because of this change in stiffness and damping properties with respect to the magnetic field and excitation amplitudes, the maximum isolation of vibration of about 74.12% is found at 2.25 mm excitation amplitude, and the minimum isolation of vibration of about 39.04% is found at 1.25 mm excitation amplitude under 3 A current input.

It is crucial for implementing the control that the response be represented by a mathematical expression. Modeling the behaviour of the isolator system using viscoelas-

tic principles is quite successful. The magnetic, amplitude-dependent viscoelastic responses were represented using a viscoelastic model including Zener and Bouc-Wen elements. This modelling technique requires the determination of parameter values relative to experimental data. Previous methods relied on parameter estimation to mimic the MRE response for a single frequency in time-domain. Although this is a tried and tested technique, it needs a greater quantity of experimental data. A strategy based on determining the parameters relative to simulating MRE response under sweep frequency is more favourable.

To identify model parameters corresponding to current input and amplitude of excitation in frequency domain, a novel technique based on the state space approach and the CS frequency was adopted in this study. The state space approach permits the identification of model parameters for a broad frequency range with respect to the input current, and the concept of CS frequency simplifies the identification of amplitude-dependent properties, thereby facilitating the overall development phase of isolator models. The simulation results indicate that the viscoelastic model developed using the aforementioned method predicts MRE response under magnetic field influence with a minimum of 86% accuracy and a maximum of 96.66% accuracy, and that it predicts the CS frequency to be identical to the experimentally measured value.

In the last phase of the study, both model-based and model-free controllers are produced. Under the field of model-based controllers, the fuzzy controller and sliding mode controller are created. The previously designed model-free Fuzzy controller works perfectly with MRE isolators; nevertheless, it produces control output even while the system is in isolation mode. To overcome this problem, a mathematical model is added to the fuzzy controller, enabling it to recognise when to cease vibration control for a broad range of excitation frequencies. In addition, a model-based sliding mode controller is developed to track the required model-generated response. Under random stimulation, the controller's performance is evaluated. The findings indicate that the MBSM controller is about 49.19% more effective than the MBF controller at isolating vibrations, at 41.39%.

Developing a mathematical model for a nonlinear system is a difficult and time-consuming undertaking. A model-free radial basis neural network sliding mode controller is designed to eliminate the burden of constructing a mathematical model for

control implementation. The 10 criteria are selected to evaluate the performance of the controller. The performance result demonstrates that the developed controller is able to modify the weights of the neural network such that the sliding mode controller generates the necessary control output for vibration isolation.

Implementation in real-time of the MBF controller on the MRE isolator for regulating vibrations in inertial mass of 0.583 kg reveals that the designed controller is effective throughout a broad frequency range. Consequently, the objective of controlling vibration in PCB boards has been achieved.

7.3   Major contribution from the current research

The developed MRE isolator was able to alter its natural frequency from 31 Hz to 52.70 Hz with a maximum change in stiffness of 190.09%, which is an excellent figure for PCB applications.

The MRE isolator successfully isolates vibration at natural frequency around 74.12% for 2.25 mm of amplitude of excitation, which was quite substantial and not achieved in any previous work.

A novel method was proposed for the development of a viscoelastic model that takes into account the influence of current input and amplitude of excitation using a state-space approach and CS frequency criteria. This method reduces the number of tests and development time significantly when compared to previous methods.

The developed model-based controller such as MBF controller and MBSM controller worked efficiently to isolate vibration for wide frequency range compared to the previously developed model free Fuzzy controller and sliding mode controller. The RBSM controller works efficiently without need of mathematical model in a given set of operating conditions.

7.4   Future scope of research

- Developing a design that includes permanent magnets in the coil circuit to reduce the amount of current supplied which reduces the temperature generation in the coil.

- The effect of larger amplitude of excitation on the CS frequency need to be estimated for developing the visco-elastic model.

- Developing controller by considering time delay in the system.

- The effect of temperature rise on the MRE properties required to be estimated for actual application must be investigated.

Reference

Agirre-Olabide, I., Lion, A., and Elejabarrieta, M. J. (2017) . "A new three-dimensional magneto-viscoelastic model for isotropic magnetorheological elastomers." *Smart Mater. Struct.*, 26(3) .

Ahmad Khairi, M. H., Mazlan, S. A., Ubaidillah, Ku Ahmad, K. Z., Choi, S. B., Abdul Aziz, S. A., and Yunus, N. A. (2017) . "The field-dependent complex modulus of magnetorheological elastomers consisting of sucrose acetate isobutyrate ester." *J. Intell. Mater. Syst. Struct.*, 28(14) , 1993–2004.

Alias, N. F., Muthalif, A. G. A., Arpan, K. A. M., and Nordin, N. H. D. (2018a) . "Experimental investigation of static properties of magnetorheological elastomer." *Iran. J. Sci. Technol. - Trans. Mech. Eng.,* 42(2) , 185–197.

An, J. S., Kwon, S. H., Choi, H. J., Jung, J. H., and Kim, Y. G. (2017) . "Modified silane-coated carbonyl iron/natural rubber composite elastomer and its magnetorheological performance." *Compos. Struct.*, 160, 1020–1026.

Aziz, S. A. A., Mazlan, S. A., Ismail, N. I. N., Ubaidillah, Khairi, M. H. A., and Yunus, N. A. (2017) . "Rheological properties of carbon nanotubes-reinforced magnetorheological elastomer." *J. Phys. Conf. Ser.*, 795(1) , 012074.

Aziz, S. A. A., Mazlan, S. A., Ubaidillah, U., Mohamad, N., Choi, S. B., Aziz, M. A. C., Johari, M. A. F., and Homma, K. (2020) . "Thermal Aging Rheological Behavior of Magnetorheological Elastomers Based on Silicone Rubber." *Int. J. Mol. Sci.* 2020, Vol. 21, Page 9007, 21(23) , 9007.

Bao Nguyen, X., Komatsuzaki, T., and Thi Truong, H. (2020) . "Novel semiactive suspension using a magnetorheological elastomer (MRE) -based absorber and adaptive neural network controller for systems with input constraints." *Mech. Sci.*, 11(2) , 465–479.

Bastola, A. K., Paudel, M., Li, L., and Li, W. (2020) . "Recent progress of magnetorheological elastomers: A review." *Smart Mater. Struct*., 29(12) .

Behrooz, M., Wang, X., and Gordaninejad, F. (2012) . "Control of structures featuring a new MRE isolator system." *Act. Passiv. Smart Struct. Integr. Syst*. 2012, 8341, 83411I.

Behrooz, M., Wang, X., and Gordaninejad, F. (2013) . "Modeling of a new magnetorheological elastomer-based isolator." https://doi.org/10.1117/12.2009946, 8688, 310–316.

Behrooz, M., Wang, X., and Gordaninejad, F. (2014a) . "Performance of a new magnetorheological elastomer isolation system." *Smart Mater. Struct*., 23(4) .

Behrooz, M., Wang, X., and Gordaninejad, F. (2014) . "Modeling of a new semi-active/passive magnetorheological elastomer isolator." *Smart Mater. Struct*., 23(4) , 045013.

Bica, I. (2009) . "Influence of the transverse magnetic field intensity upon the electric resistance of the magnetorheological elastomer containing graphite microparticles." *Mater. Lett., 63(26)* , 2230–2232.

Bica, I., Anitas, E. M., Averis, L. M. E., Kwon, S. H., and Choi, H. J. (2019) . "Magnetostrictive and viscoelastic characteristics of polyurethane-based magnetorheological elastomer." *J. Ind. Eng. Chem.,* 73, 128–133.

Bica, I., Balasoiu, M., and Kuklin, A. I. (2012) . "Anisotropic Silicone Rubber Based Magnetorheological Elastomer with Oil Silicone and Iron Microparticles." *Solid State Phenom.,* 190, 645–648.

Biller, A. M., Stolbov, O. V., and Raikher, Y. L. (2014) . "Modeling of particle interactions in magnetorheological elastomers." *J. Appl. Phys*., 116(11) .

Boczkowska, A., Awietjan, S., Boczkowska, A., and Awietjan, S. (2012) . "Microstructure and Properties of Magnetorheological Elastomers." *Adv. Elastomers - Technol. Prop. Appl*.

Borin, D., Stepanov, G., and Dohmen, E. (2019) . "Hybrid magnetoactive elastomer with a soft matrix and mixed powder." *Arch. Appl. Mech*., 89(1) , 105–117.

Böse, H. (2012) . "VISCOELASTIC PROPERTIES OF SILICONE-BASED MAGNETORHEOLOGICAL ELASTOMERS." http://dx.doi.org/10.1142/S0217979207045670, 21(28–29) , 4790–4797.

Bunoiu, M., and Bica, I. (2016) . "Magnetorheological elastomer based on silicone rubber, carbonyl iron and Rochelle salt: Effects of alternating electric and static magnetic fields intensities." *J. Ind. Eng. Chem*., 37, 312–318.

Cao, Y., Lu, H., Wang, W., Chen, D., Yang, F., Wang, G., and Rui, X. (2020) . "The dynamic mechanical properties of magnetorheological elastomer: Catalytic effect of carbonyl iron powder." https://doi.org/10.1177/1045389X20930090, 31(13) , 1567–1577.

Chen, D., Yu, M., Zhu, M., Qi, S., and Fu, J. (2016) . "Carbonyl iron powder surface modification of magnetorheological elastomers for vibration absorbing application." *Smart Mater. Struct*., 25(11) , 115005.

Chen, L., Gong, X. L., and Li, W. H. (2008) . "Effect of carbon black on the mechanical performances of magnetorheological elastomers." *Polym. Test*., 27(3) , 340–345.

Chen, L., and Jerrams, S. (2011) . "A rheological model of the dynamic behavior of magnetorheological elastomers." *J. Appl. Phys*., 110(1) .

Chen, L., Liu, S., Zhao, D., Yang, S., Dong, N., and Liu, Y. (2020) . "Magnetic properties of polyurethane magnetorheological elastomer based on carbon nanotubes." *Mater. Res*. Express, 7(7) , 076104.

Choi, J., and Chung, K. (2014) . "Magnetorheological Elastomer Based on Reactive Blend of Maleic Anhydride Grafted Chloroprene Rubber and Epoxidized Natural Rubber." *Elastomers Compos.,* 49(4) , 267–274.

Wang, X., Sun, H., and Basu, R. (2007) . "Vibration characteristics of smart sandwich beams embedded with magnetorheological elastomer cores." *Adv. Mar. Struct. - Proc. MARSTRUCT* 2007, 1st Int. Conf. Mar. Struct., 557–563.

Chokkalingam, R., Pandi, R. S., and Mahendran, M. (2011) . "Magnetomechanical behavior of Fe/PU magnetorheological elastomers." *J. Compos. Mater.,* 45(15) , 1545–1552.

Collaeott, R. A. (1977) . "Mechanical fault diagnosis and condition monitoring. (Book) ."

Costain, A. K., and Robichaud, J. M. (2004) . "Practical methods for vibration control of industrial equipment." *Annu. Meet. - Tech. Sect. Can. Pulp Pap. Assoc. Prepr.*

Cvek, M., Mrlík, M., Ilčíková, M., Mosnáček, J., Münster, L., and Pavlínek, V. (2017) . "Synthesis of Silicone Elastomers Containing Silyl-Based Polymer-Grafted Carbonyl Iron Particles: An Efficient Way to Improve Magnetorheological, Damping, and Sens-

ing Performances." *Macromolecules*, 50(5) , 2189–2200.

Dai, Z., Fu, J., Lai, J., Yang, Z., Bai, J., and Yu, M. (2018) . "A semi-active fuzzy vibration control strategy on narrowband random excitation." *Proc. 30th Chinese Control Decis. Conf. CCDC* 2018, 2129–2132.

Danas, K., Kankanala, S. V., and Triantafyllidis, N. (2012) . "Experiments and modeling of iron-particle-filled magnetorheological elastomers." *J. Mech. Phys. Solids,* 60(1) , 120–138.

Davis, L. C. (1999b) . "Model of magnetorheological elastomers." *J. Appl. Phys*., 85(6) , 3348–3351.

Du, H., Li, W., and Zhang, N. (2011) . "Semi-active variable stiffness vibration control of vehicle seat suspension using an MR elastomer isolator." *Smart Mater. Struct.*, 20(10) , 105003.

Eem, S. H., Jung, H. J., and Koo, J. H. (2012) . "Modeling of magneto-rheological elastomers for harmonic shear deformation." *IEEE Trans. Magn.,* 48(11) , 3080–3083.

Esmaeeli, R., Aliniagerdroudbari, H., Hashemi, S. R., Jbr, C., and Farhad, S. (2019) . "Designing a New Dynamic Mechanical Analysis (DMA) System for Testing Viscoelastic Materials at High Frequencies." *Model. Simul. Eng.,* 2019.

Fan, J., Yao, J., Yu, Y., and Li, Y. (2022) . "A macroscopic viscoelastic model of magnetorheological elastomer with different initial particle chain orientation angles based on fractional viscoelasticity." *Smart Mater. Struct.,* 31(2) , 025025.

Fan, Y., Gong, X., Xuan, S., Zhang, W., Zheng, J., and Jiang, W. (2011) . "Interfacial friction damping properties in magnetorheological elastomers." *Smart Mater. Struct.,* 20(3) .

Forster, E., Mayer, M., Rabindranath, R., Böse, H., Schlunck, G., Monkman, G. J., and Shamonin, M. (2013) . "Patterning of ultrasoft, agglutinative magnetorheological elastomers." *J. Appl. Polym. Sci.,* 128(4) , 2508–2515.

Fu, J., Bai, J., Lai, J., Li, P., Yu, M., and Lam, H. K. (2019) . "Adaptive fuzzy control of a magnetorheological elastomer vibration isolation system with time-varying sinusoidal excitations." *J. Sound Vib.,* 456, 386–406.

Fu, J., Lai, J., Yang, Z., Bai, J., and Yu, M. (2020) . "Fuzzy-neural network control for a Magnetorheological elastomer vibration isolation system." *Smart Mater. Struct*.

Fu, J., Lai, J., Yang, Z., Bai, J., and Yu, M. (2020) . "Fuzzy-neural network control for a

Magnetorheological elastomer vibration isolation system." *Smart Mater. Struct.,* 29(7) , 074001.

Fu, J., Li, P., Wang, Y., Liao, G., and Yu, M. (2016) . "Model-free fuzzy control of a magnetorheological elastomer vibration isolation system: analysis and experimental evaluation." *Smart Mater. Struct.,* 25(3) , 035030.

Fu, J., Liao, G., Yu, M., Li, P., and Lai, J. (2016) . "NARX neural network modeling and robustness analysis of magnetorheological elastomer isolator." *Smart Mater. Struct.,* 25(12) , 125019.

Fu, J., Yu, M., Dong, X. M., and Zhu, L. X. (2013a) . "Magnetorheological elastomer and its application on impact buffer." *J. Phys. Conf. Ser.,* 412(1) .

Fu, J., Zheng, X., Yu, M., Ju, B. X., and Yang, C. Y. (2013b) . "A new magnetorheological elastomer isolator in shear - Compression mixed mode." 2013 *IEEE/ASME Int. Conf. Adv. Intell. Mechatronics Mechatronics Hum. Wellbeing, AIM* 2013.

Gil-Negrete, N., Vinolas, J., and Kari, L. (2009) . "A Nonlinear Rubber Material Model Combining Fractional Order Viscoelasticity and Amplitude Dependent Effects." *J. Appl. Mech.,* 76(1) , 1–9.

Ginder, J. M., Nichols, M. E., Elie, L. D., and Clark, S. M. (2000) . "Controllable-stiffness components based on magnetorheological elastomers." *Smart Struct. Mater. 2000 Smart Struct. Integr. Syst.,* 3985, 418.

Gong, X. L., Zhang, X. Z., and Zhang, P. Q. (2005a) . "Fabrication and characterization of isotropic magnetorheological elastomers." *Polym. Test.,* 24(5) , 669–676.

Gu, X., Li, Y., and Li, J. (2016) . "Investigations on response time of magnetorheological elastomer isolator for real-time control implementation." *Smart Mater. Struct.,* 25(11) , 11LT04.

Guðmundsson, I. (2011) . "A Feasibility Study of Magnetorheological Elastomers for a Potential Application in Prosthetic Devices." (Thesis)

guide, L. L.-T. M. user's, and 1988, undefined. (2014) . "System identification toolbox." *researchgate.net.*

Guo, Y. Q., Zhang, J., He, D. Q., and Li, J. B. (2020) . "Magnetorheological Elastomer Precision Platform Control Using OFFO-PID Algorithm." *Adv. Mater. Sci. Eng.,* 2020.

Hafeez, M. heological elastomers and their propertieArslan, Usman, M., Umer, M. A., and Hanif, A. (2020) . "Recent progress in isotropic magnetors: A review." *Polymers*

(Basel) ., 12(12) , 1–35.

Hashi, H. A., Muthalif, A. G. A., and Diyana Nordin, N. H. (2016) . "Dynamic Tuning of Torsional Transmissibility Using Magnetorheological Elastomer: Modelling and Experimental Verification." *Iran. J. Sci. Technol. Trans. Mech. Eng.* 2016 403, 40(3) , 181–187.

Hegde, S., Kiran, K., and Gangadharan, K. V. (2015a) . "A novel approach to investigate effect of magnetic field on dynamic properties of natural rubber based isotropic thick magnetorheological elastomers in shear mode." *J. Cent. South Univ.*, 22(7) , 2612–2619.

Hellendoorn, H., and Thomas, C. (1993) . "Defuzzification in fuzzy controllers." *J. Intell. Fuzzy Syst.*, 1(2) , 109–123.

Hoang, N., Zhang, N., Li, W., and Du, H. (2011) . "Application of a magnetorheological elastomer to develop a torsional dynamic absorber for vibration reduction of powertrain." *Electro-Rheological Fluids Magneto-Rheological Suspens. - Proc.* 12th Int. Conf.

Hoang, N., Zhang, N., Li, W. H., and Du, H. (2013) . "Development of a torsional dynamic absorber using a magnetorheological elastomer for vibration reduction of a powertrain test rig." http://dx.doi.org/10.1177/1045389X13489361, 24(16) , 2036–2044.

Hu, Y., Wang, Y. L., Gong, X. L., Gong, X. Q., Zhang, X. Z., Jiang, W. Q., Zhang, P. Q., and Chen, Z. Y. (2005) . "New magnetorheological elastomers based on polyurethane/Si-rubber hybrid." *Polym. Test.,* 24(3) , 324–329.

Ismail, N. I. N., and Kamaruddin, S. (2017) . "Development of magnetorheological elastomers based on Deproteinised natural rubber as smart damping materials." *AIP Conf. Proc.*, 1901(1) , 030022.

Ivaneyko, D., Toshchevikov, V., Borin, D., Saphiannikova, M., and Heinrich, G. (2014a) . "Mechanical properties of magneto-sensitive elastomers in a homogeneous magnetic field: Theory and experiment." *Macromol. Symp.,* 338(1) .

Ivaneyko, D., Toshchevikov, V., Saphiannikova, M., and Heinrich, G. (2014b) . "Mechanical properties of magneto-sensitive elastomers: unification of the continuum-mechanics and microscopic theoretical approaches." *Soft Matter*, 10(13) , 2213–2225.

Jalali, A., Dianati, H., Norouzi, M., Vatandoost, H., and Ghatee, M. (2020) . "A novel bi-directional shear mode magneto-rheological elastomer vibration isolator." *J. Intell.*

Mater. Syst. Struct., 31(17) , 2002–2019.

Jolly, M. R., Carlson, J. D., and Muñoz, B. C. (1996) . "A model of the behaviour of magnetorheological materials." *Smart Mater. Struct.*, 5(5) , 607.

Jolly, M. R., Carlson, J. D., Muñoz, B. C., and Bullions, T. A. (1996c) . "The magneto-viscoelastic response of elastomer composites consisting of ferrous particles embedded in a polymer matrix." *J. Intell. Mater. Syst. Struct.*, 7(6) , 613–622.

Jung, H. S., Kwon, S. H., Choi, H. J., Jung, J. H., and Kim, Y. G. (2016) . "Magnetic carbonyl iron/natural rubber composite elastomer and its magnetorheology." *Compos. Struct.*, 136, 106–112.

Kaleta, J., Królewicz, M., and Lewandowski, D. (2011) . "Magnetomechanical properties of anisotropic and isotropic magnetorheological composites with thermoplastic elastomer matrices." *Smart Mater. Struct.*, 20(8) , 085006.

Kallio, M. (2005) . "The elastic and damping properties of magnetorheological elastomers." (565) , 3–146.

Kärkkäinen, K. K. (2000) . "Effective permittivity of mixtures: numerical validation by the FDTD method." *IEEE Trans. Geosci. Remote Sens.*, 38(3) , 1303–1308.

Kashima, S., Miyasaka, F., and Hirata, K. (2012) . "Novel soft actuator using magnetorheological elastomer." *IEEE Trans. Magn.*, 48(4) , 1649–1652.

Kavlicoglu, B., Wallis, B., Sahin, H., and Liu, Y. (2011) . "Magnetorheological elastomer mount for shock and vibration isolation." *Act. Passiv. Smart Struct. Integr. Syst.* 2011, 7977(775) , 79770Y.

Khairi, M. H. A., Fatah, A. Y. A., Mazlan, S. A., Ubaidillah, U., Nordin, N. A., Ismail, N. I. N., Choi, S. B., and Aziz, S. A. A. (2019) . "Enhancement of Particle Alignment Using Silicone Oil Plasticizer and Its Effects on the Field-Dependent Properties of Magnetorheological Elastomers." *Int. J. Mol. Sci.* 2019, Vol. 20, Page 4085, 20(17) , 4085.

Khairi, M. H. A., Mazlan, S. A., Ubaidillah, Aziz, S. A. A., and Hapipi, N. M. (2018) . "Performance of magnetorheological elastomer based silicone/SAIB." *Key Eng. Mater.*

Kiran, K., Poojary, U. R., and Gangadharan, K. V. (2022) . "Fractional-order viscoelastic modeling of the magnetic field dependent transmissibility response of MRE isolator." *J. Intell. Mater. Syst. Struct.*

Koo, J. H., Khan, F., Jang, D. D., and Jung, H. J. (2010) . "Dynamic characterization

and modeling of magneto-rheological elastomers under compressive loadings." *Smart Mater. Struct.*, 19(11) .

Kramarenko, E. Y., Chertovich, A. V., Stepanov, G. V., Semisalova, A. S., Makarova, L. A., Perov, N. S., and Khokhlov, A. R. (2015) . "Magnetic and viscoelastic response of elastomers with hard magnetic filler." *Smart Mater. Struct.*, 24(3) , 35002.

Kulik, V. M., Semenov, B. N., Boiko, A. V., Seoudi, B. M., Chun, H. H., and Lee, I. (2009) . "Measurement of dynamic properties of viscoelastic materials." *Exp. Mech.,* 49(3) , 417–425.

Kurniawan, C., Eko, A. S., Ayu, Y. S., Sihite, P. T. A., Ginting, M., Simamora, P., and Sebayang, P. (2017) . "Synthesis and Characterization of Magnetic Elastomer based PEG-Coated Fe3O4 from Natural Iron Sand." *IOP Conf. Ser. Mater. Sci. Eng.*, 202(1) , 012051.

Kwon, S. H., An, J. S., Choi, S. Y., Chung, K. H., and Choi, H. J. (2019) . "Poly(glycidyl methacrylate) Coated Soft-Magnetic Carbonyl Iron/Silicone Rubber Composite Elastomer and Its Magnetorheology." *Macromol. Res.* 2019 275, 27(5) , 448–453.

Lectez, A. S., and Verron, E. (2016) . "Influence of large strain preloads on the viscoelastic response of rubber-like materials under small oscillations." *Int. J. Non. Linear. Mech.*, 81, 1–7.

Lee, C. H., Park, J. H., Lee, E. S., Cho, W. O., Kim, C. H., and Kim, N. G. (2012) . "Vibration damping of hollow shaft by using magnetorheological elastomer." *19th Int. Congr. Sound Vib.* 2012, ICSV 2012.

Lee, C. J., Kwon, S. H., Choi, H. J., Chung, K. H., and Jung, J. H. (2018) . "Enhanced magnetorheological performance of carbonyl iron/natural rubber composite elastomer with gamma-ferrite additive." *Colloid Polym. Sci.*, 296(9) , 1609–1613.

Lee, J. Y., Kumar, V., and Lee, D. J. (2019) . "Compressive properties of magnetorheological elastomer with different magnetic fields and types of filler." *Polym. Adv. Technol.*, 30(4) , 1106–1115.

Lee, K. H., Park, J. E., and Kim, Y. K. (2019) . "Design and analysis of prototype of smart stiffness variable coupling for adaptive torsional vibration reduction." *Trans. Korean Soc. Mech. Eng. A.*

Lee, T. J., Morgenstern, A. H., Höft, T. A., Nelson-Cheeseman, B. B., Lee, T. J., Morgenstern, A. H., Höft, T. A., and Nelson-Cheeseman, B. B. (2019) . "Dispersion of

particulate in solvent cast magnetic thermoplastic polyurethane elastomer composites." *AIMS Mater. Sci.* 2019 3354, 6(3) , 354–362.

Leng, D., Xu, K., Ma, Y., Liu, G., and Sun, L. (2018) . "Modeling the behaviors of magnetorheological elastomer isolator in shear-compression mixed mode utilizing artificial neural network optimized by fuzzy algorithm (ANNOFA) ." *Smart Mater. Struct.*, 27(11) .

Li, H., Wang, W., Wang, X., Han, Q., Liu, J., Qin, Z., Xiong, J., and Guan, Z. (2020) . "A nonlinear analytical model of composite plate structure with an MRE function layer considering internal magnetic and temperature fields." *Compos. Sci. Technol.*, 200, 108445.

Li, J., Gong, X., Xu, Z., and Jiang, W. (2008) . "The effect of pre-structure process on magnetorheological elastomer performance." *Zeitschrift fuer Met. Res. Adv. Tech.*, 99(12) , 1358–1364.

Li, R., and Sun, L. Z. (2011) . "Dynamic mechanical behavior of magnetorheological nanocomposites filled with carbon nanotubes." *Appl. Phys. Lett.*, 99(13) , 131912.

Li, R., and Sun, L. Z. (2013) . "Viscoelastic responses of silicone-rubber-based magnetorheological elastomers under compressive and shear loadings." *J. Eng. Mater. Technol. Trans. ASME*, 135(2) , 1–7.

Li, W. H., and Zhang, X. Z. (2010) . "A study of the magnetorheological effect of bimodal particle based magnetorheological elastomers." *Smart Mater. Struct.*, 19(3) , 035002.

Li, W. H., Zhou, Y., and Tian, T. F. (2010a) . "Viscoelastic properties of MR elastomers under harmonic loading." *Rheol. Acta*, 49(7) , 733–740.

Li, W., Qi, S., Zhu, M., Xia, D., Fu, J., and Yu, M. (2021b) . "Improving transient magnetorheological response of magnetorheological elastomer by incorporating CIP@FeNi particles." *Smart Mater. Struct.*, 30(2) .

Li, Y., and Li, J. (2014) . "Development and Modeling of a Highly-Adjustable Base Isolator Utilizing Magnetorheological Elastomer." *ASME 2013 Conf. Smart Mater. Adapt. Struct. Intell. Syst. SMASIS* 2013, 1.

Li, Y., and Li, J. (2015a) . "A highly adjustable base isolator utilizing magnetorheological elastomer: Experimental testing and modeling." *J. Vib. Acoust. Trans. ASME,* 137(1) , 1–7.

Li, Y., and Li, J. (2015) . "Finite element design and analysis of adaptive base isolator utilizing laminated multiple magnetorheological elastomer layers." *J. Intell. Mater. Syst. Struct.,* 26(14) , 1861–1870.

Li, Y., and Li, J. (2017) . "On rate-dependent mechanical model for adaptive magnetorheological elastomer base isolator." *Smart Mater. Struct.*, 26(4) , 045001.

Liao, G., Gong, X., and Xuan, S. (2013) . "Magnetic field-induced compressive property of magnetorheological elastomer under high strain rate." *Ind. Eng. Chem. Res.*

Liao, G., Gong, X., and Xuan, S. (2013) . "Magnetic Field-Induced Compressive Property of Magnetorheological Elastomer under High Strain Rate." *Ind. Eng. Chem. Res.*, 52(25) , 8445–8453.

Liu, C., Hemmatian, M., Sedaghati, R., and Wen, G. (2020) . "Development and Control of Magnetorheological Elastomer-Based Semi-active Seat Suspension Isolator Using Adaptive Neural Network." *Front. Mater.*, 7, 171.

Liu, C., Sedaghati, R., and Shang, P. (2021) . "A novel semi-active switching control scheme for magnetorheological elastomer-based vibration isolator under dynamic input saturation." *Smart Mater. Struct.*, 30(9) .

Lokander, M., and Stenberg, B. (2003) . "Performance of isotropic magnetorheological rubber materials." *Polym. Test.*, 22(3) , 245–251.

Mamdani, E. H., and Assilian, S. (1975) . "An experiment in linguistic synthesis with a fuzzy logic controller." *Int. J. Man. Mach. Stud.*, 7(1) , 1–13.

Menegazzo, J., and Wangenheim, A. von. (2021). "Road surface type classification based on inertial sensors and machine learning: A comparison between classical and deep machine learning approaches for multi-contextual real-world scenarios." Computing, 103(10), 2143–2170.

Masłowski, M., and Zaborski, M. (2012) . "Smart Materials Based on Magnetorheological Composites." *Mater. Sci. Forum*, 714, 167–173.

Mital, S. K., Murthy, P. L. N., and Goldberg, R. K. (1996) . "Micromechanics for Particulate Reinforced Composites."

Nam, T. H., Petríková, I., and Marvalová, B. (2021) . "Experimental and numerical research of stress relaxation behavior of magnetorheological elastomer." *Polym. Test.*, 93, 106886.

Nayak, B., Dwivedy, S. K., and Murthy, K. S. R. K. (2015) . "Fabrication and charac-

terization of magnetorheological elastomer with carbon black." *J. Intell. Mater. Syst. Struct.,* 26(7) , 830–839.

Nguyen, V. Q., and Ramanujan, R. V. (2010) . "Novel coiling behavior in magnet-polymer composites." *Macromol. Chem. Phys*., 211(6) , 618–626.

Nguyen, X. B., Komatsuzaki, T., Iwata, Y., and Asanuma, H. (2017) . "Fuzzy Semiactive Vibration Control of Structures Using Magnetorheological Elastomer." *Shock Vib*., 2017.

Nguyen, X. B., Komatsuzaki, T., Iwata, Y., and Asanuma, H. (2018b) . "Modeling and semi-active fuzzy control of magnetorheological elastomer-based isolator for seismic response reduction." *Mech. Syst. Signal Process*., 101, 449–466.

Nguyen, X. B., Komatsuzaki, T., and Zhang, N. (2020) . "A nonlinear magnetorheological elastomer model based on fractional viscoelasticity, magnetic dipole interactions, and adaptive smooth Coulomb friction." *Mech. Syst. Signal Process*., 141, 106438.

Ni, Z. C., Gong, X. L., Li, J. F., and Chen, L. (2009b) . "Study on a dynamic stiffness-tuning absorber with squeeze-strain enhanced magnetorheological elastomer." *J. Intell. Mater. Syst. Struct.*, 20(10) , 1195–1202.

Norouzi, M., Gilani, M., Alehashem, S. M. S., and Vatandoost, H. (2017) . "Dynamic Characterization and Modeling of Isotropic Magnetorheological Elastomers under Tensile-Compressive Loadings." *IEEE Trans. Magn.*, 53(9) .

Opie, S., and Yim, W. (2011) . "Design and control of a real-time variable modulus vibration isolator." *J. Intell. Mater. Syst. Struct.*, 22(2) , 113–125.

Peng, G. R., Li, W. H., Du, H., Deng, H. X., and Alici, G. (2014) . "Modelling and identifying the parameters of a magneto-rheological damper with a force-lag phenomenon." *Appl. Math. Model*., 38(15–16) , 3763–3773.

Poojary, U. R., and Gangadharan, K. V. (2016b) . "Experimental investigation on the effect of magnetic field on strain dependent dynamic stiffness of magnetorheological elastomer." *Rheol. Acta*, 55(11–12) , 993–1001.

Poojary, U. R., and Gangadharan, K. V. (2018) . "Integer and fractional order-based viscoelastic constitutive modeling to predict the frequency and magnetic field-induced properties of magnetorheological elastomer." *J. Vib. Acoust. Trans. ASME*, 140(4) .

Praveen, S. K., Kuchibhatla, S. A. R., Singh, A. K., and Gangadharan, K. V. (2020) . "Performance of magnetorheological elastomer based torsional vibration isolation sys-

tem for dynamic loading conditions." *J. Cent. South Univ.* 2020 271, 27(1) , 144–154.

Qi, S., Yu, M., Fu, J., Li, P. D., and Zhu, M. (2015) . "Creep and recovery behaviors of magnetorheological elastomer based on polyurethane/epoxy resin IPNs matrix." *Smart Mater. Struct.*, 25(1) , 015020.

Qi, S., Yu, M., Fu, J., Zhu, M., Xie, Y., and Li, W. (2018) . "An EPDM/MVQ polymer blend based magnetorheological elastomer with good thermostability and mechanical performance." *Soft Matter*, 14(42) , 8521–8528.

Raa Khimi, S., and Lai, N. T. (2018) . "Optimisation of Pre-structuring Process of Magnetorheological Elastomer Performance." *J. Phys. Conf. Ser.,* 1082(1) , 012014.

Raa Khimi, S., and Pickering, K. L. (2016) . "The effect of silane coupling agent on the dynamic mechanical properties of iron sand/ natural rubber magnetorheological elastomers." *Compos. Part B Eng.,* 90, 115–125.

Samal, S., Škodová, M., and Blanco, I. (2019) . "Effects of Filler Distribution on Magnetorheological Silicon-Based Composites." *Mater. 2019,* Vol. 12, Page 3017, 12(18) , 3017.

Sedlacik, M., Mrlik, M., Babayan, V., and Pavlinek, V. (2016) . "Magnetorheological elastomers with efficient electromagnetic shielding." *Compos. Struct.*, 135, 199–204.

Shen, Y., Golnaraghi, M. F., and Heppler, G. R. (2004) . "Experimental research and modeling of magnetorheological elastomers." *J. Intell. Mater. Syst. Struct.,* 15(1) , 27–35.

Song, H. J., Padalka, O., Wereley, N. M., and Bell, R. C. (2009) . "Impact of nanowire versus spherical microparticles in magnetorheological elastomer composites." *Collect. Tech. Pap. - AIAA/ASME/ASCE/AHS/ASC Struct. Struct. Dyn. Mater. Conf.*

Song, X., Wang, W., Yang, F., Wang, G., and Rui, X. (2019) . "The study of magnetorheological elastomer based on natural rubber (NR) /thermoplastic elastomer SEBS hybrid matrix: Experimental and numerical simulation." *Proc. ASME Des. Eng. Tech. Conf.*

Sorokin, V. V., Ecker, E., Stepanov, G. V., Shamonin, M., Monkman, G. J., Kramarenko, E. Y., and Khokhlov, A. R. (2014b) . "Experimental study of the magnetic field enhanced Payne effect in magnetorheological elastomers." *Soft Matter,* 10(43) , 8765–8776.

Sorokin, V. V., Stepanov, G. V., Shamonin, M., Monkman, G. J., and Kramarenko, E. Y. (2017) . "Magnetorheological behavior of magnetoactive elastomers filled with bimodal

iron and magnetite particles." *Smart Mater. Struct.,* 26(3) .

Souza Eloy, F. de, Gomes, G. F., Ancelotti, A. C., Cunha, S. S. da, Bombard, A. J. F., and Junqueira, D. M. (2018) . "Experimental dynamic analysis of composite sandwich beams with magnetorheological honeycomb core." *Eng. Struct.*, 176, 231–242.

Stepanov, G. V., Borin, D. Y., Bakhtiiarov, A. V., and Storozhenko, P. A. (2020) . "Negative coercivity of magnetic elastomers filled with magnetically hard particles." *J. Magn. Magn. Mater.*, 498, 166125.

Sun, S. S., Yang, J., Deng, H. X., Du, H., Li, W. H., Alici, G., and Nakano, M. (2015a) . "Horizontal vibration reduction of a seat suspension using negative changing stiffness magnetorheological elastomer isolators." *Int. J. Veh. Des.*, 68(1–3) , 104–118.

Sun, S. S., Yildirim, T., Wu, J., Yang, J., Du, H., Zhang, S. W., and Li, W. H. (2017) . "Design and verification of a hybrid nonlinear MRE vibration absorber for controllable broadband performance." *Smart Mater. Struct.*, 26(9) , 095039.

Sun, S., Yang, J., Li, W., Deng, H., Du, H., and Alici, G. (2015) . "Development of an MRE adaptive tuned vibration absorber with self-sensing capability." *Smart Mater. Struct.*, 24(9) , 095012.

Suo, S., Xu, Z., Li, W., and Gan, Y. (2018) . "Improved Mathematical Model for Analysis of the Payne Effect of Magnetorheological Elastomers." *J. Aerosp. Eng.*, 31(5) , 04018046.

Susheelkumar, G. N., Murigendrappa, S. M., and Gangadharan, K. V. (2019) . "Theoretical and experimental investigation of model-free adaptive fuzzy sliding mode control for MRE based adaptive tuned vibration absorber." *Smart Mater. Struct.*, 28(4) , 045017.

Syam, T. M. I., Hegazi, A. A. A., Muthalif, A. G. A., and Badri, Y. (2021) . "Magnetorheological elastomer-based variable stiffness flexible coupling for vibration isolation." *Trans. Can. Soc. Mech. Eng.*, 46(1) .

Tao, Y., Rui, X., and Yang, F. (2019) . "Investigation of the impacts on magnetic permeability of MREs." *J. Magn. Magn. Mater.*, 477, 269–274.

Tian, T. F., Li, W. H., Alici, G., Du, H., and Deng, Y. M. (2011) . "Microstructure and magnetorheology of graphite-based MR elastomers." *Rheol. Acta*, 50(9–10) , 825–836.

Tian, T., and Nakano, M. (2018) . "Fabrication and characterisation of anisotropic magnetorheological elastomer with 45° iron particle alignment at various silicone oil con-

centrations." *J. Intell. Mater. Syst. Struct.,* 29(2) , 151–159.

Torvik, P. J., and Bagley, R. L. (1984) . "On the appearance of the fractional derivative in the behavior of real materials." *J. Appl. Mech. Trans. ASME,* 51(2) , 294–298.

Ubaidillah, Sutrisno, J., Purwanto, A., and Mazlan, S. A. (2015) . "Recent progress on magnetorheological solids: Materials, fabrication, testing, and applications." *Adv. Eng. Mater.*, 17(5) , 563–597.

Varga, Z., Filipcsei, G., and Zrínyi, M. (2006) . "Magnetic field sensitive functional elastomers with tuneable elastic modulus." *Polymer (Guildf)* ., 47(1) , 227–233.

Wahab, N. A. A., Mazlan, S. A., Hairuddin, K., and Zamzuri, H. (2015) . "Simulation study of electromagnetic circuit design in laminated magnetorheological elastomer isolator." *IOP Conf. Ser. Mater. Sci. Eng.*, 100(1) .

Wahab, N. A. A., Mazlan, S. A., Ubaidillah, Kamaruddin, S., Ismail, N. I. N., Choi, S. B., and Sharif, A. H. R. (2016) . "Fabrication and investigation on field-dependent properties of natural rubber based magneto-rheological elastomer isolator." *Smart Mater. Struct.*, 25(10) , 107002.

Wang, D. H., and Liao, W. H. (2011) . "Magnetorheological fluid dampers: A review of parametric modelling." *Smart Mater. Struct.,* 20(2) .

Wang, Q., Dong, X., Li, L., and Ou, J. (2017) . "A nonlinear model of magnetorheological elastomer with wide amplitude range and variable frequencies." *Smart Mater. Struct.,* 26(6) , 065010.

Wen, Y. K. (1976) . "Method for Random Vibration of Hysteretic Systems." *J. Eng. Mech. Div.*, 102(2) , 249–263.

Winthrop, M. F., Baker, W. P., and Cobb, R. G. (2005) . "A variable stiffness device selection and design tool for lightly damped structures." *J. Sound Vib.*, 287(4–5) , 667–682.

Wu, C., Cheng, C., El-Aty, A. A., Li, T., Qin, Y., Yang, Q., Hu, S., Xu, Y., and Guo, X. (2020) . "Influence of particles size and concentration of carbonyl iron powder on magnetorheological properties of silicone rubber-based magnetorheological elastomer." *Mater. Res. Express,* 7(8) , 0–13.

Xie, Y., Qi, S., Fu, J., Tian, R., Liu, F., and Yu, M. (2020) . "A pre-magnetized NdFeB-particle reinforced magnetorheological elastomer." *Smart Mater. Struct.*, 30(1) .

Xing, Z. W., Yu, M., Fu, J., Wang, Y., and Zhao, L. J. (2015) . "A laminated magnetorhe-

ological elastomer bearing prototype for seismic mitigation of bridge superstructures." *J. Intell. Mater. Syst. Struct.,* 26(14) , 1818–1825.

Xu, Z. D., Suo, S., and Lu, Y. (2016) . "Vibration control of platform structures with magnetorheological elastomer isolators based on an improved SAVS law." *Smart Mater. Struct.,* 25(6) .

Yang, C. Y., Fu, J., Yu, M., Zheng, X., and Ju, B. X. (2015) . "A new magnetorheological elastomer isolator in shear-compression mixed mode." *J. Intell. Mater. Syst. Struct.,* 26(10) , 1290–1300.

Yang, J., Du, H., Li, W., Li, Y., Li, J., Sun, S., and Deng, H. X. (2013a) . "Experimental study and modeling of a novel magnetorheological elastomer isolator." *Smart Mater. Struct.,* 22(11) .

Yang, J., Sun, S. S., Du, H., Li, W. H., Alici, G., and Deng, H. X. (2014) . "A novel magnetorheological elastomer isolator with negative changing stiffness for vibration reduction." *Smart Mater. Struct.,* 23(10) , 105023.

Yang, S., Wang, P., Liu, Y., Dong, X., Tong, Y., and Zhao, Y. (2021) . "Modified Bouc-Wen Model Based on Fractional Derivative and Application in Magnetorheological Elastomer." *Front. Mater., 8(October)* , 1–14.

Yang, X., Shuai, C. G., and Yang, S. L. (2013) . "Magnetorheological Effect of NDI Polyurethane-Based MR Elastomers." *Adv. Mater. Res.,* 750–752, 832–835.

Yao, J., Yang, W., Gao, Y., Scarpa, F., and Li, Y. (2019) . "Magnetorheological elastomers with particle chain orientation: Modelling and experiments." *Smart Mater. Struct.,* 28(9) .

Yarra, S., Gordaninejad, F., Behrooz, M., and Pekcan, G. (2019) . "Performance of natural rubber and silicone-based magnetorheological elastomers under large-strain combined axial and shear loading." *J. Intell. Mater. Syst. Struct.,* 30(2) , 228–242.

Yu, M., and Ju, B. X. (2011) . "Dynamic mechanical properties testing for shear mode of magnetorheological elastomer." *Gongneng Cailiao/Journal Funct. Mater.*

Yu, M., Qi, S., Fu, J., Yang, P. A., and Zhu, M. (2015a) . "Preparation and characterization of a novel magnetorheological elastomer based on polyurethane/epoxy resin IPNs matrix." *Smart Mater. Struct.,* 24(4) .

Yu, M., Qi, S., Fu, J., and Zhu, M. (2015) . "A high-damping magnetorheological elastomer with bi-directional magnetic-control modulus for potential application in seismol-

ogy." *Appl. Phys. Lett.*, 107(11) , 111901.

Yu, M., Qi, S., Fu, J., Zhu, M., and Chen, D. (2017) . "Understanding the reinforcing behaviors of polyaniline-modified carbonyl iron particles in magnetorheological elastomer based on polyurethane/epoxy resin IPNs matrix." *Compos. Sci. Technol.*, 139, 36–46.

Yu, M., Zhu, M., Fu, J., Yang, P. A., and Qi, S. (2015) . "A dimorphic magnetorheological elastomer incorporated with Fe nano-flakes modified carbonyl iron particles: preparation and characterization." *Smart Mater. Struct.*, 24(11) , 115021.

Yu, Y. (2014) . "Parameter Identification of an Improved Dahl Model for Magnetorheological Elastomer Base Isolator Based on Enhanced Genetic Algorithm." II(December) , 9–12.

Yu, Y., Hoshyar, A. N., Li, H., Zhang, G., and Wang, W. (2021) . "Nonlinear characterization of magnetorheological elastomer-based smart device for structural seismic mitigation." *Int. J. Smart Nano Mater.*, 12(4) , 390–428.

Yu, Y., Li, Y., and Li, J. (2014) . "A new hysteretic model for magnetorheological elastomer base isolator and parameter identification based on modified artificial fish swarm algorithm." *31st Int. Symp. Autom. Robot. Constr. Mining, ISARC 2014 - Proc.*

Yu, Y., Li, Y., and Li, J. (2015e) . "Parameter identification of a novel strain stiffening model for magnetorheological elastomer base isolator utilizing enhanced particle swarm optimization." *J. Intell. Mater. Syst. Struct., 26(18) , 2446–2462.*

Yu, Y., Li, Y., and Li, J. (2015) . "Nonparametric modeling of magnetorheological elastomer base isolator based on artificial neural network optimized by ant colony algorithm." *J. Intell. Mater. Syst. Struct.,* 26(14) , 1789–1798.

Yu, Y., Li, Y., and Li, J. (2015) . "Parameter identification and sensitivity analysis of an improved LuGre friction model for magnetorheological elastomer base isolator." *Meccanica, 50(11) , 2691–2707.*

Yu, Y., Li, Y., and Li, J. (2015i) . "Forecasting hysteresis behaviours of magnetorheological elastomer base isolator utilizing a hybrid model based on support vector regression and improved particle swarm optimization." *Smart Mater. Struct.,* 24(3) , 35025.

Yu, Y., Li, Y., Li, J., and Gu, X. (2016a) . "A hysteresis model for dynamic behaviour of magnetorheological elastomer base isolator." *Smart Mater. Struct.,* 25(5) .

Yu, Y., Li, Y., Li, J., Gu, X., and Royel, S. (2018) . "Nonlinear Characterization of the

162

MRE Isolator Using Binary-Coded Discrete CSO and ELM." *Int. J. Struct. Stab. Dyn.,* 18(8) .

Yunus, N. A., Mazlan, S. A., Ubaidillah, Aziz, S. A. A., Khairi, M. H. A., Wahab, N. A. A., and Shilan, S. T. (2016) . "Investigation on magnetic field dependent modulus of epoxidized natural rubber based magnetorheological elastomer." *J. Phys. Conf. Ser.,* 776(1) , 012024.

Zhang, W., Gong, X. L., and Chen, L. (2010) . "A Gaussian distribution model of anisotropic magnetorheological elastomers." *J. Magn. Magn. Mater.,* 322(23) , 3797–3801.

Zhang, X., Li, W., and Gong, X. L. (2008a) . "An effective permeability model to predict field-dependent modulus of magnetorheological elastomers." *Commun. Nonlinear Sci. Numer. Simul.,* 13(9) , 1910–1916.

Zhang, X., Peng, S., Wen, W., and Li, W. (2008b) . "Analysis and fabrication of patterned magnetorheological elastomers." *Smart Mater. Struct.,* 17(4) .

Zhao, J., and Bose, B. K. (2002) . "Evaluation of membership functions for fuzzy logic controlled induction motor drive." *IECON Proc. (Industrial Electron. Conf.,* 229–234.

Zhao, L., Yu, M., Fu, J., Zhu, M., and Li, B. (2017a) . "A miniature MRE isolator for lateral vibration suppression of bridge monitoring equipment: Design and verification." *Smart Mater. Struct.,* 26(4) .

Zhao, L., Yu, M., Fu, J., Zhu, M., and Li, B. (2017) . "A miniature MRE isolator for lateral vibration suppression of bridge monitoring equipment: design and verification." *Smart Mater. Struct.,* 26(4) , 047001.

Zheng, H. M., Dong, D. D., and Zhu, L. H. (2014) . "Tunable stiffness and damping vibration control strategy based on magnetorheological elastomer isolator." *Appl. Mech. Mater.,* 543–547, 1461–1466.

Zhong, H., Pei, Y., Hu, Z., Zhang, P., Guo, J., Gong, X., and Zhao, Y. (2019) . "A study of the heat transfer properties of CIP doped magnetorheological elastomers." *Smart Mater. Struct.,* 28(2) .

Zhou, G. Y., and Jiang, Z. Y. (2004) . "Deformation in magnetorheological elastomer and elastomer–ferromagnet composite driven by a magnetic field." *Smart Mater. Struct.,* 13(2) , 309.

Zhou, Y., Jerrams, S., Betts, A., Farrell, G., and Chen, L. (2015) . "The influence of par-

ticle content on the equi-biaxial fatigue behaviour of magnetorheological elastomers."
Mater. Des., 67, 398–404.

Zhu, G., Xiong, Y., Li, Z., Li, M., and Bai, X. 'Frank.' (2020) . "A fractional-order model on the dynamic mechanical behavior of magnetorheological elastomers." *Smart Mater. Struct.,* 29(2) , 025020.

Zhu, J. T., Xu, Z. D., and Guo, Y. Q. (2012) . "Magnetoviscoelasticity parametric model of an MR elastomer vibration mitigation device." *Smart Mater. Struct.,* 21(7) .

Zhu, M., Qi, S., Xie, Y., Fu, J., and Yu, M. (2019) . "Transient responses of magnetorheological elastomer and isolator under shear mode." *Smart Mater. Struct.,* 28(4) .

Zhu, M., Yu, M., Qi, S., and Fu, J. (2018) . "Investigations on response time of magnetorheological elastomer under compression mode." *Smart Mater. Struct.,* 27(5) , 055017.

Zhu, Y., Gong, X., Dang, H., Zhang, X., Zhang, P., Zhu, Y., Gong, X., Dang, H., Zhang, X., and Zhang, P. (2006) . "Numerical Analysis on Magnetic-induced Shear Modulus of Magnetorheological Elastomers Based on Multi-chain Model." *Chinese J. Chem. Phys.* , 2006, Vol. 19, Issue 2, Pages 126-130, 19(2) , 126–130.

Zou, A., Xu, L., Zhu, M., Qi, S., and Yu, M. (2018) . "Fuzzy control study on a transformer vibration isolation system." *Proc. 30th Chinese Control Decis. Conf. CCDC 2018.*

Sl. No.	Title of the paper	Name of the Authors as it is in the paper	Name of the Journal	Month, Year of Publication	Category*
1.	Developing the viscoelastic model and modal based fuzzy controller for the MRE isolator for the wide frequency range vibration isolation	Katari Kiran, Umanath R Poojary, K V Gangadharan	Journal of the Brazilian Society of Mechanical Sciences and Engineering	May 2022	1
2.	Fractional-order Viscoelastic modelling of the magnetic field dependent transmissibility response of MRE isolator	Katari Kiran, Umanath R Poojary, K V Gangadharan	Journal of Intelligent materials and structures	FEB 2022	1
3.	Dynamic response of MRE sandwich structure under non-homogenous magnetic field	Umanath R Poojary, Sriharsha Hegde, Katari Kiran, K.V. Gangadharan	Journal of the Korean Physical Society	July 2021	1
4.	Modelling of frictional damper with equivalent viscous damper	Katari Kiran, K V Gangadharan	AIP Conference Proceedings	July 2020	4
5.	Variable Stiffness Magnetorheological Isolator	Katari Kiran, K V Gangadharan	Indian Patent	May 2019	5

*Category:

1: Journal paper, full paper reviewed

2: Journal paper, abstract reviews

3. Conferance/Symposium paper, abstract reviewed

4. Conferance/Symposium paper, full paper reviewed.

5. Others (Patents)

Katari Kiran   Dr K V Gangadharan

Research Scholar   Reasearch Guide

Name and signature, with Date Name and signature, with Date

Appendix

List of instruments used in the work

1. APS 420 shaker:

Description The strongest ELECTRO-SEIS® Long-Stroke vibration exciter to date is used for vibration tests of airplanes and other large structures. With a maximum force of 900 N and up to 150 mm stroke the shaker unlocks a new performance level.

Specifications:

- Force (Sine Peak): 900 N (200 lbf)

- Velocity (Sine Peak): 1,000 mm/s (39 inch/s)

- Stroke (Peak - Peak): 150 mm (5.9 inch)

- Frequency Range: DC … 200 Hz

- Operation: horizontal or vertical

- Armature Weight: 3.6 kg (8.0 lb)

- Max. Overhung Load at Armature Attachment Point: 9.0 kg (20 lb)

- DC Coil Resistance: 1.1 Ω

- Total Shaker Weight: 140 kg (310 lb)

- Shipping Weight: 165 kg (365 lb)

- Overall Dimension: L x W x H 591 x 360 x 280 mm (23.3 x 14.2 x 11.0 inch)

- Operating Temperature: 5 ... 40 degrees C

- Storage Temperature: -25 ... 55 degrees C

2. NI cRIO 9024:

Description The cRIO-9024 is an embedded real-time controller ideal for advanced control and monitoring applications. This rugged, fanless controller features a variety of connectivity ports, including two Ethernet, one USB, and one serial. The cRIO-9024 does not include integrated C Series I/O module slots, so to use C Series I/O modules, you can combine the cRIO-9024 with a compatible CompactRIO Chassis.

Specifications:

- Manufacturer: National Instruments

- Type: CompactRIO Controller

- Processor: 1.33 GHz dual-core Intel Atom processor

- Memory: 512 MB DRAM, 2 GB nonvolatile storage

- Operating System: NI Linux Real-Time OS

- Communication Interfaces: Ethernet, RS232, RS485, USB, CAN, FPGA

- Power Supply: 24 VDC

- Software: LabVIEW Real-Time Module for programming and configuring the controller

3. NI 9264:

Description The NI-9264 is a simultaneously updating analog output module that accommodates higher-channel-count systems. Higher density modules conserve chassis space, which leaves room for other measurement types. Each channel has its own digital-to-analog converter. The spring-terminal version of the NI-9264 uses a 36-position connector for the output channels, and each channel has a ground connection.

Specifications:

- Manufacturer: National Instruments

- Type: Analog Output Module

- Channels: 4

- Resolution: 16 bits

- Output Range: ±10 V, 0-10 V, or 0-5 V

- Maximum Update Rate: 1 MS/s

- Communication Interface: Ethernet

4. NI 9234 DAQ:

Description The NI-9234 can measure signals from integrated electronic piezoelectric (IEPE) and non-IEPE sensors such as accelerometers, tachometers, and proximity probes. The NI-9234 is also compatible with smart TEDS sensors. The NI-9234 delivers a wide dynamic range and incorporates software-selectable AC/DC coupling and IEPE signal conditioning. The input channels simultaneously measure signals. Each channel also has built-in anti-aliasing filters that automatically adjust to your sample rate. When used with NI software, this module provides processing functionality for condition monitoring such as frequency analysis and order tracking.

Specifications:

- Manufacturer: National Instruments

- Type: Analog Input Module

- Channels: 4

- Resolution: 24 bits

- Input Range: ±10 V, ±5 V, ±2 V, ±1 V, ±500 mV, ±200 mV, ±100 mV

- Maximum Sample Rate: 51.2 kS/s per channel

- Communication Interface: Ethernet

5. KISTLER type 8774A50(Accelerometer):

Description The Type 8704B top connector accelerometers use a unique shear mode sensing element made of stable quartz crystals. The quartz sensing elements afford excellent long-term stability that ensure repeatable, accurate measurements for many years. Additionally, the shear element design provides low transverse sensitivity along with an insensitivity to base strain and thermal transients. All units are hermetically sealed and are constructed entirely of titanium or a combination of titanium and stainless steel. An internal circuit Piezotron impedance converter provides a high signal level at low impedance output.

Specifications:

- Manufacturer: Kistler Instruments

- Type: Piezoelectric Accelerometer

- Sensitivity: 10 mV/g

- Measurement Range: ±50 g

- Frequency Response: 1 Hz to 10 kHz

- Mounting: Screw mounting or adhesive mounting

- Operating Temperature Range: -54°C to 121°C

6. Sorenson XG60(Programmable power supply:

Description: The XG Series is the new standard for powerful, programmable DC power systems. Designed for test, production, laboratory, OEM and quality assurance applications, the XG provides a wealth of features to ensure accuracy and greater efficiency. It puts clean, reliable power at your disposal and delivers stable, variable output voltage and current for a broad range of development, test and system requirements.

Specifications:

- Manufacturer: Sorenson Power

- Type: Programmable DC Power Supply

- Output Voltage Range: 0-60 V

- Output Current Range: 0-60 A

- Maximum Output Power: 3600 W

- Voltage and Current Regulation: <0.05% + 20 mV/<0.1% + 30 mA

- Display Resolution: 10 mV, 10 mA

- Communication Interface: RS232, USB, Ethernet

- Software: Windows-based software for remote control and programming

7. Agilent Function Generator Model 33500B Series:

Description: The Agilent Function Generator Model 33500B Series is a high-performance function generator with built-in arbitrary waveform capabilities. It features a large color display, intuitive user interface, and a wide range of output waveforms and modulation capabilities. The generator is designed for use in applications such as research and development, electronic testing, and education.

Key Features:

- Output frequency range: 1 μHz to 30 MHz

- Output amplitude range: 1 mVpp to 10 Vpp into 50 ohms, 2 mVpp to 20 Vpp into open circuit

- Waveform types: Sine, square, ramp, pulse, noise, DC, arbitrary

- Arbitrary waveform memory: 16 Mpts

- Modulation types: AM, FM, PM, FSK, PWM, sweep, burst

- Interfaces: USB, LAN, GPIB

Specifications:

- Output frequency range: 1 μHz to 30 MHz

- Output amplitude range: 1 mVpp to 10 Vpp into 50 ohms, 2 mVpp to 20 Vpp into open circuit

- Output impedance: 50 ohms

- Waveform types: Sine, square, ramp, pulse, noise, DC, arbitrary

- Arbitrary waveform memory: 16 Mpts

- Modulation types: AM, FM, PM, FSK, PWM, sweep, burst

- Modulation input: External source or internal generator

- Harmonic distortion: < -50 dBc (0.1 Hz to 20 kHz)

- Total harmonic distortion: < 0.1

- Non-harmonic spurious: < -70 dBc (0.1 Hz to 1 MHz)

- Rise/fall time: < 8 ns

- Jitter: < 200 ps RMS (10 kHz to 20 MHz, 1 Vpp output)

- Interfaces: USB, LAN, GPIB